Master thesis and internship[BR]- Master's thesis : Investigation of various transonic stabilisation techniques for full potential flows calculation in DARTFlo[BR]- Integration Internship

Auteur : Brian, Guillaume
Promoteur(s) : Dimitriadis, Grigorios
Faculté : Faculté des Sciences appliquées
Diplôme : Master en ingénieur civil en aérospatiale, à finalité spécialisée en "aerospace engineering"
Année académique : 2021-2022
URI/URL : http://hdl.handle.net/2268.2/14510

LIÈGE université
School of Engineering

Investigation of various transonic stabilisation techniques for full potential flows calculation in DARTFlo

Master's thesis carried out to obtain the degree of Master of Science in Aerospace Engineering

Guillaume Brian s171284

University of Liège - School of Engineering and Computer Science

Academic supervisors
Pr. Grigorios Dimitriadis
Pr. Vincent E. Terrapon
Internship supervisor
Dr. Adrien Crovato

Academic year
2021 - 2022

Acknowledgments

First, I would like to thank my parents who gave me the opportunity to follow my life goals but also and above all encouraged me to give the best during these years. I wish to thank my family who always supported me when I needed it and prayed for me in difficult periods, my friends with whom I have spent and will continue to spend unforgettable moments, and last but not least my girlfriend who always pushed me to aim higher and to surpass myself.

Then, I thank the whole team of the research group led by Mr. Vincent E. Terrapon for their welcome, availability and precious help.

I particularly thank Adrien Crovato, who followed and helped me during these two semesters, for his time spent with me as well as for having passed me his knowledge of aerodynamics, programming and his sense of scientific research.

I would like to express my gratitude to the University of Liège and more specially to Prof. Bechet, Ms. Bissot and Ms. Tondeur, the Erasmus coordinators, for giving me the opportunity to live an abroad experience in Barcelona, at the Universitat Politècnica de Catalunya. This is by far one of the richest human experiences I have ever had and that I was lucky enough to share with my incredible roommates Thomas Bruyere and Arnaud Radermecker. I will never forget all the wonderful people I met there and the memorable moments shared.

Finally, I would like to thank all the people whose path I crossed during my studies who made me grow from near or far as an engineer but also as a person.

Guillaume Brian
Liège, June 9th 2022.

Abstract

The preliminary aircraft design is often performed based on low-fidelity aerodynamic models facilitating the evaluation of best-suited aircraft configurations thanks to low computational costs and reasonable accuracy at this early design stage. The *Full Potential* equation, based on the inviscid and isentropic assumptions, has demonstrated its ability to meet those requirements. However, the mathematical nature of this partial differential equation highlights that when the flow switches from subsonic to supersonic, it converts from elliptic to hyperbolic. This flow physics change needs to be reflected in the numerical implementation. DARTFLO, a full-potential solver, is implemented based on a physics-dependent solution experiencing mesh-dependency. Thenceforward, the present thesis aims at characterising the mesh-dependency of this physics-dependent solution and to propose alternatives to withdraw it.

The current physics-dependent implementation is studied through a mesh convergence analysis in three different test cases to characterise the mesh-dependency. The analysis relies on two comparison axes, the first is a study of global flow parameters and the second treats the problem from a local point of view. The three test cases are constructed to study the behaviour of each solution in different situations. The original DARTFLO implementation illustrates its mesh-dependency by local flow parameters which do not converge with respect to the mesh refinement as well as by instabilities appearing in the supersonic zones when the mesh is highly refined.

In parallel, three alternatives are derived and compared with the original implementation to assess their improvements in removing the mesh-dependency problem. The first alternative demonstrates improved mesh convergence and enables to partially remove the results mesh-dependency according to the case studied. However, the two others do not reveal to act on the mesh-dependency of the physics-dependent solutions.

Contents

1 Introduction

The aviation sector has been constantly growing for decades. The main reasons linked to the constant development of the air traffic are the general population and economic growth as well as the globalisation of world trade. Estimations have shown that the world population will reach 9.7 billions people by 2050 [1]. Moreover, according to S&P Global [2], the population's purchasing power is also bound to increase given that 2 people out of 3 will be associated to the middle class. This increase in purchasing power has a direct impact on the percentage of the population travelling by plane as much as the democratisation of air transport over the years. Finally, the globalisation of trade plays an undeniable role in the increase in cargo flights given the internationality of companies and their activities.

The International Air Transport Association (IATA) predicts the international air passenger traffic to almost double during the next 20 years [3]. In 2016, the total number of annual passengers reached 3.8 billions and is expected to enlarge to 7.2 billions in 2035, an increase of approximately 90% over 19 years. Additionally, Boeing predicts a 4% growth in air cargo per year from 2021 to 2040 [4].

Given these forecasts and within the climate debate, global and aviation authorities are voting policies to reduce the environmental impact of air traffic in future years. This impact is the result of various factors. The main one is the combustion of fuel in the aircraft's engines, which releases carbon dioxide CO_2 and nitrogen oxides NO_x into the atmosphere. Other factors also play an important role, such as the noise produced by the engines. According to David S. Lee *et al.* [5], in 2018, the share of CO_2 emissions due to aviation in total emissions is more or less 2.5%. Clean Aviation, with the aim of carbon neutrality within 2050 for the aviation sector, established different aircraft category targets in their "Strategic Research and Innovation Agenda" [6]. For example, for short-medium range commercial aircraft within 2035, they wish to reach a 50% fuel burn reduction, 86% emissions reduction compared to technologies available in 2020. In addition, the European Commission published its vision of the aviation within 2050 in an objective report named, "Flightpath 2050: Europe's vision for aviation" [7]. In this official report, the High-Level

Group on Aviation Research plans that the technologies and procedures available in 2050 would allow a 75% reduction in CO_2 emissions per passenger per kilometre to support the Air Transport Action Group (ATAG) target and a 90% reduction in NO_x emissions. In addition, the noise level should be reduced by 65%. These reductions are computed relative to the capabilities available in 2000. Another example to illustrate the involvement of aviation companies in the climate debate is the "ZEROe programme" developed by Airbus [8]. They have the ambition to develop the first zero-emission commercial aircraft by 2035. In summary, the involvement of the various aviation stakeholders in the environmental cause is growing.

Based on forecasts predicting the increased development of the aviation sector in the coming years, another essential aspect to be taken into account in the future of this sector is the aircraft fuel consumption. If the air transport sector wants to remain economically profitable, the aircraft fuel consumption has to be reduced as much as possible. Fuel is the most important aircraft operating cost for an airline [9, 10]. For example, Airbus predicted, in 2003 that fuel represented about 28% of total operating cost for a typical A320 family operator [11]. But in the near future, it could be more than 45% of all operating costs of an aircraft. Estimations have illustrated that every 500 grams of an aircraft's weight including crew, passengers, baggage and the aircraft itself, represents more or less 10.000$ in annual airline fuel costs. Moreover, given the daily evolution of the fuel price, the aviation industry is highly dependent on the fuel trade. This dependence has a direct impact on flight prices, since if the fuel price is high, the airline's operating costs increase accordingly. This increase also results in a slight reduction in the demand for air travel and air cargo. Therefore, the aircraft fuel consumption reduction is at the centre of concerns in the future aircraft design.

Reducing the environmental impact of aviation sector and aircraft fuel consumption can be achieved using various approaches such as improving the engine and fuel efficiency, the structural weight, the aircraft aerodynamic performance, air and ground traffic or using new types of fuel. Efficient modeling tools must be developed to enable the developments of these new technologies. This is especially the case for the preliminary design stage, where the primary objective is to identify best suited aircraft configurations to accomplish a given transport mission at an economic optimum while meeting prescribed requirements. Improving the aircraft preliminary design is of paramount importance in the era of transition in which aviation is currently in. A multitude of new technologies needs to be rapidly tested to confirm or deny their relevance and feasibility. With powerful, fast and as accurate as possible modelling tools, this evaluation is facilitated, faster and cheaper. In other words, developing better modelling tools for the preliminary aircraft design means improving the results accuracy while keeping the lowest computational time as possible which, in turns, allows to make better design choices. Thenceforth, more efficient final

aircraft designs can be achieved based on better physics modelling inducing better design choices in early design stages.

Aerodynamic modelling is one of the key concepts in aircraft design. Always in search of the best trade-off between results accuracy and computational cost in the aerodynamic models, different categories can be defined based on their level of fidelity, *i.e.* their level of approximation with respect to the physics that they represent. The highest level of fidelity is the solution of the *Navier-Stokes* equations, also called *Direct Numerical Simulations* (DNS) whereby, the equations are solved without any turbulence model. In other words, all the flow time and length scales are computed. This implies very fine meshes to capture all these scales and thus, extremely expensive computations. Instead of resolving the smallest flow length scales, which are the most computationally expensive, they can be cut off through a low-pass filter and computed by turbulence models. Therefore, coarser mesh grids can be used which drastically reduces the computational time. This is called *Large-Eddy Simulations* (LES), only the largest turbulent length scales are solved while the smallest are computed thanks to models. However, DNS and LES computations remain highly expensive. Consequently, they are not preferred during early stages of aircraft design even if they accurately capture flow physics and turbulence. Therefore, the highest level of fidelity used in the preliminary aircraft design is the *Reynolds-Averaged Navier-Stokes* (RANS) equations derived from the *Navier-Stokes* equations using the Reynolds decomposition and by time-averaging. In this aerodynamic model, all the turbulent length scales are modelled using turbulent models which highly lowers the computational time.

Several hypotheses can be made to simplify the *Reynolds-Averaged Navier-Stokes* equations and further reduce the computational time. The first assumption is to neglect the viscosity of the fluid and to resort to the *Euler* equations. This assumption is valid, except in the boundary layer, where viscous effects are dominant and drive the flow. In addition, viscous-inviscid interaction method can be implemented to counter-balance the inviscid assumption since this process is much less computationally expensive than taking into account fluid viscosity. Furthermore, if the flow is considered isentropic, it becomes irrotational and the *Euler* equations reduce to the *Full potential* equation.

Nowadays, most of the commercial airliners fly in a transonic regime which implies supersonic regions in the flow and possible shocks. However, the isentropicity hypothesis constraints the *Full potential* equation to be strictly valid for flows without embedded shocks. Nevertheless, it has been demonstrated that if the entropy change across the shock remains relatively small, flows with weak shocks can be modelled based on potential assumptions. This level of fidelity has been highlighted as providing reliable results for short computational time [12, 13, 14, 15, 16, 17, 18, 19, 20, 21, 22, 23, 24, 25, 26]. This is the reason why this level of fidelity is relevant for preliminary aircraft design.

Solving the *Full potential* equation in a transonic flow poses a major challenge. When the flow switches from subsonic to supersonic regime, the flow physics changes which is transcribed in the mathematical nature of this partial differential equation. Henceforth, it has to be solved differently in the implementation.

This research work focuses on DARTFLO, an unstructured finite element, full potential solver for steady transonic aerodynamic and aeroelastic modelling during preliminary aircraft design, mostly developed by Crovato [27] at the University of Liège. More specifically, on the physics-dependent implementation currently implemented in DARTFLO, which is based on density upwinding. However, this solution experiences mesh-dependency which alters mesh generation and mesh convergence analysis process.

The thesis is the continuation of the Crovato's work [27]. The main objective of this research work is to improve the stabilisation process by withdrawing mesh-dependency. To this end, two phases are set up. The first one is the characterisation of the density upwinding mesh-dependency through a mesh convergence analysis using the current DARTFLO implementation in different test cases. These tests cases will also be compared to a reference solution obtained by a state-of-the-art solver. The second one is to investigate, develop and implement corrections to the physics-dependent solution implemented in DARTFLO. Afterwards, the corrections are tested on the same test cases defined for the mesh-dependency characterisation phase in order to assess the improvements.

The master thesis is organised as follows. In Chapter 2, the developments and the hypotheses to derive the *Full potential* equation from the highest level of fidelity considered at the preliminary stage of an aircraft design are recalled. Afterwards, its mathematical nature is studied to bring into light one of the main challenges of solving transonic flows based on the *Full potential* equation. Then, a literature review about how this challenge has been addressed is detailed. To finish, the implementation of DARTFLO is outlined to illustrate how the code has been built.

Chapter 3 presents the new solutions to take into account the change in physics of the *Full potential* equation depending on the flow. They are mathematically detailed and justified. In addition, the finite element formulation is updated taking into account the changes.

From then on, the different implementations are compared in Chapter 4 in order to validate their improvements compared to the current DARTFLO implementation. First, the analysis methodology and the different test cases are explained. Afterwards, each new solution implementation is compared to the current DARTFLO implementation and the reference solution based on several parameters. As a conclusion, the results are discussed.

Chapter 5 summarises the work and draws conclusions from the results. In addition, it presents suggestion for future works.

2 Theoretical background

Throughout this chapter, the theoretical concepts relevant for an optimal research understanding are detailed. First, the *Full potential* equation is re-derived starting from the highest level of fidelity considered during the preliminary aircraft design stage. Then, the mathematical properties of this partial differential equation are studied to illustrate the main challenge in solving transonic flows based on this level of fidelity. Finally, a detailed review about how transonic flows are solved based on the *Full potential* equation is performed.

2.1 Aerodynamic levels of fidelity

The highest level of fidelity considered during the preliminary stage of an aircraft design is the unsteady *Reynolds-Averaged Navier-Stokes* (RANS) equations expressed as follows,

$$\frac{\partial \rho}{\partial t} + \nabla \cdot (\rho \mathbf{u}) = 0, \tag{2.1.1}$$

$$\frac{\partial \rho \mathbf{u}}{\partial t} + \nabla \cdot (\rho \mathbf{u} \otimes \mathbf{u} + p\mathbf{I}) - \nabla \cdot \boldsymbol{\tau} = 0, \tag{2.1.2}$$

$$\frac{\partial \rho e}{\partial t} + \nabla \cdot (\rho e \mathbf{u} + p\mathbf{u}) - \nabla \cdot (\boldsymbol{\tau} \cdot \mathbf{u} + \mu^{\star} c_p \nabla T) = 0, \tag{2.1.3}$$

where, ρ is the fluid density, $\mathbf{u}$ the velocity vector, e the specific energy, p the pressure, c_p the specific heat capacity at constant temperature and T the temperature. The stress tensor $\boldsymbol{\tau}$ is defined for a Newtonian fluid as given by the following relation.

$$\boldsymbol{\tau} = \mu \left(\nabla \mathbf{u} + \nabla \mathbf{u}^{\mathrm{T}} - \frac{2}{3} \mathbf{I} \nabla \cdot \mathbf{u} \right), \tag{2.1.4}$$

where, μ and μ^{*} are the total viscosity derived from a combination of the dynamic quantities denoted by the subscript d in Eq. 2.1.5, property of the fluid and turbulent quantities computed based on the Spalart-Allmaras's model [28] depicted by the subscript t,

$$\begin{aligned} \mu &= \mu_{\mathrm{d}} + \mu_{\mathrm{t}}, \\ \mu^{\star} &= \frac{\mu_{\mathrm{d}}}{\mathrm{Pr}_{\mathrm{d}}} + \frac{\mu_{\mathrm{t}}}{\mathrm{Pr}_{\mathrm{t}}}, \end{aligned} \tag{2.1.5}$$

with Pr is the Prandtl number defined as the ratio of momentum diffusivity to thermal diffusivity.

In the context of aeronautical flows during preliminary aircraft design, a first approximation that can be introduced into the aerodynamic model is the non-viscosity of the fluid expressed by,

$$\begin{cases} \boldsymbol{\tau} = \mathbf{0}, \\ \mu = \mu^* = 0. \end{cases} \tag{2.1.6}$$

Neglecting viscous effects is acceptable anywhere in a flow except in the boundary layer developing in the immediate vicinity of an immersed body. In this thin shear layer, they drive most of the flow physics. However, since it only represents a small fraction of the flow field, the inviscid assumption is relevant in early aircraft design stages.

Therefore, it enables to derive the *Euler* equations cast as follows,

$$\frac{\partial \rho}{\partial t} + \nabla \cdot (\rho \mathbf{u}) = 0, \tag{2.1.7}$$

$$\frac{\partial \rho \mathbf{u}}{\partial t} + \nabla \cdot (\rho \mathbf{u} \otimes \mathbf{u} + p\mathbf{I}), \tag{2.1.8}$$

$$\frac{\partial \rho e}{\partial t} + \nabla \cdot (\rho e \mathbf{u} + p\mathbf{u}) = 0. \tag{2.1.9}$$

In addition, if the flow is assumed to be steady and isentropic, the irrotationality condition ensues, which implies that the velocity $\mathbf{u}$ derives from a potential ϕ such that,

$$\mathbf{u} = \nabla \phi. \tag{2.1.10}$$

Introducing Eq. 2.1.10 in the *Euler* mass conservation equation (Eq. 2.1.7) taking into account all the assumptions established so far, the conservative form of the *Full potential* equation (FPE) can be derived,

$$\nabla \cdot (\rho \nabla \phi) = 0, \tag{2.1.11}$$

where, the density ρ can be obtained based on the isentropic flow relations resulting in the following expression,

$$\rho = \rho_\infty \left[1 + \frac{\gamma - 1}{2} M_\infty^2 \left(1 - |\nabla \phi|^2 \right) \right]^{\frac{1}{\gamma - 1}}, \tag{2.1.12}$$

where, ρ_∞ is the freestream density, γ the heat capacity ratio and M_∞ freestream Mach number.

The effect of these levels of fidelity have been compared by several authors [12, 13, 14, 15, 16, 17, 18, 19, 20, 21, 22, 23, 24, 25, 26]. The conclusion drawn from these analyses deduces that using the *Full potential* equation as the aerodynamic model for preliminary aircraft design is justified since reliable results can be obtained for small computational costs. As a result, the *Full potential* equation is studied in detail in the following section.

2.2 *Full potential* equation

The *Full potential* equation can be written in different forms, the conservative form has been obtained by assuming a steady inviscid, isentropic and thus, irrotational flow starting from the RANS equations as derived in SEC. 2.1.

$$\nabla \cdot (\rho \nabla \phi) = 0, \tag{2.2.1}$$

with, ρ is the fluid density and ϕ the potential.

By definition, the *Full potential* equation is strictly valid for flows without shocks due to the isentropicity condition. However, its use can be extended to model transonic flows containing weak shocks provided that the associated entropy production remains relatively small. The entropy produced by a shock wave depends on the normal Mach number, M_n in front of the shock such that the entropy change can be cast as,

$$\Delta S_{\mathrm{E}} = \mathcal{O}\left(M_n^2 - 1\right)^3. \tag{2.2.2}$$

Based on the work of Steger and Baldwin [29], the agreement between the inviscid solution and the experiments can be verified for a normal Mach number just before the shock $M_n \leq 1.3 - 1.35$. This constitutes an upper limit for the normal Mach number to ensure the validity of the results provided by the *Full potential* equation in transonic flows.

The non-conservative form of the *Full potential* equation can be derived by first entirely developing EQ. 2.2.1.

$$\nabla \cdot (\rho \nabla \phi) = \rho_x \phi_x + \rho \phi_{xx} + \rho_y \phi_y + \rho \phi_{yy} + \rho_z \phi_z + \rho \phi_{zz} = 0. \tag{2.2.3}$$

The expression of the density spatial derivatives can be obtained from the density isentropic relation EQ. 2.1.12, the speed of sound definition $a = \sqrt{\gamma RT}$ with R, ideal gas constant and T, the temperature as well as the isentropic density-pressure relation expressed as,

$$\frac{p}{\rho^\gamma} = \frac{\gamma + 1}{2\gamma}. \tag{2.2.4}$$

From then on, the *Full potential* equation can be transformed into its non-conservative form,

$$\left(a^2 - u^2\right)\phi_{xx} + \left(a^2 - v^2\right)\phi_{yy} + \left(a^2 - w^2\right)\phi_{zz} - 2uv\phi_{xy} - 2uw\phi_{xz} - 2vw\phi_{yz} = 0, \tag{2.2.5}$$

with, a is the speed of sound and (u, v, w) are the local velocity components.

A simplified version of the equation can further be derived assuming that lifting bodies induce small disturbances compared to the mean flow such that the total potential ϕ can be decomposed into a freestream potential ϕ_∞ and a disturbance potential $\varphi = \phi - \phi_\infty$.

It implies that the the flow is aligned with a particular coordinate direction, usually x-direction by formalism.

The steady *Transonic Small Disturbance* equation (TSD) is thus, derived by substituting these small-disturbance velocity components into the non-conservative form of the *Full potential* equation EQ. 2.2.5 and neglecting small terms with respect to the mean flow,

$$\left[1 - M_\infty^2 - M_\infty^2(\gamma+1)\frac{\varphi_x}{u_\infty}\right]\varphi_{xx} + \varphi_{yy} + \varphi_{zz} = 0, \tag{2.2.6}$$

where, φ is the small-disturbance potential and M_∞ the freestream Mach number, u_∞ freestream velocity and γ the heat capacity ratio.

This simplified version of the *Full potential* equation will only be used to illustrate the first major advances that have been made to solve transonic flows based on potential assumptions.

Two major challenges arise when solving transonic flows based on the potential assumptions. The first one is about the irrotionality assumption which induces that no aerodynamic loads can be produced. Therefore, an additional condition has to be enforced in order to meet the physical observations, named the Kutta condition. Since it is not the topic of this work, just the details of its implementation will be discussed.

On the other hand, the second challenge is the main concern of this research work. The difficulty in solving transonic flows based on the *Full potential* equation is the change in flow physics between sub- and supersonic regimes inducing a change in the equation's mathematical nature. Thus, a change in the numerical method to solve the problem is required. To illustrate this physical change, the mathematical properties of the *Full potential* equation can be developed.

The motivation behind studying the mathematical properties of a partial differential equation is first to acquire insight into the physics that it describes. Secondly, it helps to correctly develop the numerical solutions for the implementation in relation to the physics.

Starting from EQ. 2.2.5, assuming a two-dimensional case to be able to study the mathematical nature of this partial differential equation analytically, the non-conservative form of the *Full potential* equation EQ. 2.2.5 becomes,

$$\left(a^2 - u^2\right)\phi_{xx} - 2uv\phi_{xy} + \left(a^2 - v^2\right)\phi_{yy} = 0, \tag{2.2.7}$$

where, a is the speed of sound, (u, v) are the local velocity components and ϕ the potential. EQ. 2.2.7 is a second-order two-dimensional partial differential equation. Using EQ. 2.1.10, defining the velocity $\mathbf{u} = (u, v)$ deriving from a potential ϕ, it can be deduced that,

$$u = \frac{\partial\phi}{\partial x}, \tag{2.2.8}$$

$$v = \frac{\partial\phi}{\partial y}, \tag{2.2.9}$$

the non-conservative form of the *Full potential* can be reexpressed as a first-order partial differential equation,

$$\left(a^2 - u^2\right)\frac{\partial u}{\partial x} - 2uv\frac{\partial v}{\partial x} + \left(a^2 - v^2\right)\frac{\partial v}{\partial y} = 0. \tag{2.2.10}$$

If Eq. 2.2.8 and 2.2.9 are mixed, the following system of first-order partial differential equations can be built,

$$\left(a^2 - u^2\right)\frac{\partial u}{\partial x} - 2uv\frac{\partial v}{\partial x} + \left(a^2 - v^2\right)\frac{\partial v}{\partial y} = 0, \tag{2.2.11}$$

$$\frac{\partial v}{\partial x} - \frac{\partial u}{\partial y} = 0. \tag{2.2.12}$$

From this system, the characteristic equations can be obtained,

$$\underbrace{\left(\begin{bmatrix} a^2 - u^2 & -2uv \\ 0 & -1 \end{bmatrix} n_x + \begin{bmatrix} 0 & a^2 - v^2 \\ 1 & 0 \end{bmatrix} n_y\right)}_{A^k n_k} \begin{bmatrix} u \\ v \end{bmatrix} = 0, \tag{2.2.13}$$

where, n_x and n_y are the characteristics in respectively $x-$ and $y-$directions and A^k the matrix corresponding to the characteristic along the $k-$direction.

A non-trivial solution of the characteristic equations such that $\mathbf{U} = [u \quad v] \neq 0$ is,

$$\det|A^k n_k| = 0. \tag{2.2.14}$$

The mathematical properties of the *Full potential* equation directly depend on the nature of the characteristics. If $\lambda = \frac{n_x}{n_y}$ is posed, the characteristics can be determined by solving the following equation with respect to λ,

$$(a^2 - u^2)\lambda^2 - 2uv\lambda + (a^2 - v^2) = 0. \tag{2.2.15}$$

Henceforth, the two characteristics are given by,

$$\lambda_{1,2} = \frac{2uv \pm \sqrt{4u^2v^2 - 4(a^2 - u^2)(a^2 - v^2)}}{2(a^2 - u^2)}. \tag{2.2.16}$$

From Eq. 2.2.16, the nature of the characteristics can be deduced from the sign of the square root. Knowing that the Mach number is defined by $M = \frac{V}{a}$ with $|\mathbf{u}|$ is the local velocity magnitude and a the speed of sound.

- if M < 1, all n characteristics are complex which implies that the *Full potential* equation is hyperbolic,
- if M $= 1$, less than n real characteristics which implies that the *Full potential* equation is parabolic,
- if M > 1, all n characteristics are real which implies that the *Full potential* equation is elliptic,

Therefore, the equation switches from elliptic to hyperbolic when the flow becomes supersonic which transcribes a change in the flow physics. An elliptic partial differential equation represents an information transport mainly driven by diffusion phenomena such that the information propagates in every direction. Whereas, a hyperbolic partial differential equation describes an information propagation dominated by convection phenomena and thus, transmitted along one specific direction.

This change in the mathematical nature of the *Full potential* equation is one of the main challenges for transonic predictions. It has to be reflected in the numerical implementation to obtain a physics-dependent differentiation and thus, has to use suitable and stable discretization schemes for the different types of the equation.

In the next section, the different physics-dependent solutions which have been developed since the beginning of the *Full potential* age are reviewed in order to have a clear overview on what has been done and how they work.

2.3 Physics-dependent solutions

This section outlines the main advances over the years regarding, how physics change is handled numerically and thus, nonlinear potential methods based on the literature review of Holst [20] and Crovato [27].

First breakthroughs to solve transonic flows with *Full potential* equation have been performed using the steady *Transonic Small Disturbance* equation by Murman and Cole in 1971 [30]. The Murman and Cole algorithm switches from central differencing to upwind differencing when the equation goes from elliptic to hyperbolic. As explained in Sec. 2.2, since an elliptic equation is dominated by diffusion, a central-differencing scheme is suitable to take into account information from all directions around the current element. On the contrary, a hyperbolic equation describes convection phenomena such that an upwind differencing scheme is suitable since the information travels along one specific direction. Therefore, they implemented a discretization scheme which represents the change in flow behaviour between subsonic and supersonic regions of the flow.

In two dimensions[1], the steady *Transonic Small Disturbance* equation into its conservative form can be written as follows,

$$\nabla \cdot \mathbf{F} = \nabla \cdot \begin{bmatrix} f \\ g \end{bmatrix} = \nabla \cdot \begin{bmatrix} (1 - M_\infty^2)\,\varphi_x - \frac{\gamma-1}{2} M_\infty^2 \varphi_x^2 \\ \varphi_y \end{bmatrix}, \tag{2.3.1}$$

where, f and g are the fluxes depending on M_∞ the freestream Mach number, ψ the disturbance potential and γ the heat capacity ratio.

[1] All the mathematical details are specified in two dimensions for conciseness.

Based on the Murman and Cole algorithm formulation [30], the equation can be discretized using a central difference scheme and modifying the fluxes in the flow direction defined by the small-disturbance assumption to enable the switch to upwind differencing when the flow becomes supersonic.

$$\frac{\bar{f}_{i+1/2,j} - \bar{f}_{i-1/2,j}}{\Delta x} + \frac{g_{i,j+1/2} - g_{i,j-1/2}}{\Delta y} = 0, \tag{2.3.2}$$

with, i and j subscripts designate the location of the point in the mesh grid and Δx and Δy are the spatial steps in x- and y-directions, such that the element coordinates in the flow domain are defined as, $x = i\Delta x$ and $y = j\Delta y$. The modified flux $\bar{f}$ is defined by,

$$\bar{f}_{i+1/2,j} = \mu_i f_{i+1/2,j} + (1 - \mu_i)\, f_{i-1/2,j}, \tag{2.3.3}$$

where, μ_i is the switching function enabling to move from central to upwind differencing with respect to the following expression,

$$\mu_i = \begin{cases} 1, & M_{i,j} \leqslant 1 \\ 0, & M_{i,j} > 1 \end{cases}, \tag{2.3.4}$$

with, $M_{i,j}$ is defined as the local Mach number computed at the point (i, j) of the mesh grid. This scheme is automatically second-order accurate and centrally-differenced in the subsonic regions and first-order accurate and upwind-differenced in the supersonic regions of the flow.

After having worked on the steady *Transonic Small Disturbance* equation, the researchers started to look into the *Full potential* equation and the first two-dimensional codes appeared in the early seventies thanks to the work of Steger and Lomax [31] and also Garabedian and Korn [32]. In their formulation, the equation is discretized using finite differences on grids mapped from a circle to airfoils. This provides an elegant grid generation option and allows for simplified application of boundary conditions. An extension has been developed by Bauer *et al.* [33] to enable an incorporation of a boundary layer correction. Thereafter, some generalisations to solve more complex geometries have been performed by several authors such as axisymmetric blunt bodies [34, 35], inlets [36, 37, 38, 39], and turbomachinery airfoil cascades [40, 41].

In 1974, the first three-dimensional full potential solver was implemented by Jameson and Caughey [42, 43]. This code still uses conformal mapping to build the grid on which the finite differences are applied. However, Jameson and Caughey enhanced the Murman and Cole algorithm [30] with the key concept of rotated differencing. Instead of switching from a central scheme to an upwind one, a stable discretization scheme for the elliptic form of the *Full potential* equation is developed and then, artificial viscosity is added when it becomes hyperbolic to stabilise the scheme.

The concept of the rotated difference scheme consists in splitting the fluxes $\mathbf{F}$ into physical fluxes f and g and artificial viscosity terms P and Q. Therefore, the fluxes of the *Full potential* equation can be rewritten under the form,

$$\nabla \cdot \mathbf{F} = \nabla \cdot \begin{bmatrix} f + P \\ g + Q \end{bmatrix}. \tag{2.3.5}$$

From then on, the *Full potential* equation can be discretized given by the following relation,

$$\overleftarrow{\delta}_{\xi} \left(f_{i+1/2,j} + P_{i+1/2,j} \right) + \overleftarrow{\delta}_{\eta} \left(g_{i,j+1/2} + Q_{i,j+1/2} \right) + A_{i,j} = 0, \tag{2.3.6}$$

where, $\overleftarrow{\delta}$ represents an upwind derivative and (ξ, η) are the coordinates of the computational space computed through conformal mapping from the physical coordinates (x, y).

The physical fluxes are derived from an average of the momentum at the faces of the cell such that,

$$\begin{aligned} f_{i+1/2,j} &= \frac{1}{2} \left[\frac{\rho u}{J}\Big|_{i+1/2,j+1/2} + \frac{\rho u}{J}\Big|_{i+1/2,j-1/2} \right], \\ g_{i,j+1/2} &= \frac{1}{2} \left[\frac{\rho v}{J}\Big|_{i+1/2,j+1/2} + \frac{\rho v}{J}\Big|_{i-1/2,j-1/2} \right], \end{aligned} \tag{2.3.7}$$

where, u and v are the velocity components and J is the Jacobian matrix of the conformal mapping from the physical space (x, y) to the computational space (ξ, η). In addition, the fluxes acting as artificial viscosity can be derived in the computational space from these relations,

$$\begin{aligned} P_{i+1/2,j} &= \begin{cases} \frac{\mu\rho}{Ja^2} \left(u^2 \delta_{\xi\xi} + uv \delta_{\xi} \delta_{\eta} \right) \phi_{i,j}, & u_{i+1/2,j} > 0, \\ -\frac{\mu\rho}{Ja^2} \left(u^2 \delta_{\xi\xi} + uv \delta_{\xi} \delta_{\eta} \right) \phi_{i,j}, & u_{i+1/2,j} < 0, \end{cases} \\ Q_{i,j+1/2} &= \begin{cases} \frac{\mu\rho}{Ja^2} \left(uv \delta_{\xi} \delta_{\eta} + v^2 \delta_{\eta\eta} \right) \phi_{i,j}, & v_{i,j+1/2} > 0, \\ -\frac{\mu\rho}{Ja^2} \left(uv \delta_{\xi} \delta_{\eta} + v^2 \delta_{\eta\eta} \right) \phi_{i,j}, & v_{i,j+1/2} < 0, \end{cases} \end{aligned} \tag{2.3.8}$$

where a is the speed of sound and μ the switching function which enables to activate the artificial viscosity terms depending on the region of the flow. The switching function is defined as follows and depends on a user-specified cut-off Mach number M_C,

$$\mu = \max \left(0, 1 - \frac{M_C^2}{M^2} \right), \tag{2.3.9}$$

with, M is the local Mach number.

To finish, the term $A_{i,j}$ is a recoupling term to restore the continuity between the odd and even points.

Based on the successful concept of rotated difference, several authors [44, 45, 46] have developed another type of spatial discretization scheme for the conservative form of the *Full potential* equation, the artificial density method.

The concept has similarities with rotated difference [42, 43] developed by Jameson i.e. add artificial viscosity when the flow becomes supersonic (hyperbolic PDE) to stabilise the

second-order accurate centrally-differenced scheme stable and suitable for subsonic flows (elliptic PDE). However, the artificial viscosity term is not added directly to the equation, but through an upwind bias applied to the density in the discretized equation. It provides an upwind influence in supersonic regions without the explicit addition of an artificial viscosity term in the *Full potential* equation. Instead, the stabilising effect is accomplished through the modified density computed by biasing the physical density with an upwind one which is mathematically equivalent to rotated differences. The interest of this approach is that it simplifies the introduction of an upwind influence into the numerical equation (cfr. solving techniques [27]) when the flow is supersonic. The upwind bias applied to the physical density is computed in different ways according to the authors.

In 1978, Eberle [44] proposes the first density upwinding formulation.

$$\tilde{\rho} \approx \rho + \varepsilon \max\left(0, 1 - \frac{1}{M^2}\right)(\rho_H - \rho), \tag{2.3.10}$$

where, ε is a constant in the entire flow field and ρ_H density computed at a point which lies on a small distance upstream from the current element. Thus, on the one hand, the accuracy of the method can be increased with small ε, and on the other hand iterative convergence from case to case can be guaranteed with large ε.

One year later, another formulation is developed by Holst and Ballhaus [45] inspired from the switching algorithm implemented by Murman and Cole [30]. In one dimension, the upwinded density can be evaluated based on the following expression,

$$\tilde{\rho}_{i+\frac{1}{2}} = (1 - \nu_i)\,\rho_{i+\frac{1}{2}} + \nu_i \rho_{i-\frac{1}{2}}, \tag{2.3.11}$$

where $\nu_i = \max(0, 1 - a^2/u^2)$. Holst and Ballhaus observed that this switching function formulation produces pre-shock overshoots that often resulted in numerical instabilities. Therefore, an alternative definition for ν was introduced,

$$\nu = \begin{bmatrix} 1 - (\rho/\rho^*)^{\sigma_e} & M \geq 1 \\ 0 & M < 1 \end{bmatrix}, \tag{2.3.12}$$

with ρ^* is the density computed at sonic conditions, σ_e is a constant determined by numerical experiment at six and M the local Mach number.

In the same year, Hafez and Murman [46] present another alternative to express the upwinded density by subtracting from the physical density, an upwind bias computed with the density gradient between an upwind and the current element.

$$\tilde{\rho} = \rho - \mu \Delta s \overleftarrow{\delta}_s \rho \approx \rho - \mu(\rho - \rho_U), \tag{2.3.13}$$

where, $\mu = \mu_C \max\left(0, 1 - \frac{M_C^2}{M^2}\right)$ dependent on M_C a cut-off Mach number used to define the extent of the region where the bias is applied and μ_C an amplification of the density

bias. Moreover, Δs is the upwind streamwise cell size, $\overleftarrow{\delta_s}\rho$ streamline upwind derivative of the density and ρ_U is the density computed at an upwind element defined through several processes.

Furthermore, an improvement has been developed for the artificial density approach which consists of upwinding the entire mass fluxes [47, 48, 49, 50, 51, 52, 53]. It enables good shock capturing characteristics and to smooth flow gradients through sonic lines. Although for weak shocks, the flux upwinding provides slightly better results, the gain in accuracy is not worth the increase in computational cost.

2.4 DARTFlo

This research work focuses on DARTFlo (Discrete Adjoint for Rapid Transonic Flows), an open-source C++/Python, unstructured finite element, full potential solver, developed at the University of Liège by Dr. Adrien Crovato [27] under the supervision of Pr. Vincent E. Terrapon and Pr. Grigorios Dimitriadis. DARTFlo aims to perform transonic aerodynamic and aeroelastic computations during the preliminary stage of the aircraft design process partially thanks to the development of an aerodynamic modeling tool performing such computations with low costs. This code is currently able to rapidly solve steady transonic flows on arbitrary configurations, ranging from 2D airfoils to 3D full aircraft (without engine). A low-fidelity aerodynamic model has been preferred. The *Full potential* equation has been validated as being a relevant choice for this early design stage. As detailed in Sec. 2.2, the *Full potential* equation switches from elliptic to hyperbolic when the flow moves from a subsonic to a supersonic regime. However, the subsonic regions still represent a large portion of the flow in transonic flows. Henceforth, the finite element method has been chosen in DARTFlo since it is well adapted for solving elliptic partial differential equations and only needs to be adapted for hyperbolic partial differential equations.

2.4.1 Finite element formulation

The finite element formulation of a partial differential equation can be derived based on its weak form and the associated boundary conditions using a discretisation procedure.

Considering a domain Ω bordered by a surface Γ illustrated in Fig. 2.1 and assuming that the potential ϕ is contained in the Sobolev space, the *Full potential* equation is multiplied by test functions ψ and integrated over the domain Ω to build its weak formulation cast as,

$$\int_\Omega \rho\nabla\phi\cdot\nabla\psi dV - \int_\Gamma \overline{\rho\nabla\phi}\cdot\mathbf{n}\psi dS = 0, \quad \forall\psi\in H^1(\Omega), \tag{2.4.1}$$

where ρ is the density evaluated based on Eq. 2.1.12, ϕ the potential, ψ the test functions, $\mathbf{n}$ is the unit normal vector to the surface Γ and $H^1(\Omega)$ the Sobolev space.

Boundary surfaces of the domain Γ can be split into an upstream boundary Γ_u, farfield boundary Γ_f and the body boundary Γ_b as depicted in FIG. 2.1. To solve the problem, boundary conditions have to be imposed on these surfaces. Firstly, an impermeability condition is imposed on the body surface Γ_b through a Neumann condition such that, the normal velocity components to the body surface are null,

$$\overline{\nabla\phi} \cdot \mathbf{n}\big|_{\Gamma_\mathrm{b}} = 0. \tag{2.4.2}$$

Secondly, boundary conditions are also imposed to control the flow in the domain. The freestream flow is imposed at the upstream surface to dictate the inlet flow through a Dirichlet condition,

$$\bar{\phi}\big|_{\Gamma_\mathrm{u}} = \phi_\infty, \tag{2.4.3}$$

where, ϕ_∞ is the freestream potential at the coordinates (x, y, z) defined as follows,

$$\phi_\infty = x\cos\alpha\cos\beta + y\sin\beta + z\sin\alpha\cos\beta, \tag{2.4.4}$$

with, α is the angle of attack and β the sideslip angle (only in three-dimensions).

In addition, a condition has to be set to model the undisturbed flow at the farfield surfaces. A Neumann boundary condition is adopted,

$$\overline{\nabla\phi} \cdot \boldsymbol{n}\big|_{\Gamma_\mathrm{f}} = \mathbf{U}_\infty \cdot \boldsymbol{n}, \tag{2.4.5}$$

where $\mathbf{U}_\infty$ is the freestream velocity.

The last condition to be enforced concerns the potential assumptions. As explained in SEC. 2.2, since the flow has been assumed to be irrotational, no aerodynamic loads can be produced by the immersed body, which is not physical. From experiments which illustrated that real fluids are viscous and can not turn around sharp corners such as the trailing edge, Kuethe and Schetzer [54] stated that a body with a sharp trailing edge which is moving through a fluid will create about itself a circulation of sufficient strength to hold the rear stagnation point at the trailing edge. Many formulations of the Kutta condition exist. The DARTFLO Kutta condition considers a flat wake sheet denoted Γ_w starting from the trailing edge of the body to the downstream farfield surface as illustrated in FIG. 2.1. This wake sheet is duplicated to enforce the equality of the mass fluxes on the upper and lower sides of the wake such that,

$$\int_{\Gamma_{\mathrm{w,u}}} \rho\nabla\phi \cdot \mathbf{n} dS = -\int_{\Gamma_{\mathrm{w},l}} \rho\nabla\phi \cdot \mathbf{n} dS, \tag{2.4.6}$$

where, u and l subscripts denote the upper or lower side of the wake sheet. This condition can be particularised at the trailing edge such that, EQ. 2.4.6 becomes,

$$\int_{\Gamma_{\mathrm{TE,u}}} |\nabla\phi|^2 \psi dS - \int_{\Gamma_{\mathrm{TE},1}} |\nabla\phi|^2 \psi dS = 0, \quad \forall\psi \in H^1\left(\Gamma_{\mathrm{TE,u}}\right), \tag{2.4.7}$$

with, Γ_{TE} denotes the trailing edge surface.

To finish, a third condition to avoid the wake sheet to behave as a wall is to prevent any pressure jump across the wake. For potential flow, it is equivalent as imposing the continuity of the velocity magnitude such that,

$$\int_{\Gamma} (\psi + \Psi) \left[\left[|\nabla \phi|^2 \right] \right] dS = 0. \tag{2.4.8}$$

where, the brackets denote a jump of the quantity across the wake sheet. The test function is stabilised using a Petrov Galerkin formulation such that,

$$\Psi = \frac{1}{2} \frac{h}{u_\infty} \left(\mathbf{u}_\infty \cdot \nabla \phi \right), \tag{2.4.9}$$

with u_∞ is the freestream velocity and h a characteristic length.

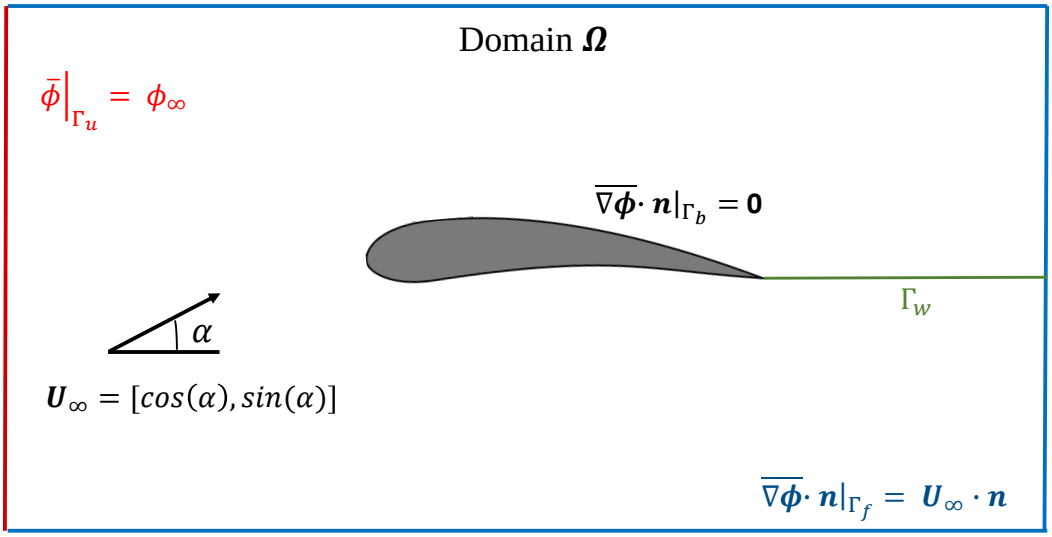

FIGURE 2.1: Domain definition for finite element computations and illustration of the boundary conditions from [27].

2.4.2 Supersonic regions treatment

As explained in SEC. 2.2, the supersonic regions of the flow have to be stabilised. The formulation proposed by Hafez and Murman [46] has been chosen such that the physical density is replaced by a biased (*i.e.* upwinded) density,

$$\tilde{\rho} = \rho - \mu(\rho - \rho_U), \tag{2.4.10}$$

where, $\tilde{\rho}$ is the upwinded density, ρ the physical density computed with EQ. 2.1.12, $\mu = \mu_C \max\left(0, 1 - \frac{M_C^2}{M^2}\right)$ dependent on M_C a cut-off Mach number used to define the extend

of the region where the bias is applied and μ_C an amplification of the density bias and ρ_U the density computed at an upwind element.

In DARTFLO, the upwind element is exactly determined based on the local velocity vector. As illustrated in FIG. 2.2, the upwind element with respect to the current one is chosen along the adjacent elements by minimising the scalar product between the local velocity vector denoted in blue and the vector joining both centroïds.

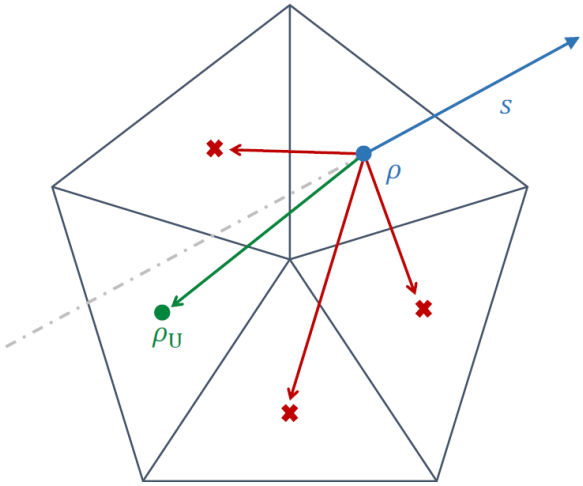

FIGURE 2.2: Identification process of the upwind element in DARTFLO for the density upwinding procedure [27].

The density upwinding in DARTFLO has demonstrated an increased sensitivity to mesh density which leads to highly variable results depending on the mesh sizes and distributions. Mesh convergence analyses have been performed on different test cases by Crovato [27]. For a weak shock test case, despite the refinement of the mesh, local flow parameters keep varying despite a shock position convergence. For a strong shock test case, DARTFLO is capable to capture a shock but the difference between its solution and state-of-the-art solvers increases, compared to the weak shock case. In addition, further refining leads to oscillatory behaviours of the local variables in the supersonic regions.

2.4.3 Finite element discretisation

The discretisation process is performed using the continuous Galerkin method [55]. The goal is to particularise the *Full potential* finite element formulation for each element and then, create a global system of equations. The potential ϕ and test functions ψ are expressed as,

$$\begin{aligned} \phi &= N_i \phi_i, \\ \psi &= N_i \psi_i, \end{aligned} \tag{2.4.11}$$

where, N_i are the shape functions unique for each element and used to interpolate the nodal values. They are defined as being equal to one at the node i and zero at others such

that, they are to meet the following requirement,

$$\sum_i N_i = 1, \tag{2.4.12}$$

over their support.

From then on, the weak formulation of the *Full potential* equation (Eq. 2.4.1) can be discretised,

$$\sum_e \int_{\Omega_e} \tilde{\rho}_e \nabla N_j \phi_j \cdot \nabla N_i \psi_i dV_e - \sum_e \int_{\Gamma e} \overline{\rho \nabla \phi_e} \cdot \mathbf{n}_e N_i \psi_i dS_e = 0, \quad \forall \psi_i, \tag{2.4.13}$$

where, the subscript e denotes elemental quantities and $\tilde{\rho}$ the upwinded density computed based on Eq. 2.4.10.

The boundary conditions are also discretised which are particularised for each element. The Neumann boundary conditions described in Eq. 2.4.2 and 2.4.5 becomes,

$$\begin{aligned} \overline{\nabla \phi_e} \cdot \mathbf{n_e}\big|_{\Gamma_{\mathrm{b_e}}} &= 0, \\ \overline{\nabla \phi_e} \cdot \mathbf{n_e}\big|_{\Gamma_{\mathrm{f_e}}} &= \mathbf{U}_\infty \cdot \mathbf{n_e}. \end{aligned} \tag{2.4.14}$$

In addition, the Dirichlet condition (Eq. 2.4.3) is expressed as follows,

$$\bar{\phi_e}\big|_{\Gamma_{\mathrm{u_e}}} = \phi_\infty, \tag{2.4.15}$$

The Kutta condition is also discretised. First, the continuity in the mass flux through the wake can be reexpressed as,

$$\sum_{\mathrm{e}} \int_{\Omega_{\mathrm{w,e_e}}} \tilde{\rho}_{\mathrm{e}} \nabla N_j \phi_j \cdot \nabla N_i \psi_{i_{\mathrm{w,l}}} dV_{\mathrm{e}} + \sum_{\mathrm{e}} \int_{\Omega_{\mathrm{w,u_e}}} \tilde{\rho}_{\mathrm{e}} \nabla N_j \phi_j \cdot \nabla N_i \psi_{i_{\mathrm{w,l}}} dV_{\mathrm{e}} = 0, \quad \forall \psi_i \in \Omega_{\mathrm{w,l}}. \tag{2.4.16}$$

The latter equation can be particularised for the trailing edge, uniquely in three-dimensional cases.

$$\sum_{\mathrm{e}} \int_{\Gamma_{\mathrm{TE,u_e}}} \nabla \phi \cdot \nabla N_j \phi_j \psi_{i_{\mathrm{TE,u}}} dS_{\mathrm{e}} - \sum_{\mathrm{e}} \int_{\Gamma_{\mathrm{TE,l_e}}} \nabla \phi \cdot \nabla N_j \phi_j \psi_{i_{\mathrm{TE,u}}} dS_{\mathrm{e}} = 0, \quad \forall \psi_i \in \Gamma_{\mathrm{TE,u}}. \tag{2.4.17}$$

Likewise, the no pressure jump condition across the shock is discretised,

$$\sum_{\mathrm{e}} \int_{\Gamma_{\mathrm{w_e}}} (\psi + \Psi)_{\mathrm{w,u}} \left([\nabla \phi \cdot \nabla N_j \phi_j]_{\mathrm{w,u}} - [\nabla \phi \cdot \nabla N_j \phi_j]_{\mathrm{w,l}} \right) dS_{\mathrm{e}} = 0, \quad \forall (\psi + \Psi)_{\mathrm{w,u}}, \tag{2.4.18}$$

where, the stabilised test functions are computed based on the following expression,

$$(\psi + \Psi)_{\mathrm{w,u}} = N_i \psi_i + \frac{1}{2} \frac{h}{U_\infty} \left(\mathbf{U}_\infty \cdot \nabla N_i \psi_i \right), \quad \psi \in \Gamma_{\mathrm{w,u}}. \tag{2.4.19}$$

2.4.4 Numerical scheme

The discretised *Full potential* equation has to be written as a set of equations using a residual vector $\mathbf{R}$ since any test function $\boldsymbol{\psi}$ has to verify the equation such as,

$$\mathbf{R} = 0. \tag{2.4.20}$$

However, since the *Full potential* equation is non-linear, the system of equations can only be solved iteratively. Thus, a Taylor expansion is developed around a known solution $\boldsymbol{\phi}_s$ giving,

$$\mathbf{R} + \frac{\partial \mathbf{R}}{\partial \boldsymbol{\phi}}(\boldsymbol{\phi} - \boldsymbol{\phi}_s) + \mathcal{O}\left((\boldsymbol{\phi} - \boldsymbol{\phi}_s)^2\right) = 0. \tag{2.4.21}$$

Therefore, the iterative process can be built neglecting the second-order term and taking as known solution the potential $\boldsymbol{\phi}_n$ at iteration n resulting in the following numerical form of the *Full Potential* equation,

$$\mathbf{J}_n \left(\phi_{n+1} - \phi_n\right) = -\mathbf{R}_n, \tag{2.4.22}$$

where, ϕ_{n+1} is a better approximation of the solution than ϕ_n, $\mathbf{R}_n$ the residual vector at iteration n and $\mathbf{J}_n$ the Jacobian matrix at iteration n defined as the variation of the residual vector with respect to the solution $\boldsymbol{\phi}$ computed around the known solution at $\boldsymbol{\phi}_n$,

$$\mathbf{J}_n = \left.\frac{\partial \mathbf{R}}{\partial \phi}\right|_{\phi_n}. \tag{2.4.23}$$

Two iterative methods are implemented in DARTFLO to solve EQ. 2.4.22, the Picard iteration with relaxation, and a quasi-Newton algorithm combined with line search. Picard iteration scheme has demonstrated poor convergence characteristics and sometimes does not even converge in presence of shocks. Consequently, this method is constrained to solve compressible flows without supersonic regions. Henceforth, only the quasi-Newton scheme has been used in the scope of this thesis to solve the EQ. 2.4.22 and derive the solution at next iteration $\boldsymbol{\phi}_{n+1}$.

Based on the weak form of the *Full potential* equation EQ. 2.4.1 and the discretisation process described in EQ. 2.4.11, the residual vector can be discretised as follows,

$$R_i = \int_{\Omega_\mathrm{e}} \left[(1-\mu)\rho_\mathrm{e} + \mu\rho_\mathrm{U}\right] \partial_k\phi\partial_k N_i dV_\mathrm{e} - \int_{\Gamma_\mathrm{e}} \overline{\rho\partial_k\phi n_k} N_i dS_\mathrm{e}. \tag{2.4.24}$$

In the quasi-Newton algorithm combined with line search, the Jacobian can be computed either numerically or analytically. However, to obtain the lowest computational time, the Jacobian matrix is determined analytically by deriving the residual vector $\mathbf{R}$ with respect to the potential ϕ.

$$
\begin{aligned}
J = \frac{\partial R}{\partial \phi} = = & \int_\Omega \frac{\partial}{\partial \phi}\{\tilde{\rho}\}\nabla\phi\cdot\nabla\psi dV + \int_\Omega \tilde{\rho}\frac{\partial}{\partial\phi}\{\nabla\phi\cdot\nabla\psi\}dV, \\
& = \int_\Omega (1-\mu)\frac{\partial}{\partial\phi}\{\rho\nabla\phi\cdot\nabla\psi\}dV \\
& + \int_\Omega \mu\left(\frac{\partial}{\partial\phi}\left\{\rho_{\mathrm{U}}\right\}\nabla\phi\cdot\nabla\psi + \rho_{\mathrm{U}}\frac{\partial}{\partial\phi}\{\nabla\phi\cdot\nabla\psi\}\right)dV \\
& + \int_\Omega -\left(\rho-\rho_{\mathrm{U}}\right)\frac{\partial}{\partial\phi}\{\mu\}\nabla\phi\cdot\nabla\psi dV,
\end{aligned}
\tag{2.4.25}
$$

where the derivatives of the parameters with respect to potential result from the parameter definition expressions,

$$
\begin{aligned}
\frac{\partial}{\partial\phi}\{\rho\} &= -M_\infty^2\rho^{2-\gamma}\nabla\phi\cdot\frac{\partial}{\partial\phi}\{\nabla\phi\}, \\
\frac{\partial}{\partial\phi}\{\mu\} &= \mu_{\mathrm{C}}M_{\mathrm{C}}^2\left(\frac{2}{M^3}\frac{\partial}{\partial\phi}\{M\}\right), \\
\frac{\partial}{\partial\phi}\{M\} &= M\left[\frac{1}{|\nabla\phi|^2}+\frac{\gamma-1}{2}\frac{1}{a^2}\right]\nabla\phi\cdot\frac{\partial}{\partial\phi}\{\nabla\phi\}.
\end{aligned}
\tag{2.4.26}
$$

Note that the derivative of the switching function is particularised for the supersonic regions since it is null otherwise. In addition, the speed of sound is computed based on,

$$
a = \sqrt{\frac{1}{M_\infty^2}+\frac{\gamma-1}{2}\left(1-|\nabla\phi|^2\right)}. \tag{2.4.27}
$$

Based on the finite element discretisation, the Jacobian expression can be discretised,

$$
\begin{aligned}
J_{ij} = & \int_{\Omega_{\mathrm{e}}}(1-\mu)\left[\frac{\partial\rho}{\partial\phi}\partial_k\phi\partial_k N_i + \rho_{\mathrm{e}}\partial_k N_j\partial_k N_i\right]dV_{\mathrm{e}} \\
& + \int_{\Omega_{\mathrm{e}}}\mu\left[\frac{\partial\rho_U}{\partial\phi}\partial_k\phi\partial_k N_i + \rho_{\mathrm{U}}\partial_k N_j\partial_k N_i\right]dV_{\mathrm{e}} \\
& - \int_{\Omega_{\mathrm{e}}}\left(\rho_{\mathrm{e}}-\rho_{\mathrm{U}}\right)\left[\frac{\partial\mu}{\partial\phi}\partial_k\phi\partial_k N_i\right]dV_{\mathrm{e}},
\end{aligned}
\tag{2.4.28}
$$

where, the different derivatives become,

$$
\begin{aligned}
\frac{\partial}{\partial\phi}\{\rho\} &= -M_\infty^2\rho_{\mathrm{e}}^{2-\gamma}\partial_k\phi\partial_k N_j, \\
\frac{\partial}{\partial\phi}\{\rho_U\} &= -M_\infty^2\rho_{\mathrm{U}}^{2-\gamma}\partial_k\phi_U\partial_k N_{jU}, \\
\frac{\partial}{\partial\phi}\{\mu\} &= \frac{2\mu_{\mathrm{C}}M_{\mathrm{C}}^2}{M_{\mathrm{e}}^3}\left(\frac{1}{\sqrt{\partial_k\phi^2 a_{\mathrm{e}}^2}}+\frac{\gamma-1}{2}\frac{\sqrt{\partial_k\phi^2}}{\sqrt[3]{a_{\mathrm{e}}^2}}\right)\partial_k\phi\partial_k N_j,
\end{aligned}
\tag{2.4.29}
$$

with, the subscript U denotes the upwind element.

3 Stabilisation solutions

In this chapter, different options to solve the mesh density sensitivity problem of the stabilisation process implemented in DARTFLO are presented. Firstly, the general concept of each method is specified and then, the mathematical details are carried out to justify their relevance compared to previous stabilisation processes reviewed in SEC. 2.3. Lastly, the different numerical equations are updated, based on the corrections.

Note that with the aim of gaining insight about the original DARTFLO density upwinding, a one-dimensional finite-element, full potential code has been implemented. The objective of this test code is to correctly understand the functioning of the stabilisation process in a simple case and thus, propose corrections for the mesh-dependency. However, within the thesis duration, the code could not be fully operational. Therefore, an annex is devoted to the details of the implementation (cfr. SEC. A).

3.1 Fixed length correction

As explained in SEC. 2.4 and demonstrated in Crovato's thesis [27], DARTFLO current implementation experiences increased sensitivity of the stabilisation process to mesh density. Therefore, the first solution aims to correct the biased density formulation to reach mesh-independency. The mesh sizes directly influence the upwind bias since the finer the mesh, the more the bias $\rho - \rho_U$ tends to zero in EQ. 2.3.13 and thus, the lower the amount of artificial viscosity and inversely. Thenceforth, the numerical scheme is not correctly stabilised anymore in the supersonic regions involving oscillations and/or no local results convergence with respect to the mesh and in worst cases, prevents solver convergence.

To withdraw this mesh dependency, starting from the density upwinding formulation developed by Hafez and Murman (EQ. 2.3.13), the concept is to compute the streamwise density gradient based on upwind numerical differentiation and multiply the upwind bias by a fixed length that has to be characterised in order to keep consistent units. Henceforth,

the upwind bias depends on a constant length in the entire flow field and a density gradient independent of the mesh grid.

$$\tilde{\rho} = \rho - \mu L \overleftarrow{\delta_s} \rho = \rho - \mu L \frac{(\rho - \rho_U)}{\Delta s}, \tag{3.1.1}$$

where $\tilde{\rho}$ is the upwinded density, ρ the physical density, $\mu = \mu_C \max\left(0, 1 - \frac{M_C^2}{M^2}\right)$ dependent on M_C a cut-off Mach number and μ_C an amplification of the density bias. In addition, L is the fixed length, Δs the streamwise cell size and ρ_U the density computed at an upwind element defined following the procedure detailed in Sec. 2.4.

The streamwise cell size Δs is approximated based on the distance between current and upwind element centroïd locations.

From then on, the finite element formulation Eq. 2.4.13 needs to be adapted using the new biased density formulation Eq. 3.1.1 in DARTFlo implementation.

$$\sum_e \int_{\Omega_e} \left(\rho_e - \mu \frac{L}{\Delta s}(\rho_e - \rho_U)\right) \nabla N_j \phi_j \cdot \nabla N_i \psi_i dV_e - \sum_e \int_{\Gamma e} \overline{\rho \nabla \phi_e} \cdot \mathbf{n}_e N_i \psi_i dS_e = 0, \quad \forall \psi_i, \tag{3.1.2}$$

where, the subscript e denotes elemental quantities, Ω_e is the element volume, Γ_e the element surface, N_k, ϕ_k and ψ_k are respectively the shape function, the potential and the test function for the node k and $\mathbf{n}$ the element unit normal vector.

Given the updated finite element formulation Eq. 3.1.2 for the fixed length correction, the residual vector can be updated,

$$R_i = \int_{\Omega_e} \left[\left(1 - \frac{L}{\Delta s}\mu\right)\rho_e + \frac{L}{\Delta s}\mu\rho_U\right] \partial_k \phi \partial_k N_i dV_e - \int_{\Gamma_e} \overline{\rho \partial_k \phi n_k} N_i dS_e, \tag{3.1.3}$$

which implies that the Jacobian matrix J can be analytically re-derived,

$$\begin{aligned} J = \frac{\partial R}{\partial \phi} &= \int_\Omega \frac{\partial}{\partial \phi}\{\tilde{\rho}\} \nabla\phi \cdot \nabla\psi dV + \int_\Omega \tilde{\rho} \frac{\partial}{\partial \phi}\{\nabla\phi \cdot \nabla\psi\} dV, \\ &= \int_\Omega \left(1 - \frac{L}{\Delta s}\mu\right) \frac{\partial}{\partial \phi}\{\rho \nabla\phi \cdot \nabla\psi\} dV \\ &+ \int_\Omega \frac{L}{\Delta s}\, \mu \left(\frac{\partial}{\partial \phi}\{\rho_U\} \nabla\phi \cdot \nabla\psi + \rho_U \frac{\partial}{\partial \phi}\{\nabla\phi \cdot \nabla\psi\}\right) dV \\ &+ \int_\Omega -\frac{L}{\Delta s}\,(\rho - \rho_U) \frac{\partial}{\partial \phi}\{\mu\} \nabla\phi \cdot \nabla\psi dV, \end{aligned} \tag{3.1.4}$$

where, the derivatives with respect to the potential ϕ are identical to the original implementation Eq. 2.4.26. Finally, based on the discretisation process Eq. 2.4.11 and potential derivative expressions, the discretised Jacobian matrix becomes,

$$\begin{aligned} J_{ij} &= \int_{\Omega_e} \left(1 - \frac{L}{\Delta s}\mu\right) \left[\frac{\partial \rho}{\partial \phi} \partial_k \phi \partial_k N_i + \rho_e \partial_k N_j \partial_k N_i\right] dV_e \\ &+ \int_{\Omega_e} \frac{L}{\Delta s}\, \mu \left[\frac{\partial \rho_U}{\partial \phi} \partial_k \phi \partial_k N_i + \rho_U \partial_k N_j \partial_k N_i\right] dV_e \\ &- \int_{\Omega_e} \frac{L}{\Delta s}\,(\rho_e - \rho_U) \left[\frac{\partial \mu}{\partial \phi} \partial_k \phi \partial_k N_i\right] dV_e, \end{aligned} \tag{3.1.5}$$

with, the discretised derivatives identical compared to the DARTFLO original implementation (EQ. 2.4.29).

3.2 Sonic density bias

Another solution to apply a mesh-independent bias on the physical density is to simulate an upwind influence with quantities computed at flow scale. The idea is to use a constant in the entire flow field to compute the density bias. In other words, changing the influence of the associated upwind element density ρ_U in the original DARTFLO density upwinding EQ. 2.3.13 by a constant independent on the position in the domain and on the mesh.

The process of upwinding the density consists in adding a positive bias to the physical density in order to retard it. By definition, the physical density decreases with respect to the Mach number in supersonic regions such that the bias computed with an upwind element in EQ. 2.3.13 is always positive inducing that,

$$\rho_U \geq \rho, \tag{3.2.1}$$

is always true. Therefore, the constant used to upwind the physical density has to always be larger or equal at any point in the supersonic regions to reach the same effect as density upwinding concept. As EQ. 2.1.12 suggests, in the supersonic regions, the highest value of the physical density is the one computed at sonic conditions. Henceforth, the formulation of the biased density is rewritten as follows,

$$\tilde{\rho} = \rho - \mu(\rho - \rho^*), \tag{3.2.2}$$

where $\tilde{\rho}$ is the upwinded density, ρ the physical density, $\mu = \mu_C \max\left(0, 1 - \frac{M_C^2}{M^2}\right)$ dependent on M_C a cut-off Mach number and μ_C an amplification of the density bias. Moreover, ρ^* denotes the density computed at sonic conditions thanks to the isentropic relations. The parameters at sonic conditions are determined by equalling the local Mach number at one in the isentropic flow relations such that, the following expressions can be derived,

$$\rho^* = \left(1 - \frac{\gamma - 1}{2} M_\infty^2 \left((a^*)^2 - 1\right)\right)^{1/(\gamma-1)}, \tag{3.2.3}$$

where, the critical speed of sound is determined by,

$$a^* = \sqrt{\frac{M_\infty^{-2} + (\gamma - 1)/2}{(\gamma + 1)/2}}, \tag{3.2.4}$$

with, M_∞ is the freestream Mach number and γ the heat capacity ratio.

Taking into account this change, the finite element formulation can be updated.

$$\sum_e \int_{\Omega_e} (\rho_e - \mu(\rho_e - \rho^*)) \nabla N_j \phi_j \cdot \nabla N_i \psi_i dV_e - \sum_e \int_{\Gamma e} \overline{\rho \nabla \phi_e} \cdot \mathbf{n}_e N_i \psi_i dS_e = 0, \quad \forall \psi_i, \tag{3.2.5}$$

where, the subscript e denotes elemental quantities, Ω_e is the element volume, Γ_e the element surface, N_k, ϕ_k and ψ_k are respectively the shape function, the potential and the test function for the node k and $\mathbf{n}$ the element unit normal vector.

Afterwards, based on the new finite element discretisation, the residual vector has to be reexpressed,

$$R_i = \int_{\Omega_e} \left[(1-\mu)\rho_e + \mu\rho^*\right] \partial_k\phi\partial_k N_i dV_e - \int_{\Gamma_e} \overline{\rho\partial_k\phi n_k} N_i dS_e, \tag{3.2.6}$$

which implies that the Jacobian matrix J can be analytically re-derived Eq. 3.2.6.

$$\begin{aligned} J = \frac{\partial R}{\partial \phi} &= \int_\Omega \frac{\partial}{\partial\phi}\{\tilde{\rho}\}\nabla\phi\cdot\nabla\psi dV + \int_\Omega \tilde{\rho}\frac{\partial}{\partial\phi}\{\nabla\phi\cdot\nabla\psi\}dV, \\ &= \int_\Omega (1-\mu)\frac{\partial}{\partial\phi}\{\rho\nabla\phi\cdot\nabla\psi\}dV \\ &+ \int_\Omega \mu\rho^*\frac{\partial}{\partial\phi}\{\nabla\phi\cdot\nabla\psi\}dV \\ &+ \int_\Omega -(\rho-\rho^*)\frac{\partial}{\partial\phi}\{\mu\}\nabla\phi\cdot\nabla\psi dV, \end{aligned} \tag{3.2.7}$$

where, the different derivatives are unchanged and computed based on Eq. 2.4.26. The discretised formulation of the Jacobian matrix becomes,

$$\begin{aligned} J_{ij} &= \int_{\Omega_e} (1-\mu)\left[\frac{\partial\rho}{\partial\phi}\partial_k\phi\partial_k N_i + \rho_e\partial_k N_j\partial_k N_i\right] dV_e \\ &+ \int_{\Omega_e} \mu\rho^*\partial_k N_j\partial_k N_i dV_e \\ &- \int_{\Omega_e} (\rho_e-\rho^*)\left[\frac{\partial\mu}{\partial\phi}\partial_k\phi\partial_k N_i\right] dV_e, \end{aligned} \tag{3.2.8}$$

with, identical derivatives as for the original DARTFlo implementation Eq. 2.4.29.

3.3 Switching function reformulation

The last solution to investigate is to change the formulation of the switching function. As explained in Sec. 2.3, Holst and Ballhaus [45] developed a new switching function formulation in response to numerical instabilities experienced by their solver due to pre-shock overshoots based on a previous switching function formulation similar to DARTFlo one.

Therefore, the expression of the switching function in Eq. 2.4.10 becomes,

$$\mu = \begin{bmatrix} 1-(\rho/\rho^*)^{\sigma_e} & M \geq 1 \\ 0 & M < 1 \end{bmatrix}, \tag{3.3.1}$$

where, ρ^* is the density computed at sonic conditions, ρ the physical density, M the local Mach number and σ_e a constant determined by numerical experiments. The value of this constant has been evaluated by Holst and Ballhaus [45] at six.

The expression of the residual vector (Eq. 2.4.24) as well as the Jacobian matrix (Eq. 2.4.25) stays unchanged, the only difference with the original DARTFlo implementation is the switching function formulation and its derivative with respect to the potential.

Particularised for supersonic regions, the derivative of the switching function with respect to the potential is computed based on Eq. 3.3.1.

$$\frac{\partial}{\partial \phi}\{\mu\} = -\sigma_e \left(\frac{1}{\rho_*}\right)^{\sigma_e} \rho^{\sigma_e - 1} \frac{\partial}{\partial \phi}\{\rho\}, \tag{3.3.2}$$

using the original expression for the density derivative Eq. 2.4.26.

4 Results

Within this chapter, a complete comparison between the different modified stabilisation solutions, the original DARTFLO density upwinding implementation and a reference solution is performed. Firstly, the analysis methodology is explained to detail the mesh convergence process and reference solution computations. In addition, the different test cases are described. Lastly, the different stabilisation methods are compared in the latter different test cases in order to assess the improvements.

4.1 Methodology

The thorough comparison of the different implementations in DARTFLO relies on two main biases. The first is mesh convergence analyses allowing to characterise how the global and local flight parameters evolve with respect to the mesh density in different test cases for the stabilisation solutions detailed in CHAP. 3. For consistency, three test cases have been set up in order to illustrate the behaviour of the implementations in different situations. They are described later in dedicated sections. The second bias is the use of a reference solution as a point of comparison to verify that the results accuracy has not been altered by cancelling the mesh-dependency.

4.1.1 Mesh convergence process

In each test case, a mesh convergence analysis is performed using each implementation. In DARTFLO, the mesh structure is an input parameter built with an external mesh generator. Henceforth, a mesh input file needs to be specified in configuration files. Currently, the code only supports GMSH native format mesh files [56].

The mesh density is commanded, based on different types of control points as illustrated in FIG. 4.1 and 4.2. Firstly, the farfield mesh control points define the element sizes at the domain boundaries. Secondly, control points are placed at the leading and trailing edge of the airfoils defining the different wing planforms of the problem.

The mesh convergence analysis is conducted by first fixing the farfield mesh size at different values and then, for each farfield mesh size, the leading and trailing edge mesh sizes are varied. To minimise the influence of the surface mesh evolution along the airfoil(s), the mesh sizes at the leading and trailing edge associated to the same airfoil are identically varied and will be denoted as surface mesh size. Note that all the mesh sizes are adimensionnalised by their associated chord length for consistency.

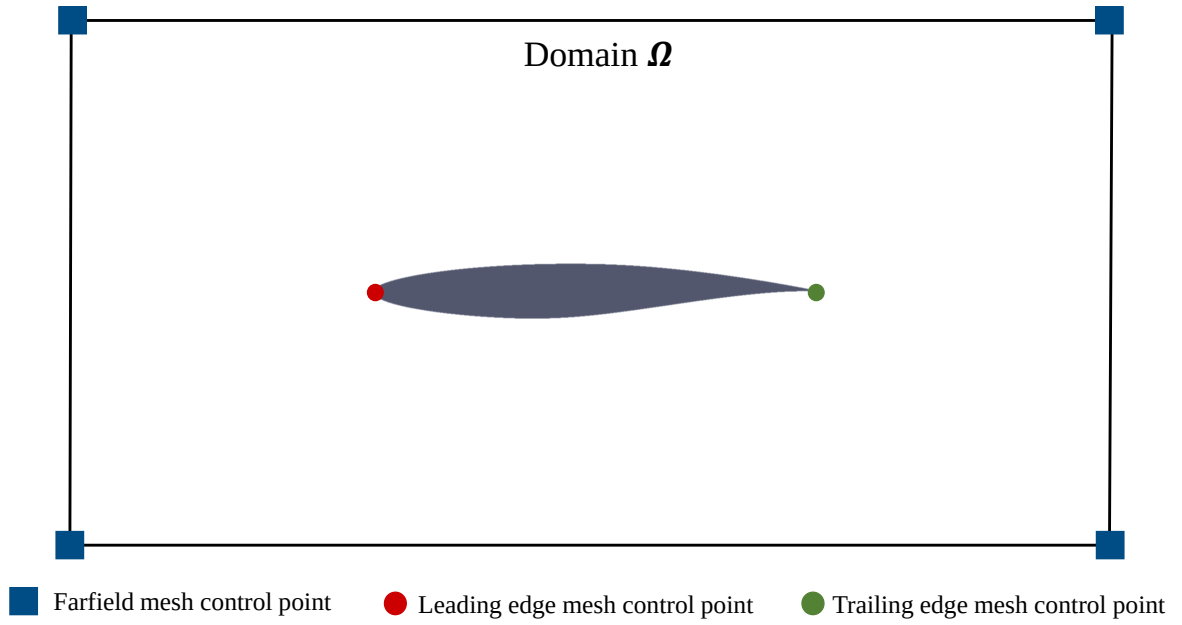

FIGURE 4.1: Different types of mesh control points in a two-dimensional case in GMSH.

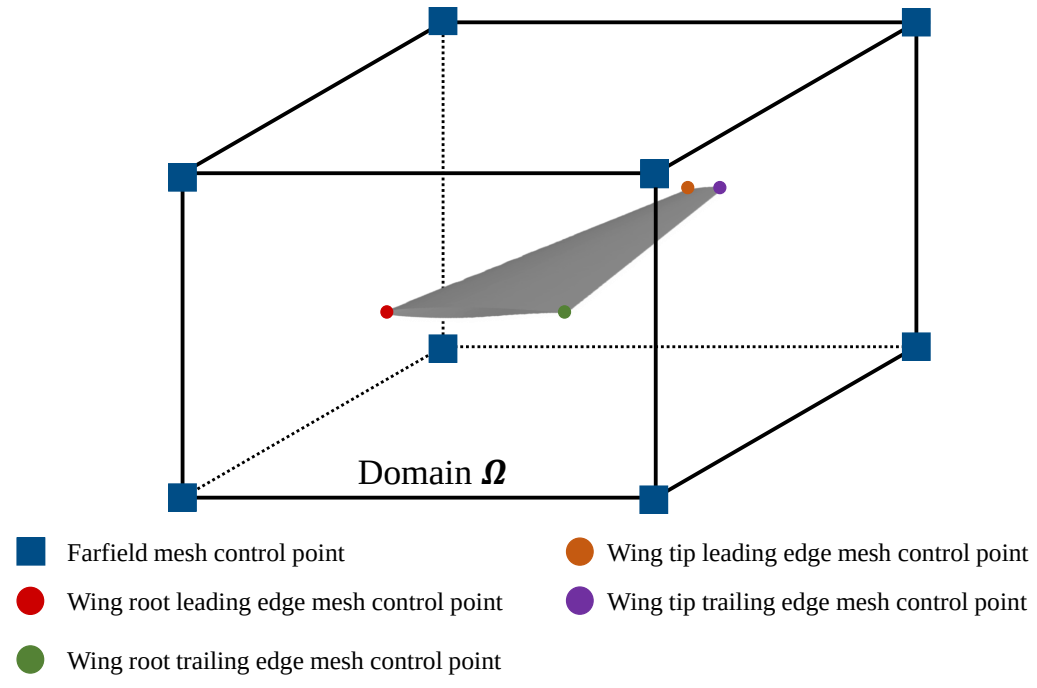

FIGURE 4.2: Different types of mesh control points in a three-dimensional case in GMSH.

Several parameters are studied in order to draw a clear comparison between the different implementations. Firstly, two global parameters, the lift and drag coefficients with respect to the mesh density providing first clues about the results convergence and stability of the implementation. Secondly, the pressure coefficient distribution is studied, which gives more information about the shock shape and the local behaviour in the supersonic regions.

4.1.2 Reference solution computation

The second bias to perform a complete comparison between the different implementations in DARTFLO is the computation of a reference solution with a state-of-the-art solver for each test case. The simulation tool selected for this research work is SU2, an open-source multiphysics simulation and design software [57]. This code enables to solve transonic flows based on different levels of aerodynamic fidelity whose *Euler* equations. The equations are spatially discretized on an unstructured dual-grid using a finite volume method with a cell-vertex based approach and multiple ready-to-use convective schemes. Two different convective schemes are going to be tested to derive an optimal numerical configuration. The first one is a central scheme, the Jameson-Schmidt-Turkel (JST) scheme [58] in which scalar dissipation can be introduced by second and fourth order dissipation coefficients. In addition, no limiters can be applied to this numerical scheme. The second is an upwind scheme, named ROE scheme. Several options are available to modify numerical parameters whose a dissipation relaxation coefficient and limiters which are studied.

An *Euler* modelling has been chosen as a point of comparison to observe whether withdrawing the mesh dependency with new implementations does not alter the results accuracy. Using a higher level of fidelity to compare the results enables to have an accuracy target to quantify if the updated stabilisation solutions do not lead the results in the wrong direction.

The reference solution evaluation can be divided into two phases. The first phase consists in defining converged mesh sizes for each test case providing relevant results. The latter is performed using the JST central scheme with the by-default second and fourth order dissipation coefficients since it offers a good compromise between accuracy and robustness. During the second phase, the specific numerical parameters of each scheme are investigated in order to determine the optimal simulation configuration and thus, a relevant reference solution. The selection criterion of the optimal numerical configuration follows the goal of obtaining a stable solution capturing a pressure drop as steep as possible by minimising over- and under-shoots on either side of the shock.

4.2 Weak shock test case

In this section, the stabilisation solutions are tested in a weak shock test case. Firstly, a case description is carried out. Then, the different stabilisation solutions are compared based on the different parameters detailed earlier. Lastly, the results are discussed.

4.2.1 Case description

The weak shock test case aims to set up a two-dimensional transonic flow with an embedded weak shock. By definition, a transonic flow is obtained for freestream Mach numbers between 0.8 and 1.2 [59]. In addition, a weak shock is characterised by a local Mach number upstream of the shock around 1.1 and a small change in the flow parameters.

Nowadays, commercial aircraft mostly fly at transonic regime. Specific airfoil shapes have been developed for this type of flow to obtain efficient aerodynamic behaviour in cruise. Supercritical airfoils are optimised for transonic cruise. A commonly used airfoil for solver validations is the RAE2822 since several experimental test cases have been performed in wind-tunnel [60].

From then on, the weak shock test case's characteristics are given in Tab. 4.1.

Airfoil	Mach number M [−]	Angle of attack α [°]	Dimensions
RAE2822	.72	1.	2D

Table 4.1: Flow characteristics of the weak shock test case.

This case configuration allows reaching the above-mentioned conditions as illustrated in the appendices Sec. B.1.

The computational domain is chosen to be rectangular whose dimensions have been determined through a convergence analysis by Crovato during DARTFlo development. Fig. 4.3 illustrates the conclusions drawn from this analysis. The different domain surfaces are placed at precise dimensions with respect to the airfoil. The upstream surface is located at a distance equal to five times the chord length with respect to the leading edge position. The downstream surface is also five times the chord length away from the trailing edge. Concerning the top and bottom surface, their dimensions have been defined as being equal to five times the chord length from the airfoil. Note that the Neumann boundary conditions applied at the farfield and body surfaces enabled to build a relatively small flow domain as the solution is less sensitive to such boundary conditions reducing the influence of the boundary surface on the solution.

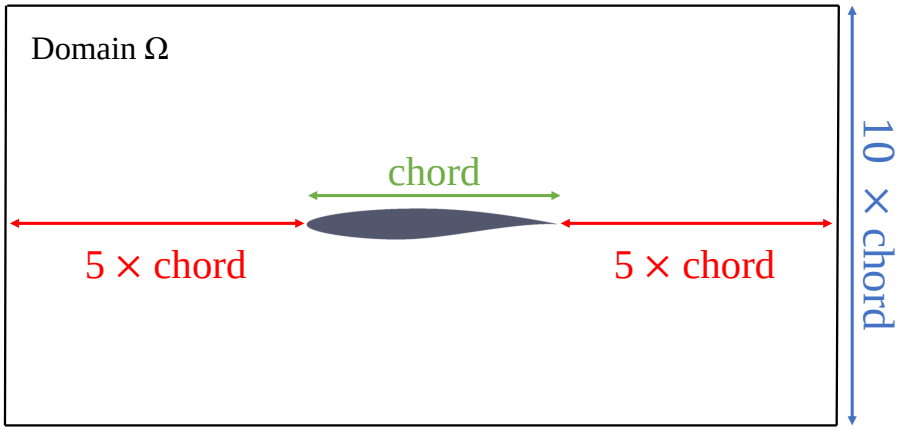

FIGURE 4.3: Computational domain dimensions in the two-dimensional weak shock test case.

4.2.2 Reference solution

The first phase in the reference solution computation is to perform a mesh convergence analysis on the aerodynamic coefficients with the aim of defining converged mesh sizes. The mesh convergence analyses have been conducted following the methodology described earlier. As explained in SEC. 4.1.2, these computations are carried out by SU2 based on the *Euler* equations using the Jameson-Schmidt-Turkel scheme with by-default scalar dissipation coefficients.

FIG. 4.4 illustrates the evolution of the aerodynamic loads with respect to the airfoil surface mesh size for different farfield mesh sizes. The influence of the farfield mesh size shows that values around 1 [−] can be considered as converged since the curves start to superimpose. In addition, a change in the curve slopes is noticed from a surface mesh size of 10^{-2} [−] which can be associated to the start of the convergence. However, a fully converged surface mesh size could not be experienced since from a value of 2×10^{-3} [−], the solver diverges due to infinite over- and under-shoots just before and after the shock. Therefore, the finest surface mesh size that has been simulated is considered as converged. The latter assumption is valid since the slope computed between two coarse surface mesh sizes (coarser than 10^{-2} [−]) and between two fine mesh sizes (finer than 10^{-2} [−]) is drastically reduced tending to zero.

As a conclusion, for the weak shock test case in SU2, the converged mesh characteristics are summarised in TAB. 4.2.

Farfield mesh size [−]	Surface mesh size [−]
1	.002

TABLE 4.2: SU2 converged mesh characteristics of the weak shock test case.

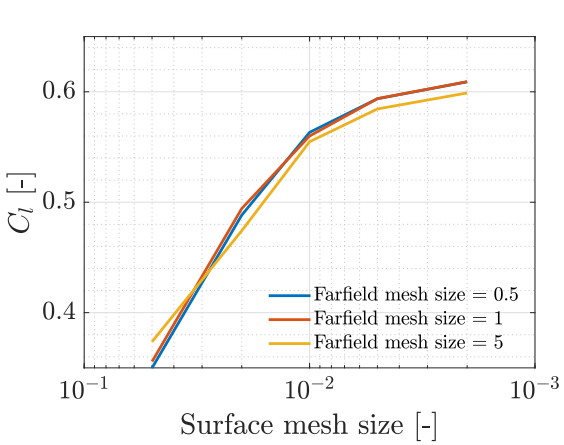

(a) Two-dimensional lift coefficient C_l [−] mesh convergence analysis.

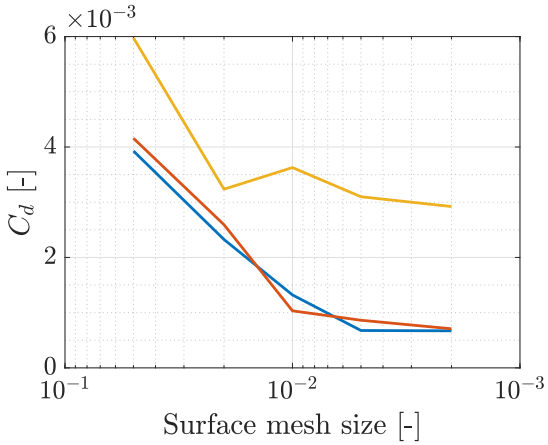

(b) Two-dimensional drag coefficient C_d [−] mesh convergence analysis.

FIGURE 4.4: Mesh convergence analysis on the aerodynamic coefficients performed with SU2 using the Jameson-Schmidt-Turkel convective scheme with by-default dissipation coefficients [57].

The second phase consists in studying the different convective schemes implemented in SU2 to determine the best numerical configurations. In the Jameson-Schmidt-Turkel scheme, the influence of the second and fourth order dissipation coefficients is characterised to determine the optimal combination for the weak shock test case. In order to do so, the 2^{nd} order dissipation coefficient is fixed at its default value (0.5) and the 4^{th} order one is variable to evaluate the optimal value. Then, the inverse process is performed, the 4^{th} order dissipation coefficient is fixed at its best-suited value and the 2^{nd} order one is studied.

FIG. 4.5 highlights that the larger the 4^{th} order dissipation coefficient, the smaller the under- and over-shoots at the shock. However, the largest value allowing the SU2 solver to converge is 0.12. Thenceforth, for the weak test case, the latter is set at 0.12.

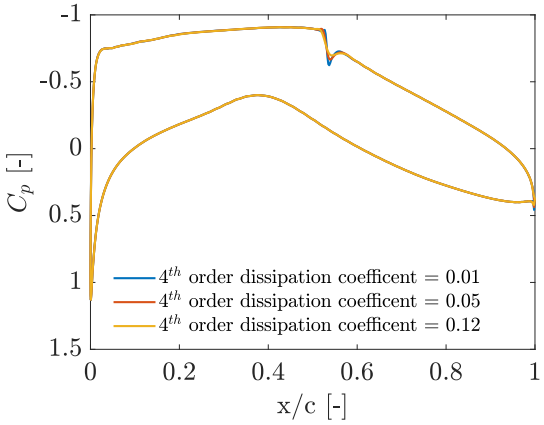

(a) Evolution of the pressure coefficient distribution.

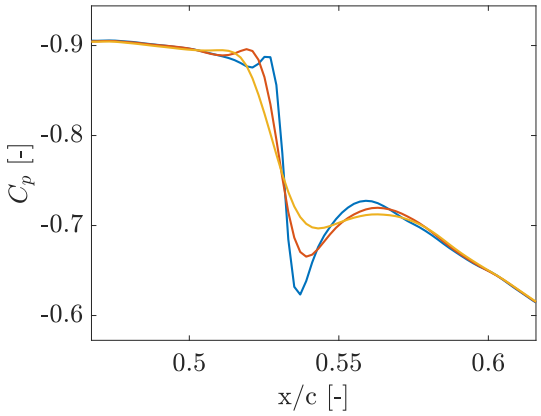

(b) Zoomed in pressure drop zone corresponding to the weak shock.

FIGURE 4.5: Influence study of the 4^{th} order dissipation coefficient in Jameson-Schmidt-Turkel scheme using SU2 based on the converged mesh with the by-default 2^{nd} order dissipation coefficient for the weak shock test case.

Since the optimal 4^{th} order dissipation coefficient has been determined, the 2^{nd} order one can be studied. As observed in FIG. 4.6, the influence of this coefficient is minimal such that its value is kept as the default one.

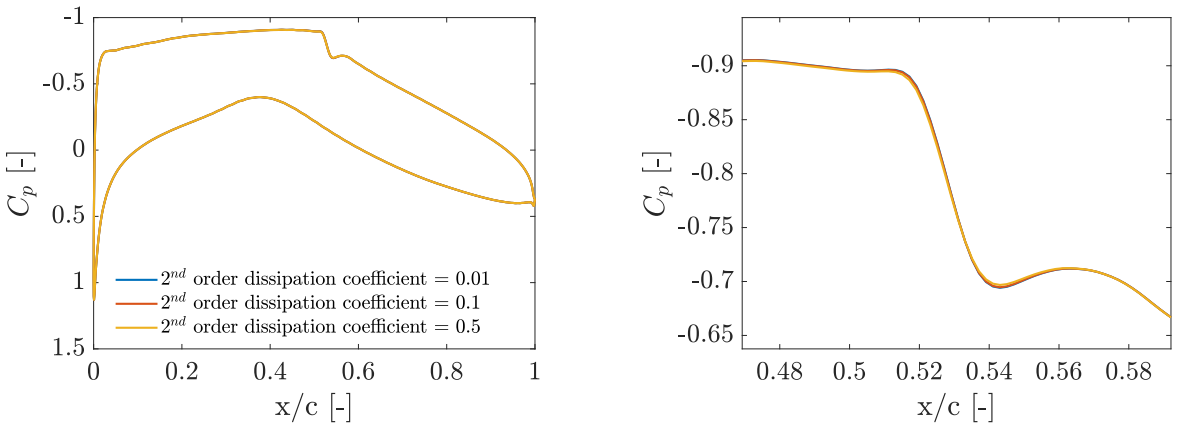

(a) Evolution of the pressure coefficient distribution.

(b) Zoomed in pressure drop zone corresponding to the weak shock.

FIGURE 4.6: Influence study of the 2^{nd} order dissipation coefficient in Jameson-Schmidt-Turkel scheme using SU2 based on the converged mesh with the optimal 4^{th} order dissipation coefficient for the weak shock test case.

In ROE upwind scheme, two numerical parameters have to be investigated. Firstly, the use of limiters is assessed. Then, the influence of the dissipation relaxation coefficient, 'ROE kappa', is analysed. In FIG. 4.7, it is observed that limiters have a reduced impact on the oscillations. However, limiters minimising the formation of over- and under-shoots across the shock are the Venkatakrishnan limiters [61].

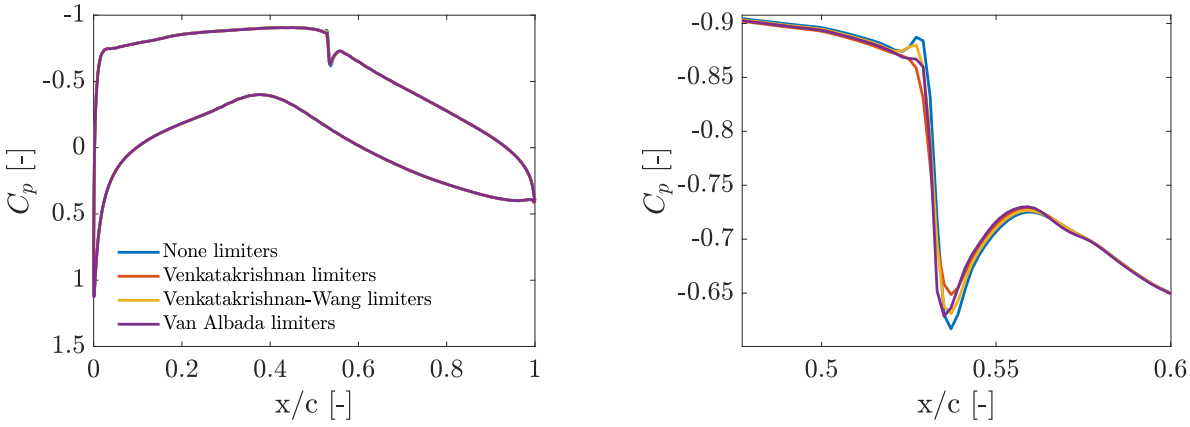

(a) Evolution of the pressure coefficient distribution.

(b) Zoomed in pressure drop zone corresponding to the weak shock.

FIGURE 4.7: Influence study of limiters in ROE scheme using SU2 based on the converged mesh with the default dissipation relaxation coefficient.

Thenceforth, FIG. 4.8 highlights the evolution of the pressure coefficient distribution with respect to the dissipation relaxation coefficient. As for the limiters, the latter does

not have a notorious impact on oscillations across the shock. However, as the goal is to minimise the over- and under-shoots, ROE kappa can be fixed at values smaller than 0.1, all providing similar results.

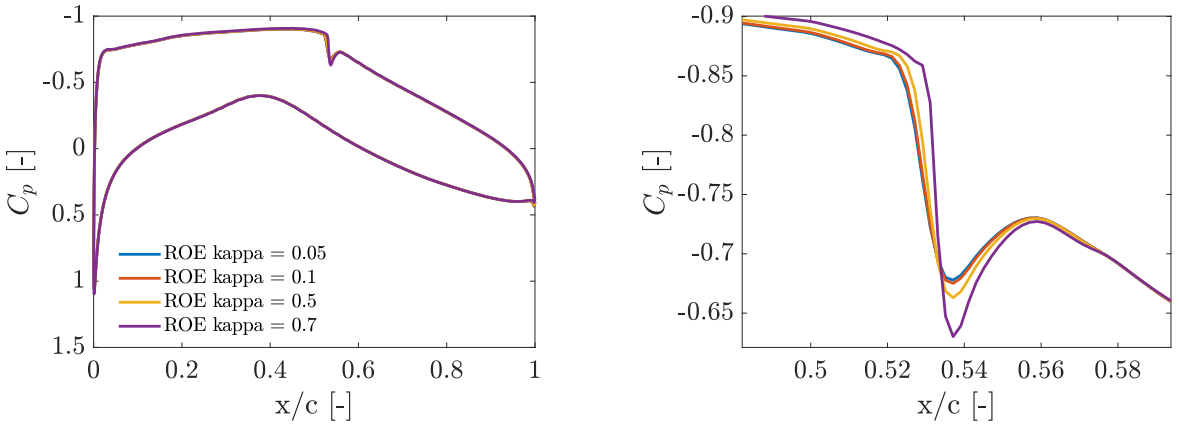

(a) Evolution of the pressure coefficient distribution.

(b) Zoomed in pressure drop zone corresponding to the weak shock.

FIGURE 4.8: Influence study of the dissipation relaxation coefficient ROE kappa in ROE scheme using SU2 based on the converged mesh with Venkatakrishnan limiters for the weak shock test case.

The optimal numerical configurations based on the two different schemes are compared to finally determine the reference solution for the weak shock test case. The configuration respecting the selection criterion described in SEC. 4.1.2 is the JST central scheme with second and fourth order dissipation coefficients respectively equal to $(0.5, 0.12)$. As illustrated in FIG. 4.9, the optimal JST numerical configuration offers a relatively steep shock capturing while providing minimal oscillations across the shock compared to optimal ROE configuration.

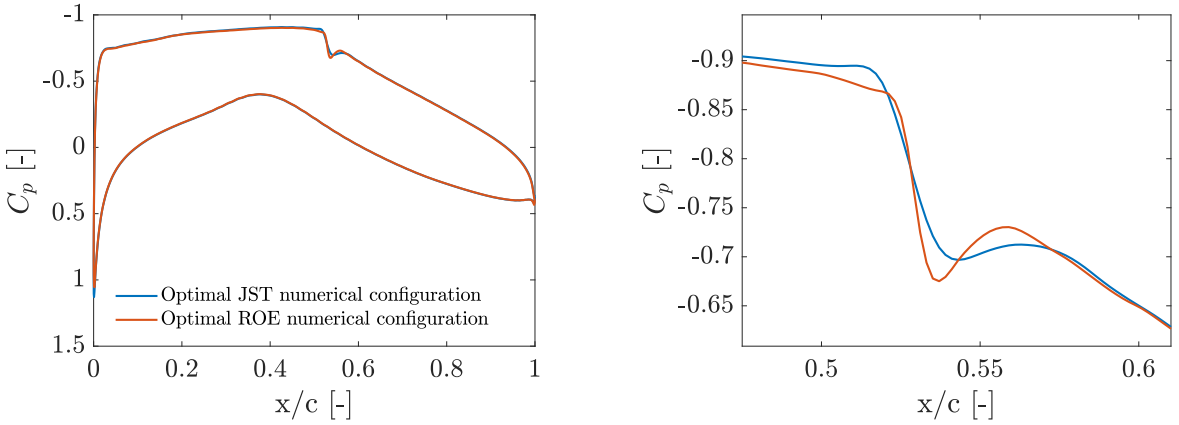

(a) Evolution of the pressure coefficient distribution.

(b) Zoomed in pressure drop zone corresponding to the weak shock.

FIGURE 4.9: Comparison between the optimal numerical configuration determined for both JST and ROE scheme in the weak shock test case context using SU2 and the converged mesh.

As a conclusion, the reference solution for the weak shock test case is defined using SU2 based on the *Euler* equations discretised with Jameson-Schmidt-Turkel scheme setting with second and fourth order dissipation coefficients defined at $(0.5, 0.12)$.

Aerodynamic coefficient	Value
C_l $[-]$	.61
C_d $[-]$	.00089

(a) Aerodynamic coefficients of the reference solution.

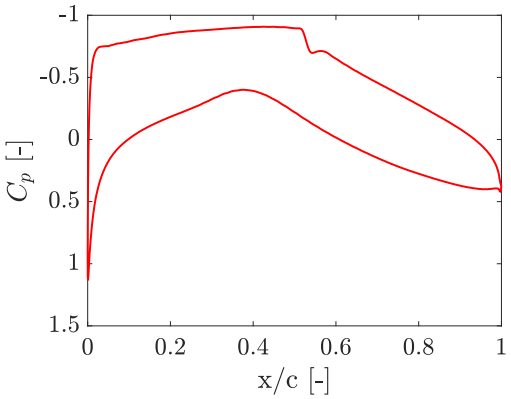

(b) Pressure coefficient distribution of the reference solution.

FIGURE 4.10: Characteristics of the reference solution for the weak shock test case.

4.2.3 Fixed length selection

As explained in the solution description of the fixed length correction, the fixed length has to be determined in relation to the test case.

In this section, the influence of the fixed length L $[m]$ on the aerodynamic coefficients is studied in a weak shock test case. The most suitable value is evaluated with the objective of performing a mesh convergence analysis using the fixed length correction described in SEC. 3.1.

For different refined mesh configurations, the fixed length L $[m]$ is varied to quantify its impact. For a weak shock test case in DARTFLO, it has been demonstrated that a mesh density of around 6000 elements is already enough to accurately capture the shock [27]. This mesh density corresponds to a farfield mesh size of 1 and a surface mesh size equal to 1/200 of the chord length. For the sake of completeness, a configuration twice as coarse is used as the coarsest mesh configuration, corresponding to a farfield of 1 and a surface mesh size equal to 1/100 of the chord length (3739 elements). From this starting mesh configuration, the element sizes are refined to build the different fixed mesh configurations used for the fixed length analysis.

FIG. 4.11 represents the evolution of the aerodynamic coefficients with respect to the fixed length L $[m]$ for different mesh configurations. The first important interpretation from the analysis is the independence of the aerodynamic coefficient with respect to the set length. In the length range allowing the solver convergence, the variation of the parameters is null. In addition, the comparison between different farfield mesh sizes illustrates that

its impact is negligible since the convergent length ranges do not vary when the farfield mesh is refined. Concerning the influence of the surface mesh size, it can be noticed that the finer the surface mesh size, the smaller the fixed lengths. However, for highly refined surface mesh sizes, the ranges allowing solver convergence seem to stabilise.

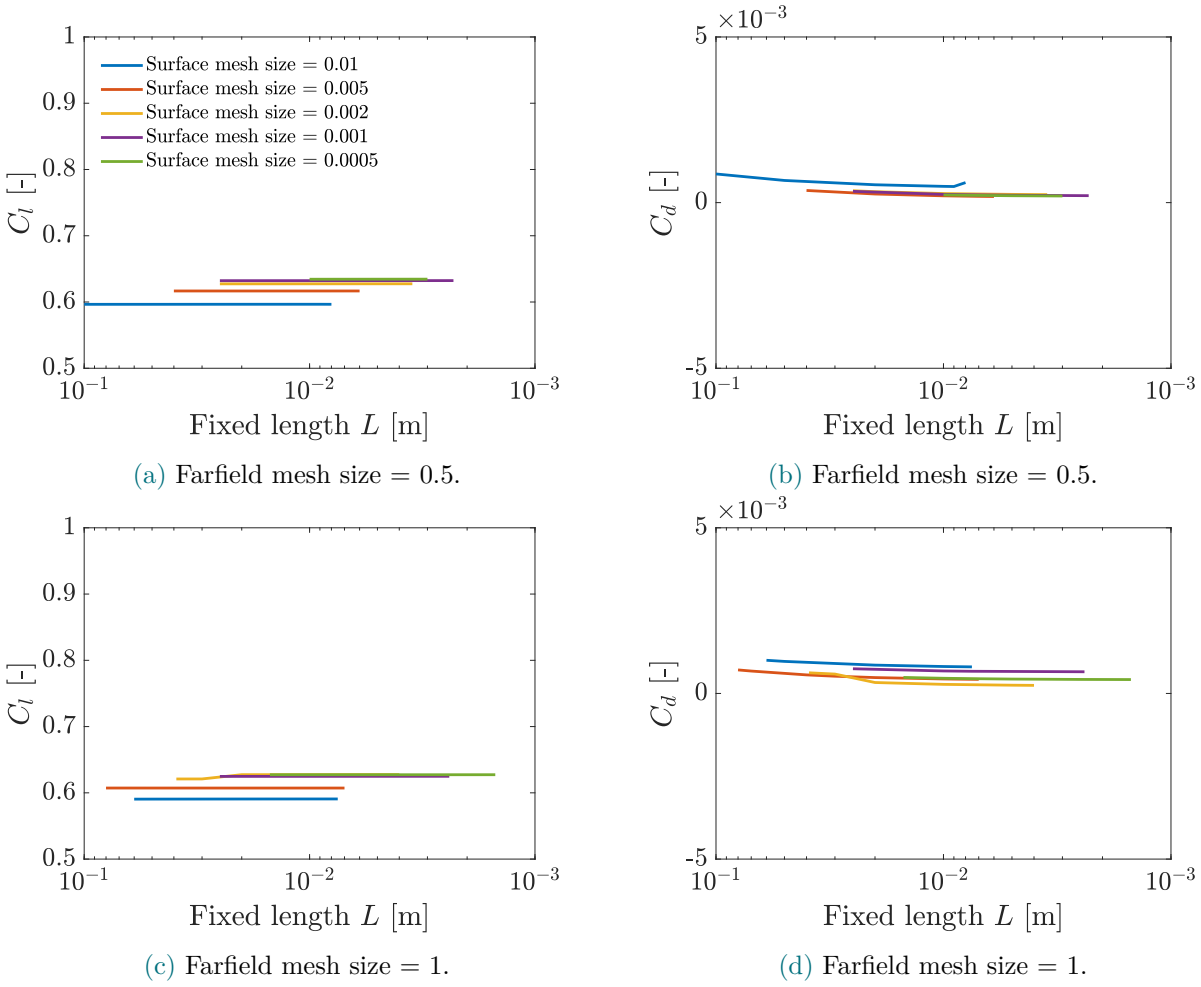

(a) Farfield mesh size = 0.5.

(b) Farfield mesh size = 0.5.

(c) Farfield mesh size = 1.

(d) Farfield mesh size = 1.

FIGURE 4.11: Evolution of the aerodynamic coefficients with respect to the fixed length L for different fixed mesh size configurations in the weak shock test case using the fixed length correction implementation in DARTFLO 3.1.

To approximately determine an optimal fixed length in a weak shock test case, for each mesh configuration, the average of the length range is computed. The results are summarised in FIG. 4.12. For highly refined mesh configurations, the fixed length converges to a value between 0.005 and 0.01 $[m]$. Therefore, it can be concluded that for a weak shock test case, the fixed length can be set in the latter range. Henceforth, the fixed length L $[m]$ is defined based on FIG. 4.12 with the finest mesh configuration leading to $L = 0.0065$ $[m]$. This value is used in the next section to perform the mesh convergence analysis using the fixed length correction implementation.

However, a further analysis concerning the determination of the fixed length should be performed in order to assess the selection process.

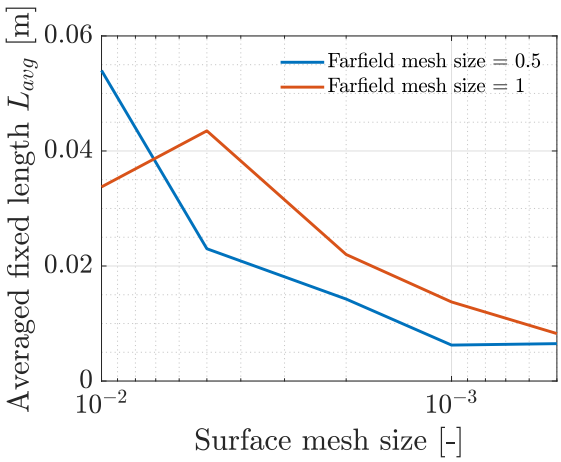

FIGURE 4.12: Evolution of the averaged converging fixed length for the different mesh configurations in the weak shock test case.

4.2.4 Results comparison

In this section, the original and new stabilisation implementations are compared in the context of the weak shock test case. Firstly, the evolution of the lift C_l and the drag C_d coefficients with respect to the mesh density is studied to characterise the mesh-dependency of the original implementation and observe the improvements of the new stabilisation processes described in CHAP. 3. Secondly, the pressure coefficient C_p distributions with respect to mesh sizes are compared to gain insight into the local behaviour of the flow computed based on the different implementations. The process of analysing the results is conducted in two phases. First, the original implementation is studied in order to characterise the mesh dependency of the global and local results. Then, the results obtained with the new implementations are compared to the original to highlight possible improvements.

Lift and drag coefficients

In the first instance, the lift coefficient is analysed. FIG. 4.13 illustrates the evolution of the lift coefficient C_l with respect to the mesh density for the different implementations in the weak shock test case. The original DARTFLO implementation results are shown in FIG. 4.13a. Concerning the mesh at the domain boundaries, farfield mesh sizes from around one are considered as converged since the associated curves are almost superimposed. Whereas, a farfield mesh size equal to 3 provides not converged results since the yellow curve in FIG. 4.13a has a completely different behaviour from the other two farfield mesh sizes. As for the surface mesh size, a change in the curve slopes is detected from 10^{-2} [−] related to the start of the convergence. However, depending on the farfield mesh size, DARTFLO solver stops converging for surface mesh sizes $\mathcal{O}(10^{-3})$ [−] *i.e.* the mesh could not be further refined. Note that for all the simulations, the mesh has been refined as long as the solver was converging.

The results obtained with the original DARTFLO implementation can be compared with those computed with SU2. It can be observed that DARTFLO globally seems to converge to a similar range of lift as SU2 taking into account the different levels of fidelity that both solvers represent and that DARTFLO results have not already fully converged at the surface mesh sizes from which it stops converging.

The fixed length correction lift coefficient evolution is illustrated in FIG. 4.13b. A great improvement of the mesh convergence can be highlighted since the surface mesh size can be refined by one order of magnitude further compared to the original implementation. The latter leads to surface mesh sizes refined to $\mathcal{O}(10^{-4})$ [−]. In this case, the results convergence is clearly observed since the curve slope tends to zero for surface mesh sizes finer than 5×10^{-3} [−]. Note that the conclusion for the farfield mesh size convergence is also valid for this fixed length correction implementation. Concerning the comparison with SU2 reference lift coefficient, the lift curves converge to similar values taking into account the different levels of fidelity on which both solvers are based. For example, the relative error between the SU2 reference lift coefficient and the one computed with the finest mesh is around 4.22%.

The lift coefficient evolution computed based on the sonic density bias solution is illustrated in FIG. 4.13c. As for the previous solution, the mesh convergence is highly improved given that the surface mesh refinement can be performed to almost 10^{-4} [−] while keeping a converging solver. In addition, the farfield mesh convergence is still observed for values around one. Based on this new implementation, it can be deduced that the lift coefficient computed with the finest mesh gets closer to the reference one than for the previous solution since the relative error between the two decreases to 3.14%.

FIG. 4.13d pictures the lift evolution with respect to the mesh density based on the switching function reformulation. The first observation is that the convergence improvement compared to the other stabilisation solutions is lower since the surface mesh can be refined to the order of the original density upwinding implementation ($\mathcal{O}(10^{-3})$ [−]). This stop in the mesh convergence leads to the same conclusions drawn for the original implementation. The surface mesh sizes, at which the DARTFLO solver does not converge, result in not fully converged lift coefficients.

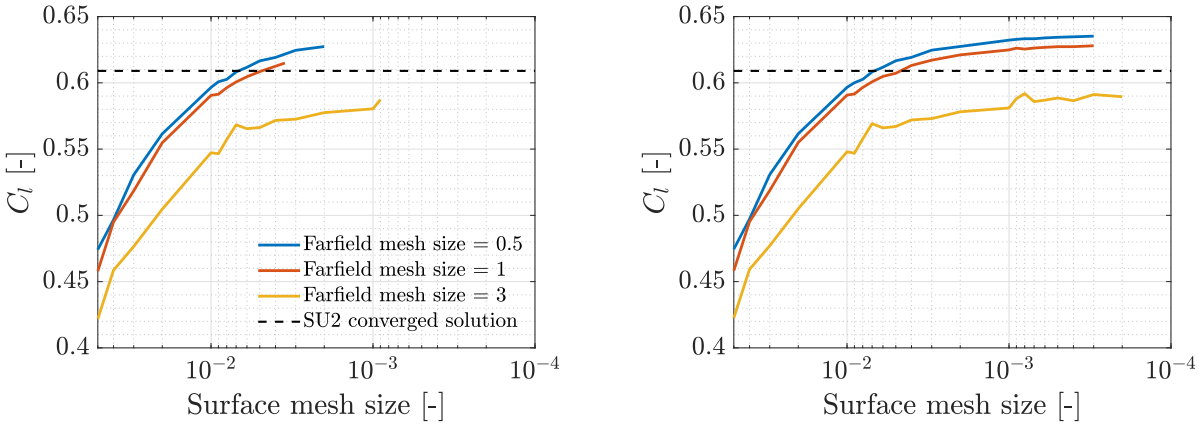

(a) Original DARTFLO implementation 2.4.2.

(b) Fixed length correction 3.1 with $L = 0.0065$.

(c) Sonic density bias 3.2.

(d) Switching function reformulation 3.3.

FIGURE 4.13: Evolution of the lift coefficient C_l with respect to the farfield and surface mesh sizes for the different stabilisation solutions in the weak shock test case.

In a second phase, the evolution of the drag coefficient with respect to the mesh density is studied in FIG. 4.14. The first observation confirmed with the drag coefficient evolutions for each stabilisation solutions is the convergence of the farfield mesh size. Values finer or equal to one are converged while coarser farfield mesh sizes do not provide relevant results. Indeed, chaotic drag oscillations are observed for coarse farfield mesh sizes. In addition, the start of the convergence for surface mesh finer than 10^{-2} [−] is endorsed since highly variable drag coefficients are observed for coarser surface mesh sizes. After this threshold, the drag coefficient curves stabilise.

The convergence improvements provided by the fixed length correction and the sonic density bias are verified in the drag coefficients graphs. Much finer surface mesh sizes can be reached with these two solutions than the original one and the switching function reformulation. The results convergence is clearly illustrated by the curve slope change which turns to zero from surface mesh sizes finer than 10^{-2} [−] and farfield mesh sizes smaller or equal to one.

The small oscillations observed for farfield mesh size equal to one can be explained by the order of magnitude of the drag coefficient ($\mathcal{O}(10^{-4})$ [−]). Since the fluid is considered

to be inviscid, the only drag contribution is the pressure drag generated by the size and the shape of the immersed body. However, in the cases of streamlined bodies as airfoils or wings, the pressure drag represents a small portion of the total physical drag. Consequently, the order of drag magnitude is very low which results in a high degree sensitivity of the drag to numerical errors and mesh configurations.

Lastly, in all configurations, the drag estimate approximately clings to the reference solution, taking into account the different levels of fidelity represented in both solvers.

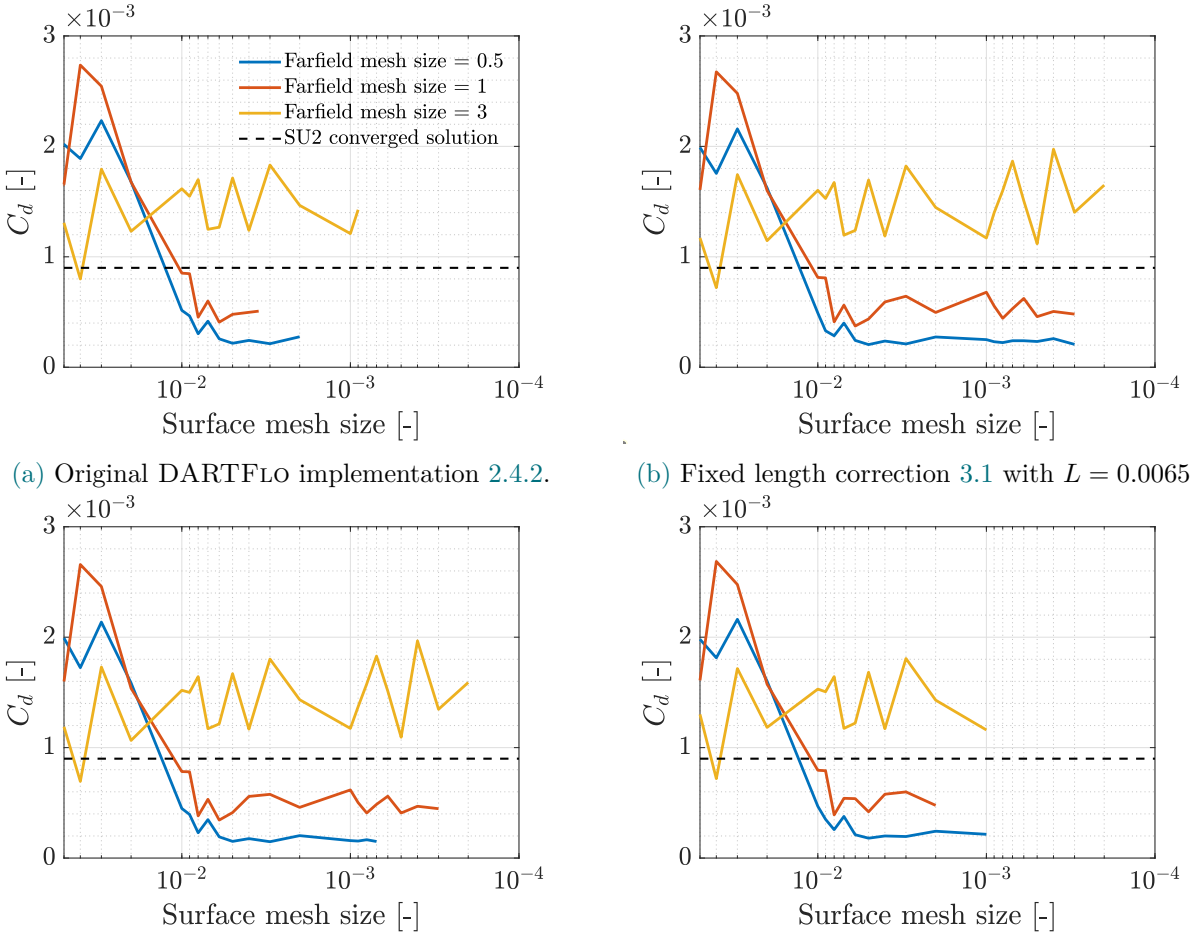

(a) Original DARTFLO implementation 2.4.2.

(b) Fixed length correction 3.1 with $L = 0.0065$.

(c) Sonic density bias 3.2.

(d) Switching function reformulation 3.3.

FIGURE 4.14: Evolution of the drag coefficient C_d with respect to the farfield and surface mesh sizes for the different stabilisation solutions in the weak shock test case.

Pressure coefficient distributions

The section aims at analysing the influence of the mesh density on the pressure coefficient distributions. For different farfield mesh sizes, the surface mesh size is varied. FIG. 4.15 illustrates the evolution of the pressure distribution with respect to the surface mesh size for a farfield mesh size equal to 1/2 of the airfoil chord length with the different stabilisation implementations.

First, the original DARTFLO density upwinding implementation is studied. FIG. 4.15a confirms that the original stabilisation process experiences high mesh sensitivity. Despite

the convergence of the shock position, the pressure distribution does not converge when the mesh is refined. The shock capturing varies with respect to the mesh density since the pressure distribution on around the shock keeps evolving even for highly refined surface meshes. This reflects a dependence on the mesh size of the stabilisation process since the results do not tend to one single pressure distribution. Another important point to note is the appearance of short-wavelength oscillations in the supersonic zone of the airfoil suction side. The latter prove that when the surface mesh size is refined, the numerical scheme becomes unstable which prevents the solver from converging for finer surface mesh sizes. This is explained by the decrease of the density upwinding stabilisation effect when the mesh is refined as explained previously. The density upwinding being mesh-dependent, the more the mesh is refined, the less the artificial viscosity is added to the numerical scheme which implies that the supersonic regions are less and less stabilised involving appearance of oscillations in the supersonic zones.

In addition, the shock position predicted by the original DARTFLO implementation is delayed by more or less 5% of the chord length with respect to the computations with the *Euler* equations in SU2. The shock strength is also larger than SU2 estimates. This is due to the different levels of aerodynamic fidelity which lead to different approximations.

The fixed length correction pressure distribution evolution for a farfield mesh size equal to 1/2 of the chord length is illustrated in FIG. 4.15b. A real improvement in the local flow behaviour is observed. Firstly, the oscillations occurring in the supersonic regions are fully cancelled, which enables the surface mesh to be much further refined while conserving a converging solver as characterised in the lift and drag analysis. Secondly, in addition to the convergence of the shock position, the shock capturing stops varying when the surface mesh is enough refined. In other words, the pressure distributions are identical when the surface mesh size is finer than 1/100 of the chord length as depicted in FIG. 4.15b by the associated curves. Thenceforth, the improvements observed in the lift and drag analysis are confirmed with the pressure coefficient distributions.

Concerning the sonic density bias adaptation, the associated pressure coefficient evolutions are plotted in FIG. 4.15c. In the lift and drag analysis, a convergence improvement has been noticed allowing to further refine the surface mesh on the airfoil. However, it can be observed that no shock is captured since no rapid pressure change is detected by the solver. The artificial viscosity added by the upwind bias computed with the density evaluated at sonic conditions is too large which leads to highly diffused shock capturing.

FIG. 4.15d shows the evolution of the pressure coefficient distribution with respect to the mesh density for the switching function reformulation implementation. Similar problems as for the original DARTFLO implementation arise. Despite the shock position convergence, the pressure distributions do not converge during the mesh refinement since

over- and under-shoots increase as the surface mesh is refined until the solver convergence is prevented. Moreover, this stabilisation solution also experiences short-wavelength oscillations in the supersonic region of the flow. Thenceforward, a mesh-dependency can be retrieved based on these observations which place this implementation in front of the same problem as with the original density upwinding solution.

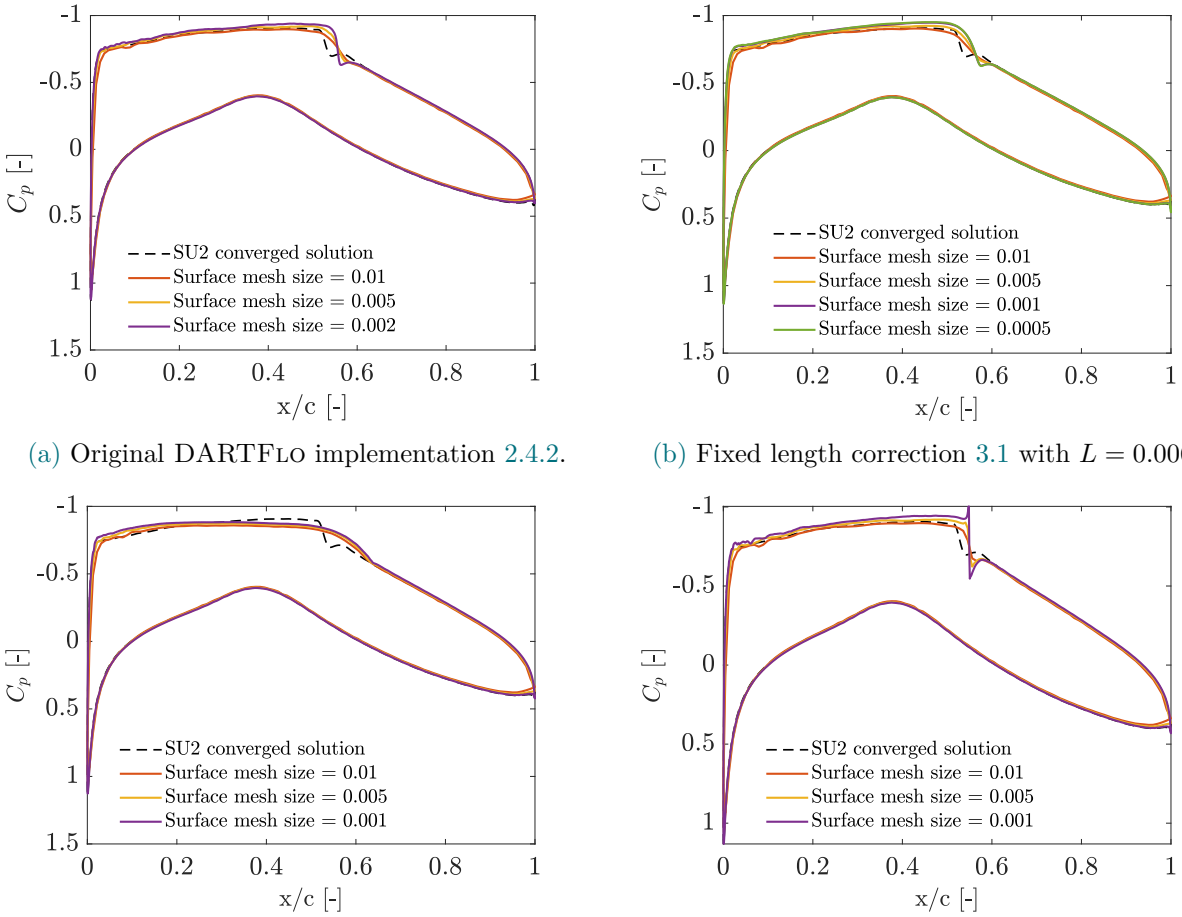

(a) Original DARTFLO implementation 2.4.2.

(b) Fixed length correction 3.1 with $L = 0.0065$.

(c) Sonic density bias 3.2.

(d) Switching function reformulation 3.3.

FIGURE 4.15: Evolution of the pressure coefficient distribution C_p with respect to the surface mesh size with a **fixed farfield mesh size at 1/2 of the chord length** for the different stabilisation solutions in the weak shock test case.

The farfield mesh size is increased to 1 of the chord length in FIG. 4.16 where the pressure distribution evolutions are recomputed for all the stabilisation solutions. First, the impact of the farfield mesh size on the pressure distribution is evaluated in the original DARTFLO implementation case. FIG. 4.16a shows that when the farfield mesh gets coarser, the shock capturing starts to degenerate, the shock position and the pressure distribution become highly variable depending on the surface mesh size and the mesh is too diffusive to correctly capture any shock since no steep pressure drop is discerned. In addition, the oscillations in the supersonic regions observed in the 0.5 farfield mesh case are slightly accentuated.

The fixed length correction results illustrated in FIG. 4.16b for a farfield mesh equal to 1 of the chord length still bring out improved results compared to the original implementation. The pressure distribution as well as the shock location respectively converge towards one single curve or chordwise position when the surface mesh is sufficiently refined. However, long-wavelength oscillations are observed before the shock in the supersonic zone, probably due to the farfield mesh which becomes slightly too coarse to maximise the results accuracy inducing a large growth mesh rate.

Concerning the sonic density bias solution, as described in the previous mesh configuration, no shock capturing is enabled with this stabilisation solution since the artificial viscosity introduces too much diffusion. The latter conclusion is still valid for a farfield mesh size equal to one of the chord length.

FIG. 4.16d depicts the evolution of the pressure distribution with respect to the surface mesh for a farfield mesh size of one of the chord length computed with the switching function reformulation. The same conclusions as for the original implementation can be drawn *i.e.* the shock capturing is degenerated when the farfield mesh size becomes coarse. The shock location does not converge anymore with respect to the surface mesh size nor the pressure distribution. In addition, the short-wavelength oscillations in the leading edge region of the airfoil suction side are still appearing as well as large wavelength in all the supersonic regions. One improvement with respect to the equivalent mesh configuration with the original implementation is the shock capturing. Even if no convergence is observed for the pressure distribution curve and the shock position, a pressure drop is observed transcribing a shock capturing.

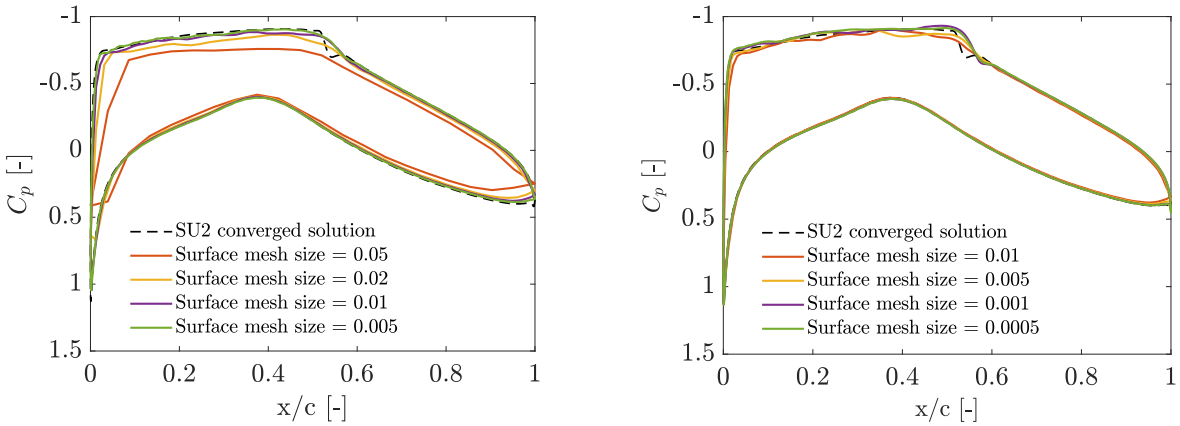

(a) Original DARTFLO implementation 2.4.2.

(b) Fixed length correction 3.1 with $L = 0.0065$.

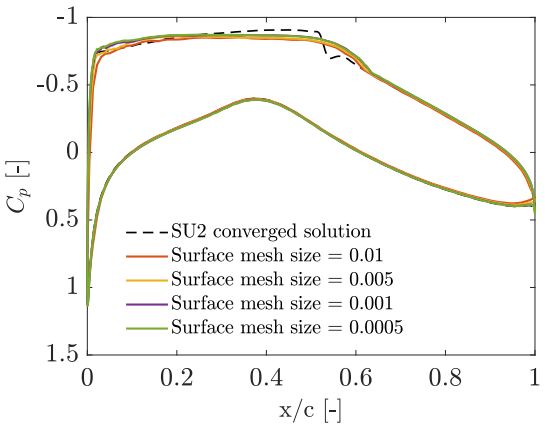

(c) Sonic density bias 3.2.

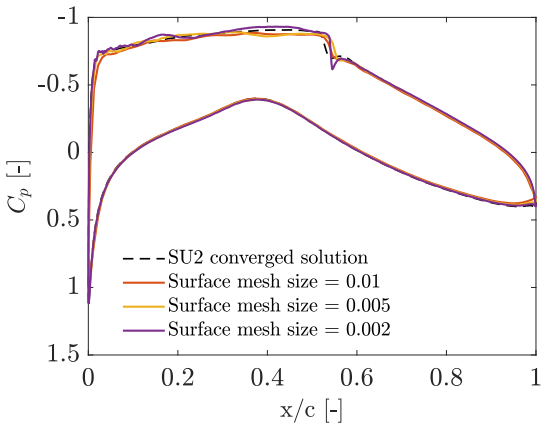

(d) Switching function reformulation 3.3.

FIGURE 4.16: Evolution of the pressure coefficient distribution C_p with respect to the surface mesh size with a **fixed farfield mesh size at 1 of the chord length** for the different stabilisation solutions in the weak shock test case.

Lastly, the farfield mesh size gets coarser to 3 times the chord length as illustrated in FIG. 4.17. For each stabilisation implementation, heavy oscillations emerge in the supersonic region of the airfoil suction side. A too coarse farfield mesh is the only reason producing these oscillations. From a certain threshold of mesh size at the domain boundaries, the mesh growth rate between the surface and the farfield is too large. This implies that the mesh quickly becomes too coarse to capture any physics in the supersonic regions. In other words, the evolution from the surface where the mesh is highly refined to the farfield at 3 times the chord length is too fast such that even in the suction side near-field, the mesh is too coarse.

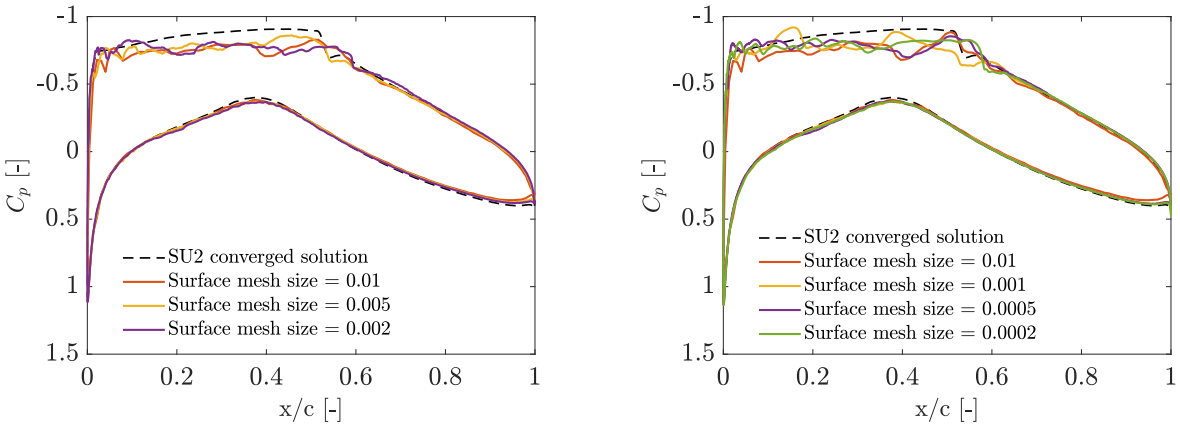

(a) Original DARTFLO implementation 2.4.2.

(b) Fixed length correction 3.1 with $L = 0.0065$.

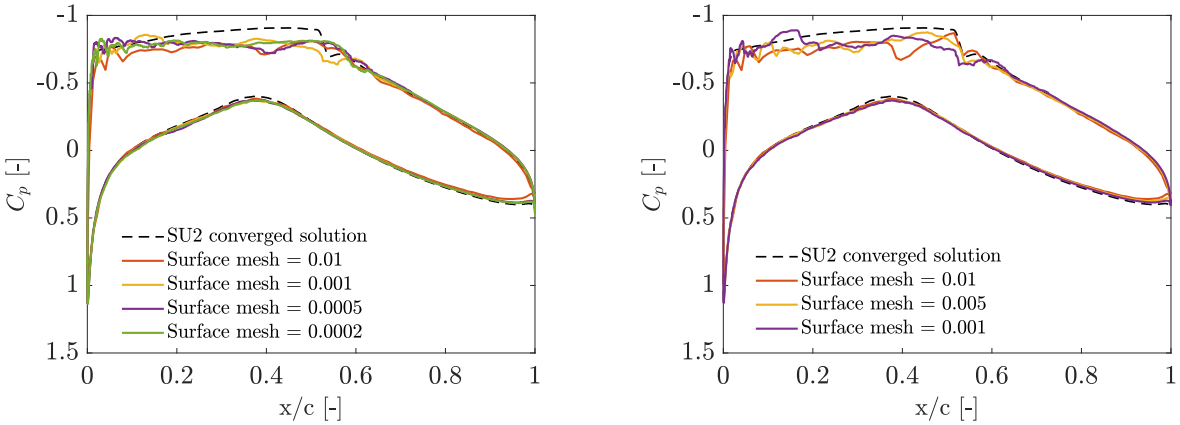

(c) Sonic density bias 3.2.

(d) Switching function reformulation 3.3.

FIGURE 4.17: Evolution of the pressure coefficient distribution C_p with respect to the surface mesh size with a **fixed farfield mesh size at 3 of the chord length** for the different stabilisation solutions in the weak shock test case.

4.2.5 Discussion

In this section, the results obtained for the different stabilisation processes in the weak shock test case are discussed.

In the weak shock test case, original DARTFLO implementation and more precisely, the density upwinding demonstrated its high mesh-dependency through oscillations appearing in the supersonic zone when the surface airfoil mesh is refined and the variable pressure distribution depending on the mesh configuration. The latter phenomena imply that over- and under-shoots are progressively created during the refinement of the mesh which consequently kills the solver convergence. However, reliable results can be computed for well-chosen mesh sizes. The farfield mesh size must be imperatively finer than 1 of the chord length in order to avoid as much as possible strong oscillations in the supersonic regions and to decrease the mesh growth rate. In addition, the start of the convergence has been observed from surface mesh sizes finer than 1/100 of the chord such that the flow physics can be more or less correctly captured in the most sensitive regions of the flow.

Although reliable results can be reached for precise mesh sizes, the local flow parameters stay highly mesh-dependent such that the results vary from one mesh size to another.

The analysis of the fixed length correction demonstrated that improved results could be achieved in the weak shock test case. The mesh-dependency clues cited in the original DARTFlo implementation analysis are withdrawn. Mesh convergence is facilitated by increasing the solver refinement capability. In addition, converged mesh sizes enable to reach solutions which do not vary with the mesh anymore. Mesh-independent results are attained by setting the farfield mesh sizes at finer values than 1 coupled with surface mesh sizes smaller than 1/1000 of the chord length. Given the improvements derived by this stabilisation solution, it should be further investigated in other test cases.

Concerning the sonic density bias, it illustrated during the lift and drag coefficients analysis that improvements were possible to increase the mesh convergence range. However, the local analysis highlighted no shock capturing due to high numerical diffusivity. Therefore, this stabilisation solution is discarded from further analysis.

Lastly, the last stabilisation solution that has been implemented is the reformulation of the switching function. Both global and local analyses proved that similar mesh-dependency problems were observed in the weak shock test case. The problem experienced by DARTFlo with its original density upwinding has simply been reformulated in another form. Indeed, the reformulated switching function is a rearranged expression of the original one based on equivalent flow parameters. Consequently, this stabilisation implementation is excluded from further analyses.

4.3 Strong shock test case

In this section, the stabilisation solutions are tested in a strong shock test case. Firstly, the strong shock test case is described. Then, the different stabilisation solutions are compared based on the different parameters detailed earlier. Lastly, the results are discussed.

4.3.1 Case description

The strong shock test case aims to set up a two-dimensional transonic flow with an embedded strong shock within the local Mach number validity range for the potential assumption ($M_n < 1.3$). The Mach numbers corresponding to transonic flows is identical to the ones defined for the previous test case. Concerning the shock strength, a strong shock is considered as a large change in the flow parameters and a local Mach number just before the shock around 1.2 - 1.25. The same airfoil as the one used in the weak shock test case is considered, the RAE2822 supercritical airfoil. These requirements lead to the test case configuration summarised in Tab. 4.3.

Airfoil	Mach number M [−]	Angle of attack α [°]	Dimensions
RAE2822	.73	1.	2D

TABLE 4.3: Flow characteristics of the strong shock test case.

As illustrated in appendices SEC. B.2, the configuration detailed in TAB. 4.3 meets the test case requirements. The computational domain for this strong shock test case is exactly the same as for the weak shock test case illustrated in FIG. 4.3.

4.3.2 Reference solution

In the strong shock test case, the reference solution evaluation is based on the same methodology as for the first test case. Firstly, one converged mesh is determined. Thereafter, the different numerical schemes as well as their parameters are studied with the aim to build the optimal numerical configuration.

Given that the weak and strong shock test case describes almost the same physics apart the shock strength, the converged mesh can be considered the same. Therefore, based on the mesh convergence analysis performed for the evaluation of the reference solution for the weak shock case, the mesh characteristics can be summarised in TAB. 4.4.

Farfield mesh size [−]	Surface mesh size [−]
1	.002

TABLE 4.4: SU2 converged mesh characteristics of the strong shock test case.

Based on the latter converged mesh, the numerical schemes are studied. For the JST central scheme, the same process is performed concerning the scalar dissipation. In FIG. 4.18, the influence of the fourth order dissipation coefficient on the shock capturing is assessed with the default second order dissipation coefficient. The smaller the coefficient, the more the over- and under-shoots are reduced leading to choose the smallest value. However, the extreme coefficient values illustrated in the figure are the SU2 convergence bounds. Thenceforth, 4^{th} order dissipation coefficient is set at the smallest value allowing solver convergence which is at 0.01.

The process is inverted to study the impact of the second order dissipation coefficient on the solution by fixing the fourth one at the optimal value. It is observed in FIG. 4.19 that the larger the second order coefficient, the smaller the over- and under-shoots. However, another important point to note is from a value around 0.8, the second order dissipation coefficient has no impact on the pressure coefficient distribution anymore. Therefore, it can be concluded that the optimal configuration is reached when the second order dissipation coefficient is equal to 0.8.

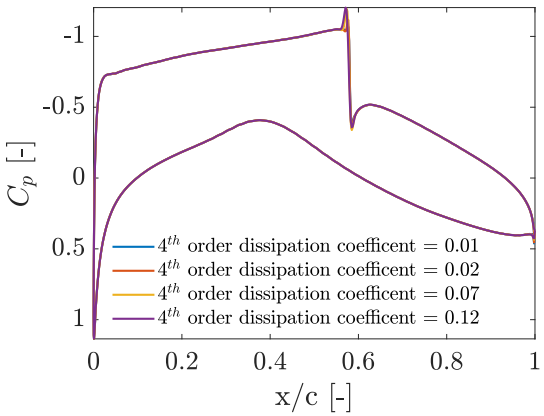

(a) Evolution of the pressure coefficient distribution.

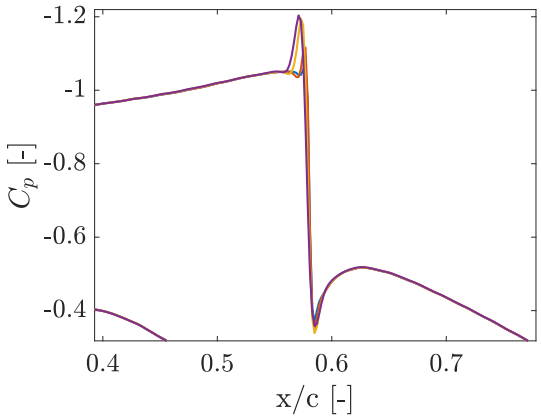

(b) Zoomed in pressure drop zone corresponding to the strong shock.

FIGURE 4.18: Influence study of the 4^{th} order dissipation coefficient in Jameson-Schmidt-Turkel scheme using SU2 based on the converged mesh with the by-default 2^{nd} order dissipation coefficient for the strong shock test case.

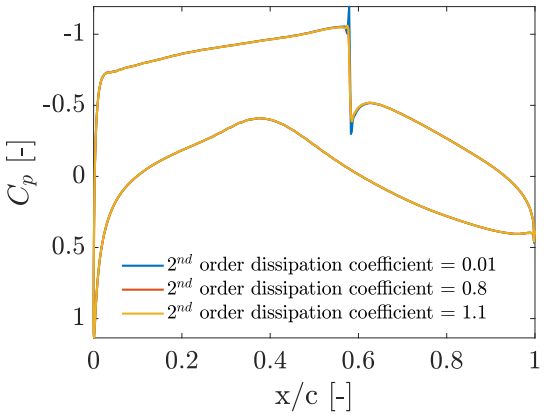

(a) Evolution of the pressure coefficient distribution.

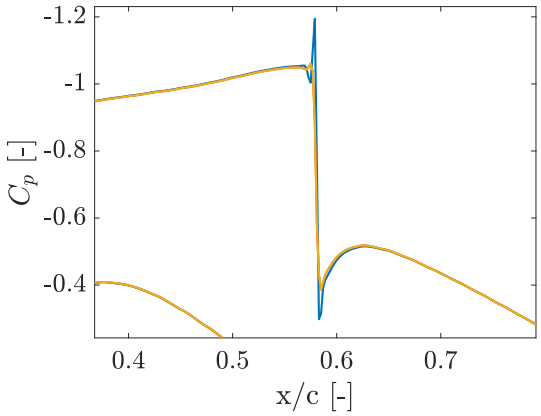

(b) Zoomed in pressure drop zone corresponding to the strong shock.

FIGURE 4.19: Influence study of the 2^{nd} order dissipation coefficient in Jameson-Schmidt-Turkel scheme using SU2 based on the converged mesh with the optimal 4^{th} order dissipation coefficient for the strong shock test case.

Concerning the analysis of the ROE scheme and its numerical parameters, the validity of the limiters applied on the scheme is assumed to be the same illustrated for the weak shock test case in FIG. 4.7. Henceforth, Venkatakrishnan limiters are added to the ROE numerical scheme. Then, the dissipation relaxation coefficient is varied. FIG. 4.20 brings into light that this coefficient has almost no impact on the pressure coefficient distribution. Consequently, the default value is selected to build the optimal ROE numerical configuration.

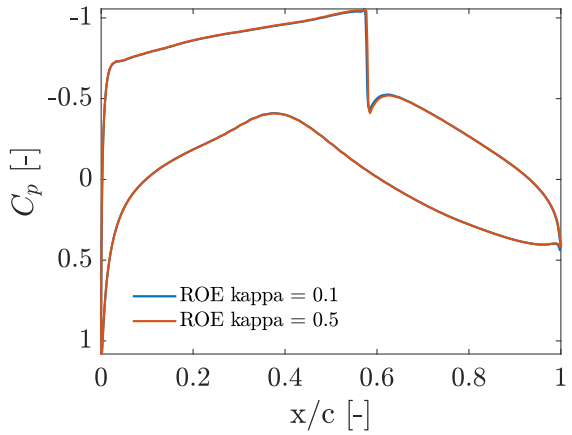

FIGURE 4.20: Influence study of the dissipation relaxation coefficient ROE kappa in ROE scheme using SU2 based on the converged mesh with Venkatakrishnan limiters for the strong shock test case.

Lastly, both optimal numerical configurations are compared based on their pressure coefficient distribution in FIG. 4.21. The latter provide extremely similar results in terms of pressure distribution. Consequently, referring to the selection criterion mentioned in SEC. 4.1.2, both configurations can be identified as an optimal one. Henceforth, for consistency, the optimal numerical configuration for the strong shock test case is the JST central scheme with second and fourth order dissipation coefficients respectively equal to (0.8, 0.01).

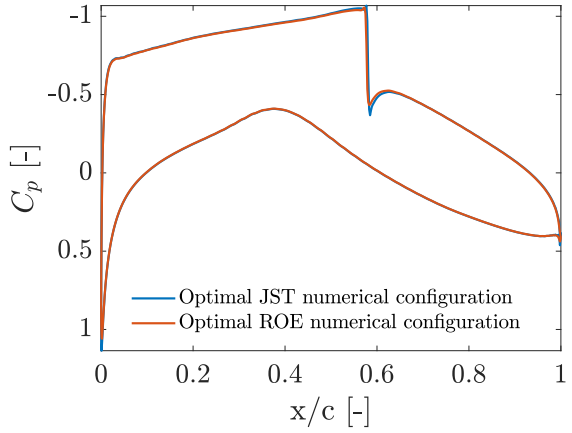

FIGURE 4.21: Comparison between the optimal numerical configuration determined for both JST and ROE scheme in the strong shock test case context using SU2 and the converged mesh.

As a conclusion, the reference solution for the strong shock test case is defined using SU2 based on the *Euler* equations discretised with Jameson-Schmidt-Turkel scheme setting with second and fourth order dissipation coefficients defined at $(0.8, 0.01)$.

Aerodynamic coefficient	Value
C_l [−]	.63
C_d [−]	.0012

(a) Aerodynamic coefficients of the reference solution.

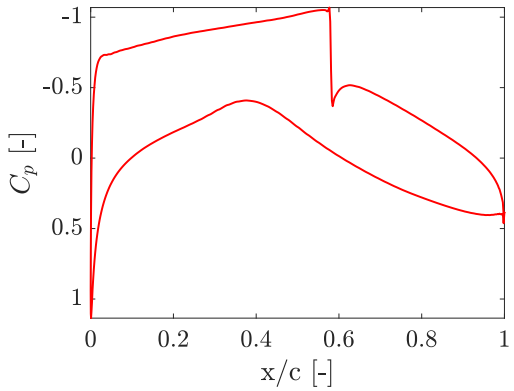

(b) Pressure coefficient distribution of the reference solution.

FIGURE 4.22: Characteristics of the reference solution for the strong shock test case.

4.3.3 Fixed length selection

As explained in the solution description of the fixed length correction, the fixed length has to be determined in relation to the test case.

In this section, the influence of the fixed length L $[m]$ on the aerodynamic coefficients is studied in a strong shock test case. The most suitable value is evaluated with the objective of performing a mesh convergence analysis using the fixed length correction described in SEC. 3.1.

The same analysis methodology as for the weak shock test case is applied. Different mesh size configurations are fixed and then, the fixed length L $[m]$ is varied to determine the most suitable value. FIG. 4.23 represents the evolution of the aerodynamic coefficients with respect to fixed length for different mesh configurations. The first observation is the independence of the aerodynamic coefficients in relation to the fixed length which proves that introducing this additional parameter does not increase the number of variables in the solver. In addition, in the strong shock test case, finding a length range leading to solver convergence becomes much more difficult since it is narrowed compared to the weak shock test case. For example, in FIG. 4.23c and 4.23d, for a farfield mesh size of 1 and a surface mesh size equal to 1/500 of the chord length, the solver converges for one single fixed length value. However, the evolution of the convergent length range with respect to the mesh configurations seems to behave as for the weak shock test case. The fixed lengths also decrease with the surface mesh sizes until reaching a certain threshold for which it converges. Thenceforth, the average of each convergent length range are computed and shown in FIG. 4.24. It can be seen that for sufficiently refined surface mesh sizes, the averaged optimal fixed length converges to the same value. As a conclusion, based on FIG. 4.24, the fixed length L $[m]$ is chosen at 0.008 in the strong shock test case to perform the mesh convergence analysis using the fixed length correction.

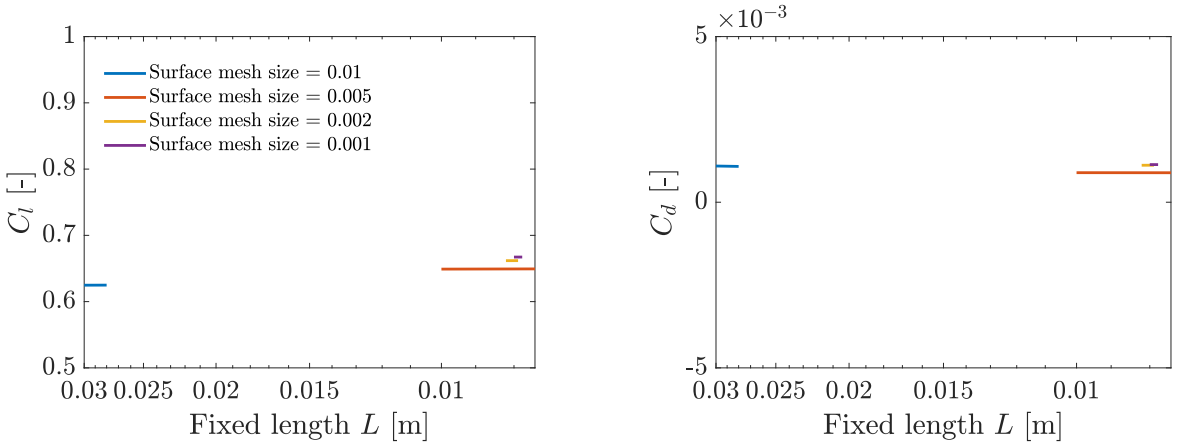

(a) Farfield mesh size = 0.5.

(b) Farfield mesh size = 0.5.

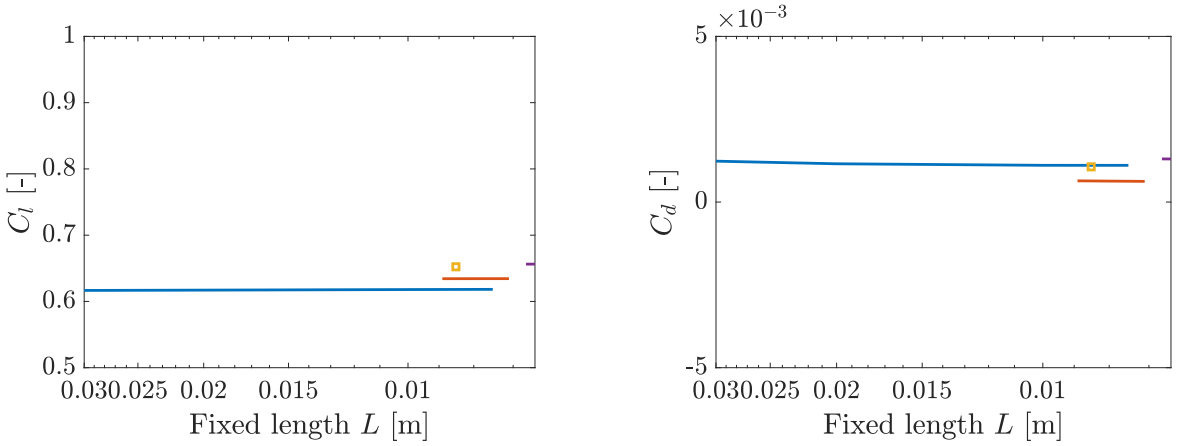

(c) Farfield mesh size = 1.

(d) Farfield mesh size = 1.

FIGURE 4.23: Evolution of the aerodynamic coefficients with respect to the fixed length L for different fixed mesh size configurations in the strong shock test case.

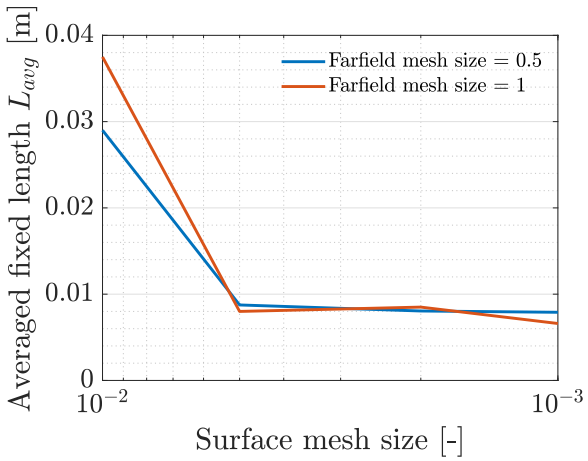

FIGURE 4.24: Evolution of the averaged converging fixed length for the different mesh configurations in the strong shock test case.

4.3.4 Results comparison

In this section, the original and fixed length correction implementations are compared in the context of the strong shock test case. Firstly, the evolution of the lift C_l and the drag C_d coefficients with respect to the mesh density is studied to characterise the mesh-dependency of the original implementation and observe the improvements of the new stabilisation process described in Chap. 3. Secondly, the pressure coefficient C_p distributions with respect to mesh sizes are compared to gain insight on the local behaviour of the flow computed based on the different implementations. The process of analysing the results is conducted in two phases. First, the original implementation is studied in order to characterise the mesh dependency of the global and local results. Then, the results obtained with the fixed length implementation are compared to the original to highlight possible improvements. Note that the observations drawn in the weak test case have been taken into account to drive the mesh convergence analysis.

Lift and drag coefficients

Firstly, the lift coefficient C_l is studied. Fig. 4.25b illustrates the evolution of the lift coefficient with respect to the mesh density for the original DARTFlo and fixed length correction implementation in the strong shock test case. The increase in shock strength makes mesh convergence somewhat more complicated based on the original implementation of DARTFlo. A start of the convergence is initialised from a mesh surface equal to 1/100 of the chord length. However, the results computed with the finest mesh sizes in Fig. 4.25a are not fully converged since the mesh could not be further refined. The observation concerning the farfield mesh size explained in the weak shock test case is also valid for this test case. A farfield mesh size finer or equal to 1 [−] is considered as converged since the curves are almost superimposed in Fig. 4.25. The results obtained with the original DARTFlo implementation can be compared with those computed with SU2. DARTFlo results globally converge to the same lift coefficient range taking into the different levels of fidelity as well as the mesh convergence is not fully completed.

The fixed length correction lift coefficient evolution is depicted in Fig. 4.25b. A slight mesh convergence improvement can be detected for a farfield of 0.5 [−]. On the other hand, the mesh convergence is reduced for the farfield of 1 [−] configuration. This phenomena is entirely due to the difficulty of determining a perfectly suitable fixed length. However, a convergence improvement is achieved for farfield mesh sizes for which the fixed length is optimal. For example, in this test case, the fixed length has been chosen for a farfield mesh size equal to 0.5 [−] which directly induces a convergence improvement. Another point to notice is that introducing a correction in the DARTFlo density upwinding formulation does not affect the results since the curves are similar whatever the implementation.

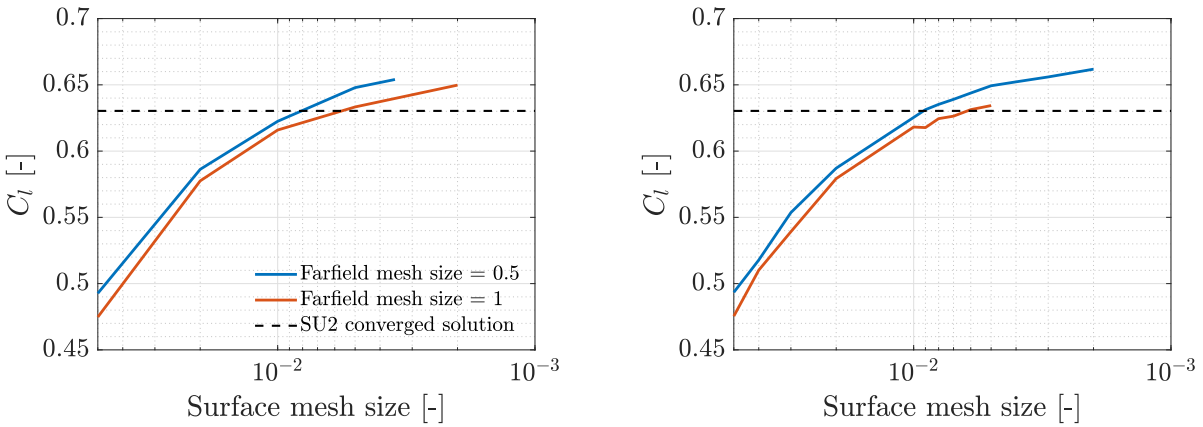

(a) Original DARTFLO implementation 2.4.2. (b) Fixed length correction 3.1 with $L = 0.008$.

FIGURE 4.25: Evolution of the lift coefficient C_l with respect to the mesh density for the original DARTFLO stabilisation solution and fixed length correction in the strong shock test case.

Secondly, the drag coefficient C_d is analysed. FIG. 4.26 shows the evolution of the drag coefficient with respect to the mesh density for the original DARTFLO and the fixed length correction implementations in the strong shock test case. Based on the drag plot, the conclusions concerning the mesh sizes are validated. The results start to converge from a surface mesh size equal to 1/100 of the chord length and a farfield mesh size from 1 is considered as converged. Moreover, the drag coefficient is slightly under-estimated with respect to the higher level of fidelity which is expected due to the difference between the approximations in the aerodynamic model. The convergence improvement is confirmed in FIG. 4.26b for the farfield mesh size of 0.5 since the surface mesh can be further refined.

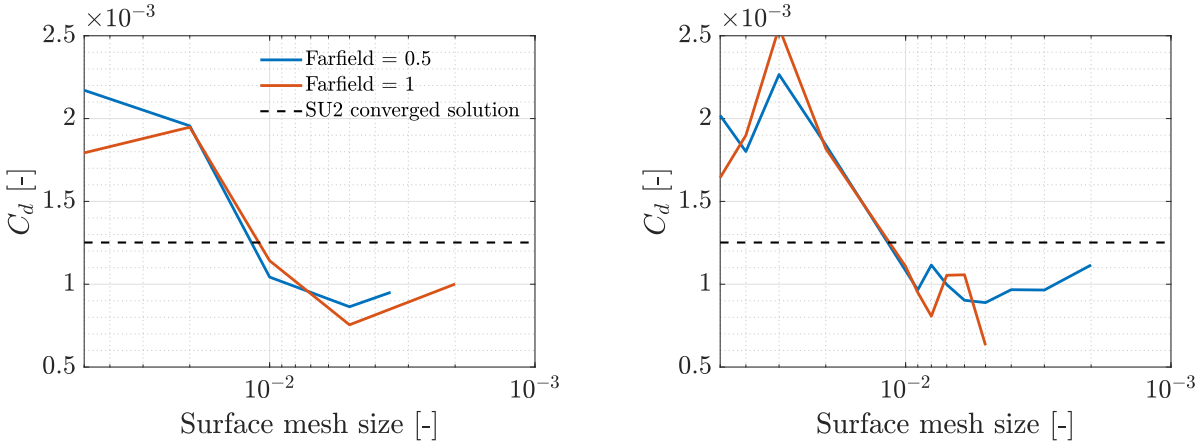

(a) Original DARTFLO implementation 2.4.2. (b) Fixed length correction 3.1 with $L = 0.008$.

FIGURE 4.26: Evolution of the drag coefficient C_d with respect to the mesh density for the original DARTFLO stabilisation solution and fixed length correction in the strong shock test case.

Pressure coefficient distributions

The section aims at analysing the influence of the mesh density on the pressure coefficient distributions in the strong shock test case for the original DARTFlo and fixed length correction implementations.

Fig. 4.27 summarises the case for a fixed farfield mesh size of 0.5. The original DARTFlo implementation provides relatively relevant results since the shock position as well as the pressure distribution converge for surface mesh sizes from 1/200 of the chord length. The curves associated to finer surface mesh are mostly superimposed except in the regions just before and after the shock where under- and over-shoots still evolve with the surface mesh size. These numerical instabilities interrupt the convergence from a certain surface mesh threshold. In addition, short-wavelength oscillations can be detected in the supersonic region, sign of mesh-dependency. However, the shock strength is similar to the reference solution.

In comparison, the evolution of the pressure distribution computed with the fixed length correction implementation is depicted in Fig. 4.27b. Firstly, the shock strength is increased when using this stabilisation solution compared to the original DARTFlo implementation. Therefore, this implementation drives the results in the wrong accuracy direction since the shock strength defined by a higher level of fidelity (SU2) is lower. Secondly, the pressure distribution curve almost converges with respect to the mesh refinement given that the difference between the two finest mesh configurations is small. However, compared to the original DARTFlo implementation, the local flow convergence is degraded since the pressure distribution convergence is not fully complete with the fixed length correction. Lastly, the oscillations occurring in the supersonic regions are attenuated when using the fixed length correction proving improvements concerning mesh-dependency. As a conclusion, the fixed length correction seems to deteriorate the solution computations despite the convergence and mesh-dependency improvements in the strong shock test case. One of the possible reasons is the difficulty to determine an optimal fixed length L $[m]$. Choosing a best-suited fixed length would maybe have enabled to further refine the mesh and illustrate the mesh-independent solutions.

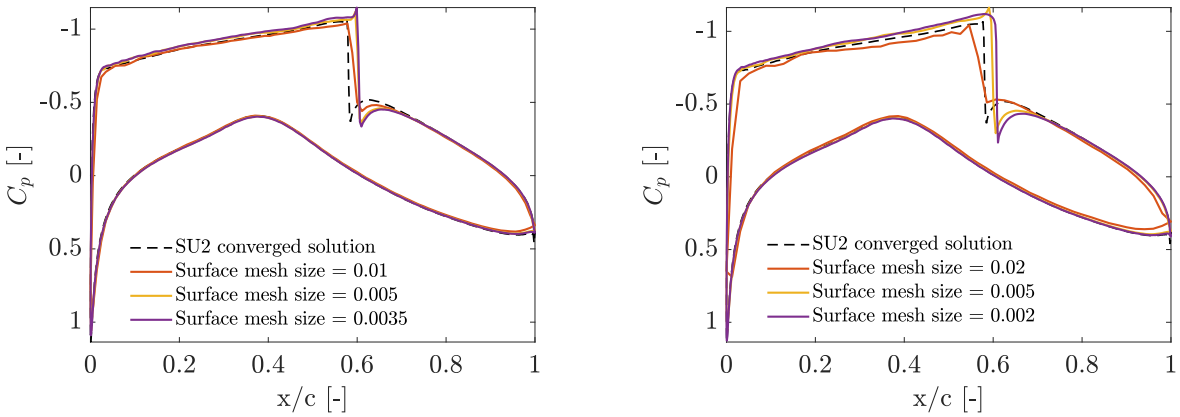

(a) Original DARTFLO implementation 2.4.2. (b) Fixed length correction 3.1 with $L = 0.008$.

FIGURE 4.27: Evolution of the pressure coefficient distribution C_p with respect to the surface mesh size with a **fixed farfield mesh size at 1/2 of the chord length** for the different stabilisation solutions in the strong shock test case.

Henceforth, the farfield mesh size is increased to 1 to evaluate its impact on the pressure distribution using both original DARTFLO and fixed length correction implementations in the strong shock test case. Concerning the original DARTFLO implementation, increasing the farfield mesh prevents the pressure distribution convergence observed for a farfield mesh size of 0.5 illustrated in FIG. 4.27a since except the shock position, the pressure distribution keeps evolving with the surface mesh refinement. In addition, the appearance of large oscillations in the supersonic zone shows that using a farfield mesh size of one or larger starts to become too coarse to enable the perfect stabilisation of the local supersonic flow. However, the shock position approaches the one computed with SU2.

FIG. 4.28b represents the evolution of the pressure coefficient using the fixed length correction. As for the original implementation, strong oscillations are noticed in the supersonic zones which are larger than the ones developed in the original DARTFLO density upwinding case. Although the pressure distribution does not converge during the mesh refinement, the shock position does and tends to the reference one.

Comparing the supersonic zone computed with both implementations, the original DARTFLO implementation illustrates essentially short-length oscillations while the fixed length correction expresses chaotic behaviour of the local flow. These different types of oscillations stem from two different sources. On the one hand, the short-wavelength oscillations are initiated by the mesh-dependency of the density upwinding as already explained in previous analyses. On the other hand, the chaotic behaviour appears due to the farfield mesh size which stands at the limit of the convergence established earlier.

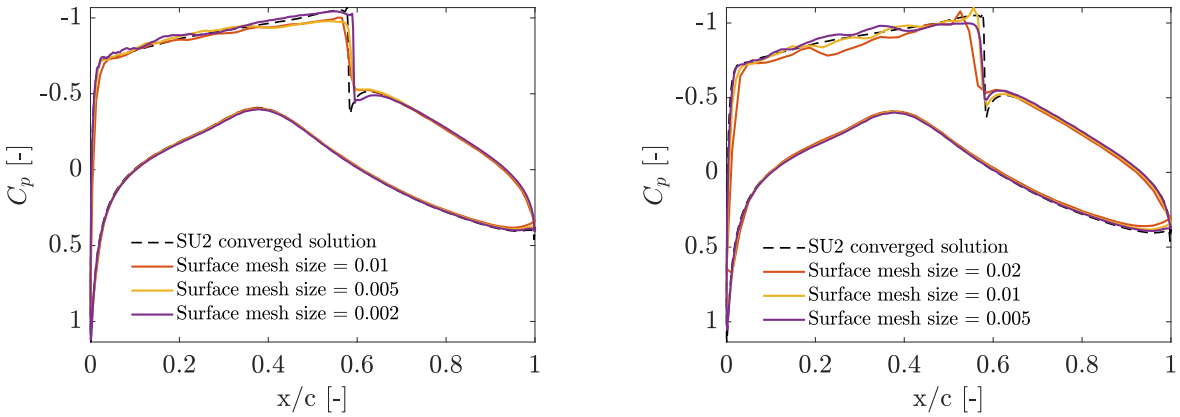

(a) Original DARTFLO implementation 2.4.2. (b) Fixed length correction 3.1 with $L = 0.008$.

FIGURE 4.28: Evolution of the pressure coefficient distribution C_p with respect to the surface mesh size with a **fixed farfield mesh size at 1 of the chord length** for the different stabilisation solutions in the strong shock test case.

4.3.5 Discussion

In this section, mesh convergence analyses performed using both original DARTFLO and the fixed length correction implementations are discussed in the context of the strong shock test case.

The original DARTFLO implementation exhibited relatively accurate results. For sufficiently refined mesh configurations, the pressure distribution converges to reach mesh-independent solutions *i.e.* which do not vary with the mesh anymore in the strong shock test case. In addition, the shock characteristics are similar to SU2 reference solution despite the different levels of fidelity. Another important point to note is that a farfield mesh size coarser than 1 leads to the appearance of oscillations in the supersonic zones of the flow illustrating the start of the scheme instability.

As to the fixed length correction, the results seem to be degraded compared to original density upwinding. Despite the convergence improvements obtained with an optimal fixed length for certain mesh configurations and the short-wavelength oscillations stabilisation, the pressure distribution graphs reveal that the solutions tend to the wrong accuracy direction when the mesh-dependency is withdrawn. For a farfield equal to 0.5, the shock strength is increased while it should at least stay unchanged or slightly decrease and the shock position is a bit more delayed downstream. However, when the farfield mesh size is coarsened, despite strong oscillations in the supersonic region, the shock position converges towards SU2 location. This high variability of the solution is undoubtedly due to the difficulty of determining an optimal fixed length in the strong shock test case. Therefore, further analyses should be performed to draw a selection rule for the fixed length in this type of cases.

4.4 Three-dimensional test case

In this section, the stabilisation solutions are analysed in a three-dimensional test case. Firstly, the three-dimensional test case is described. Then, the different stabilisation solutions are compared based on the different parameters detailed earlier. Lastly, the results are discussed.

4.4.1 Case description

The goal of the three-dimensional test case is to compare the different stabilisation solutions on a commercial wing. The type of aircraft chosen as being a commercial reference is the regional family which usually have a lift coefficient C_L around $0.4 - 0.45$ $[-]$. Therefore, a three-dimensional wing is designed based on common geometrical properties of commercial regional aircraft to reach this lift coefficient target. The airfoil is the same as for the two-dimensional cases, the RAE2822. The wing geometry is summarised in Tab. 4.5 and depicted in Fig. 4.29. In addition, for the local flow analysis, different wingspan stations are defined; the wing root, the mean aerodynamic chord ($\approx$ 42%-span), 60%-span location and the wingtip.

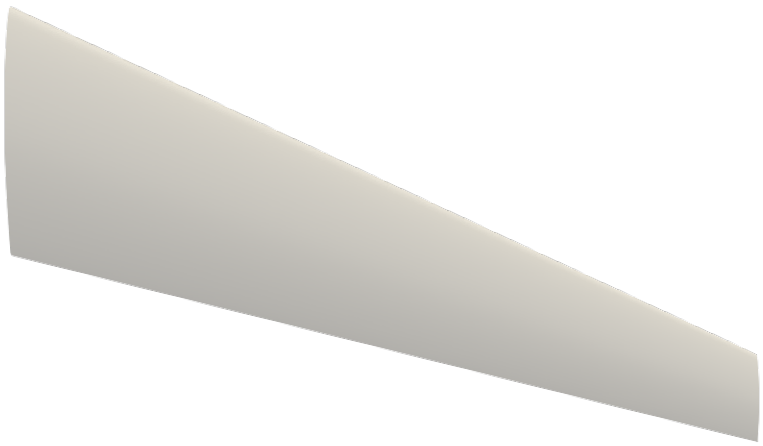

Figure 4.29: Top view of the three-dimensional wing designed to test the different stabilisation solutions based on common regional aircraft.

Parameter	
Span $[m]$	15.
Root chord $[m]$	5.
Taper ratio $[-]$	.35
Sweep angle $[°]$	25.
Twist angle $[°]$	-2.
Dihedral $[°]$	0.

Table 4.5: Wing geometrical parameters for the three-dimensional test case.

Airfoil	Mach number M [−]	Angle of attack α [°]	Dimensions
RAE2822	.794	1.5	3D

TABLE 4.6: Flow characteristics of the three-dimensional test case.

As illustrated in appendices SEC. B.3, the wing design achieves performance within the lift coefficient target range for the regional aircraft class.

The computational domain is a rectangular box in three-dimensions. As for the two dimensional cases, the symmetry plane and its parallel are scaled with respect to the wing root chord length. The upstream and downstream surfaces are located at a distance of five times the wing root chord length regarding respectively the leading and trailing edge of the wing root airfoil as illustrated in FIG. 4.30 (left). The distance between the symmetry and its parallel plane is set at two times the wing span as can be observed in FIG. 4.30 (right). As for the top and bottom surfaces, they are placed at five times the wing root chord length away from the wing root airfoil.

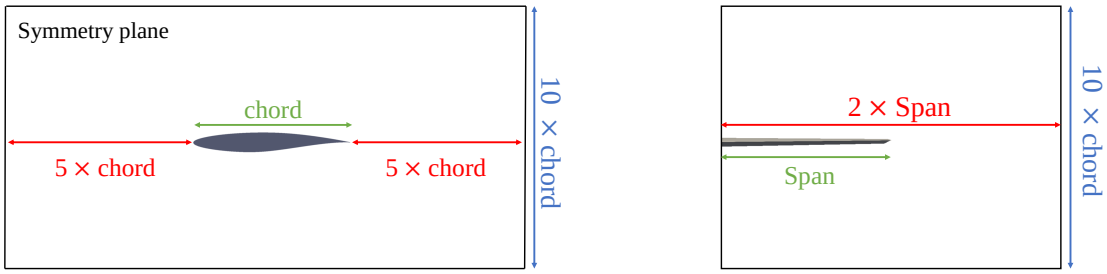

FIGURE 4.30: Symmetry plane (left) and bottom (right) views of the three-dimensional computational domain.

4.4.2 Reference solution

In the three-dimensional test case, the reference solution is determined based on the same methodology as detailed in SEC. 4.1.2. Firstly, converged meshes are evaluated through a mesh convergence analysis using by-default the JST central scheme with default scalar dissipation. Then, different numerical schemes are tested and compared to assess the best reference configuration.

FIG. 4.31 illustrates the evolution of the aerodynamic loads with respect to the wing surface mesh size for different farfield mesh sizes. Note that the mesh sizes have been non-dimensionalised by their associated airfoil chord lengths defining the different wing planforms summarised in TAB. 4.5. Based on the mesh convergence analysis, a change in the lift coefficient curve slope is observed for surface mesh sizes from 1/100 of the chord lengths corresponding to the start of the convergence. Whereas from the drag evolution graph, a convergence is observed from surface mesh sizes around 1/20 of chord lengths.

Concerning the farfield mesh, the observations from previous test cases are verified since from farfield mesh size equal to 1 [−], the lift evolution curves are similar and almost superimposed.

As a conclusion, for the three-dimensional test case in SU2, the converged mesh characteristics are summarised in Tab. 4.7.

Farfield mesh size [−]	Surface mesh size [−]
1	.01

Table 4.7: SU2 converged mesh characteristics of the three-dimensional test case.

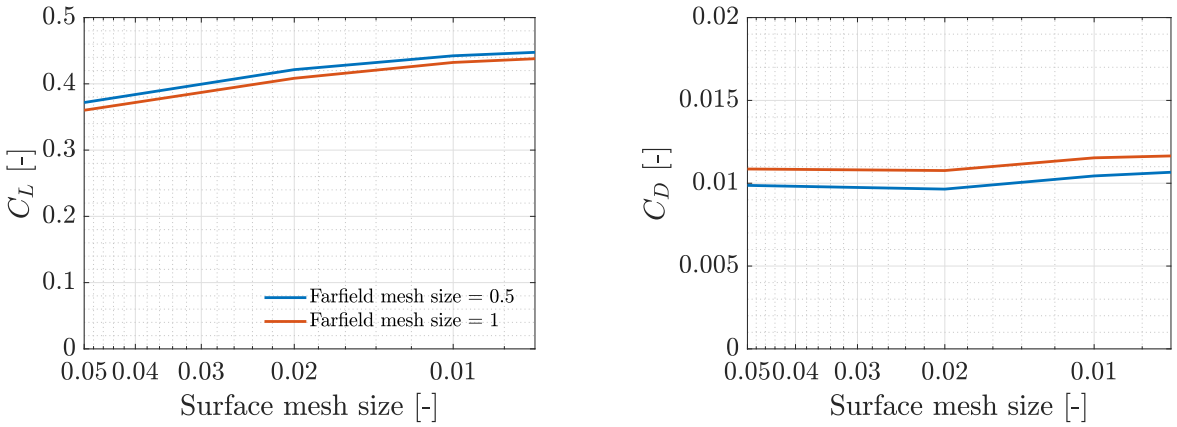

(a) Three-dimensional lift coefficient C_L [−] mesh convergence analysis.

(b) Three-dimensional drag coefficient C_D [−] mesh convergence analysis.

Figure 4.31: Mesh convergence analysis on the aerodynamic coefficients performed with SU2 using the Jameson-Schmidt-Turkel convective scheme with by-default dissipation coefficients [57].

Based on the converged mesh configuration, the different numerical schemes described in Sec. 4.1.2 are compared to determine the best SU2 reference solution. Firstly, the Jameson-Schmidt Turkel scheme is studied by varying the different scalar dissipation coefficients. To begin, the second order dissipation coefficient is fixed at its default value to enable the evaluation of the fourth order impact. Once the fourth order dissipation coefficient value has been determined following the selection criterion described in Sec. 4.1.2, the influence of the second order one is characterised to result with the best numerical configuration based on JST scheme.

Fig. 4.32 illustrates the evolution of the pressure distribution at the wing root ($y = 0$) with respect to the 4^{th} order dissipation coefficient available in the JST central scheme for a by-default fixed second order dissipation coefficient. The wing root has been chosen for the analysis since this wing location provides the strongest shock and thus, the most sensitivity to numerical parameters. Therefore, if the numerical configuration provides good solutions at this location, it is automatically the case at the rest of the wing. The

same 4^{th} order dissipation coefficient analysis has been performed at another wingspan station to prove the latter assumption in appendices Sec C.1.

The first observation that can be drawn is that the smaller 4^{th} order dissipation coefficient, the steeper the shock is while keeping a reasonable over-shoot. However, from a value around 0.01, the pressure distribution converges since it does not vary anymore with the dissipation coefficient. Therefore, a 4^{th} order dissipation coefficient equal to 0.01 is the optimal numerical choice for the JST model in the three-dimensional case.

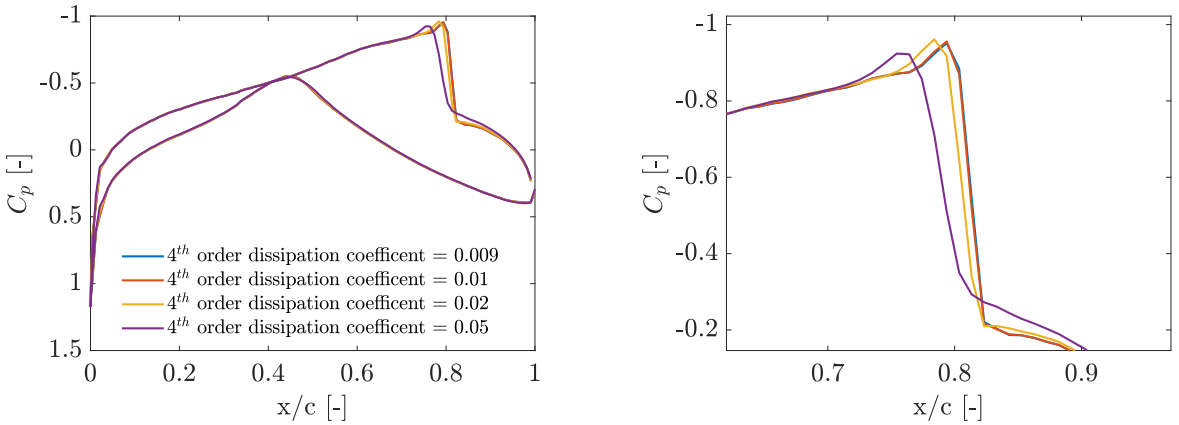

(a) Evolution of the pressure coefficient distribution at the wing root $y = 0$.

(b) Zoomed in pressure drop zone corresponding to the shock at the wing root $y = 0$.

Figure 4.32: Influence study of the 4^{th} order dissipation coefficient in Jameson-Schmidt-Turkel scheme using SU2 based on the converged mesh with the by-default 2^{nd} order dissipation coefficient for the three-dimensional test case.

Using the optimal 4^{th} order dissipation coefficient, the impact of the 2^{nd} order coefficient is evaluated. Fig. 4.33 illustrates that the larger the coefficient, the smaller the over-shoot while keeping a steep shock. From a certain threshold, the pressure distribution converges in a steep shock almost without over- and under-shoots. Therefore, the optimal value for the 2^{nd} order dissipation coefficient is 0.8.

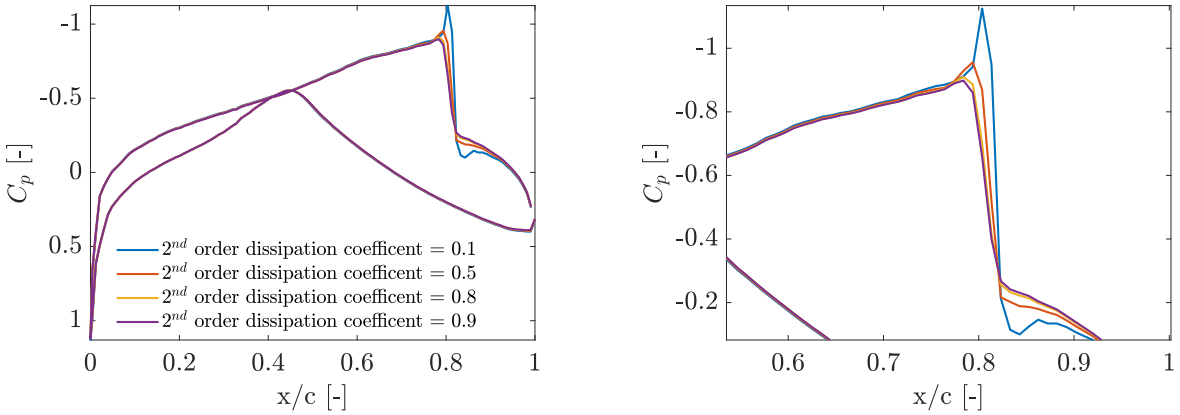

(a) Evolution of the pressure coefficient distribution at the wing root $y = 0$.

(b) Zoomed in pressure drop zone corresponding to the shock at the wing root $y = 0$.

FIGURE 4.33: Influence study of the 2^{nd} order dissipation coefficient in Jameson-Schmidt-Turkel scheme using SU2 based on the converged mesh with the optimal 4^{th} order dissipation coefficient for the three-dimensional test case.

The second numerical scheme studied in the scope of the reference solution computations is the ROE upwind scheme in which a dissipation relaxation coefficient can be played with. No reference solution for the three-dimensional test case could be computed whatever the coefficient value since the solver never converges. Therefore, the optimal numerical configuration to compute the SU2 reference solution for the three-dimensional test case is derived based on the JST central scheme with the second and fourth order dissipation coefficients set to $(0.8, 0.01)$. As a conclusion, the reference solution aerodynamic coefficients are summarised in TAB. 4.8.

Aerodynamic coefficient	**Value**
C_L $[-]$	.43
C_D $[-]$	.013

TABLE 4.8: Aerodynamic coefficients of the reference solution.

4.4.3 Fixed length selection

As explained in the solution description of the fixed length correction, the fixed length has to be determined in relation to the test case.

The fixed length L $[m]$ used to correct the original DARTFLO density upwinding has to be determined with the objective of subsequently performing a mesh convergence analysis.

The selection is conducted as follows, several fixed mesh configurations are constructed and then, the fixed length is varied to observe its influence on the aerodynamic coefficients. FIG. 4.34 depicts the evolution of the aerodynamic coefficients with respect to the fixed length L for different mesh configurations. Firstly, the independence of the parameters with respect to the fixed length is still observed in the three-dimensional test case *i.e.* parameters do not vary with L. In addition, it can be deduced that from a certain mesh threshold, the convergent length ranges almost converge. Indeed, from surface mesh sizes equal to 1/50 of the chord lengths, the fixed lengths allowing the solver convergence tend to the same range of validity. However, in a three-dimensional case, defining the optimal fixed length is much more difficult since the surface mesh size varies within a large range of values along the span.

The averages of the different convergent fixed length ranges are calculated to demonstrate which would be the most optimal value for the three-dimensional case. FIG. 4.35 illustrates that from surface meshes finer than 0.02 $[-]$, the means converge to relatively different values depending on the farfield mesh size. In addition, since the results are illustrated for adimensionalised surface mesh sizes, the choice of the fixed length is biased. In reality, the element size at the wing root and wingtip is different inducing that an optimal fixed length for the wing root is not necessarily optimal for wingtip element size. Therefore, choosing an optimal fixed length for the entire wing would deserve deeper analyses about the selection process. However, based on FIG. 4.35, a fixed length is determined. In order to perform the mesh convergence analysis in the next section, the fixed length L $[m]$ is chosen at 0.1.

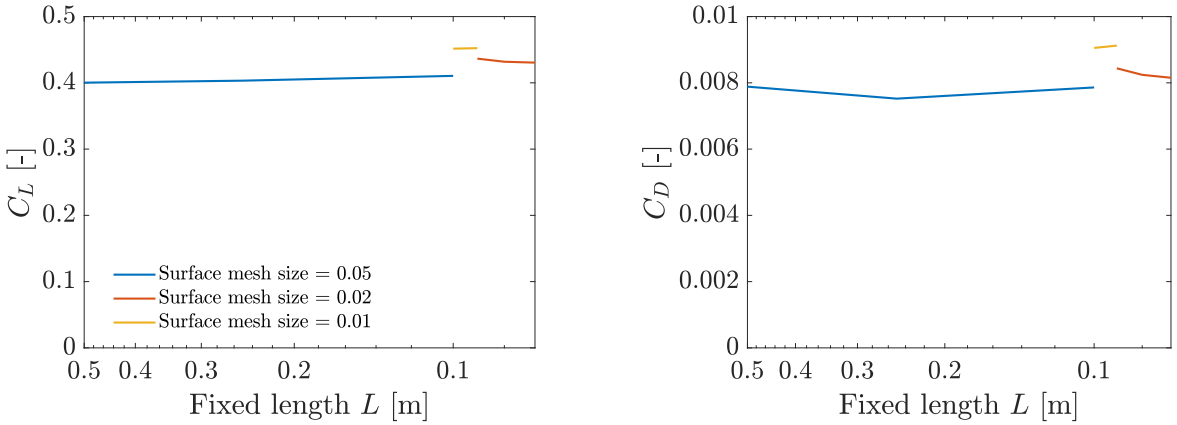

(a) Farfield mesh size = 0.5.

(b) Farfield mesh size = 0.5.

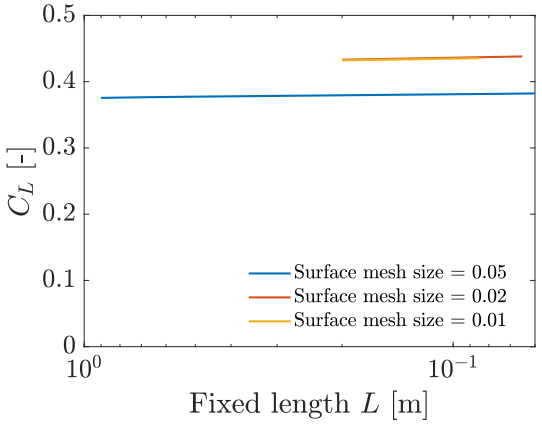

(c) Farfield mesh size = 1.

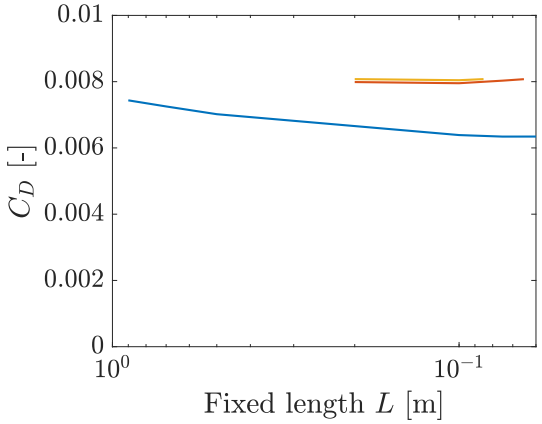

(d) Farfield mesh size = 1.

FIGURE 4.34: Evolution of the aerodynamic coefficients with respect to the fixed length L for different fixed mesh size configurations in the three dimensional test case.

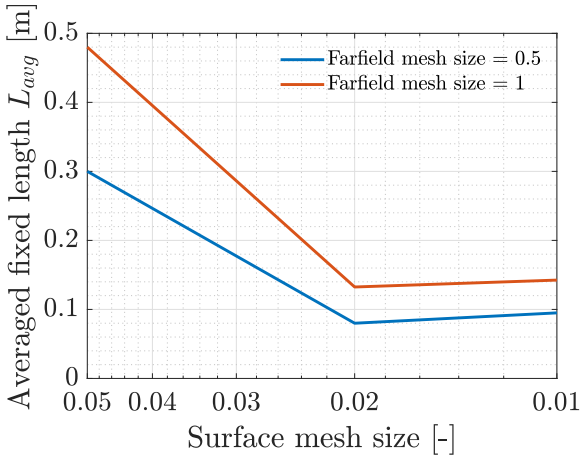

FIGURE 4.35: Evolution of the averaged converging fixed length for the different mesh configurations in the three dimensional test case.

4.4.4 Results comparison

In this section, the original and fixed length correction are compared in the context of the three dimensional test case. Firstly, the evolution of the lift C_L and the drag C_D coefficients with respect to the mesh density is studied to characterise the mesh-dependency of the original implementation and observe the improvements of the new stabilisation processes described in CHAP. 3. Secondly, the pressure coefficient C_p distribution with respect to mesh sizes are compared to gain insight on the local behaviour of the flow computed based on the different implementations.

The process of analysing the results is conducted in two phases. First, the original implementation is studied in order to characterise the mesh dependency of the global and local results. Then, the results obtained with the new implementation are compared to the original to highlight possible improvements. Note that the observations drawn in the weak shock and strong shock test cases are taken into account to drive the mesh convergence analysis.

Lift and drag coefficients

In the first instance, the lift coefficient C_L is analysed. FIG. 4.36 illustrates its evolution with respect to the mesh density for both the original DARTFLO density upwinding and the fixed length correction in the three dimensional test case. Based on original DARTFLO results, a change in the lift curve slope can be observed from surface mesh sizes equal to 1/50 of the chord lengths in FIG. 4.36a. Depending on the farfield mesh size, the results are either over-estimated with respect to SU2 reference solution or similar illustrating a relative mesh-dependency. For example, the finest mesh configuration induces a relative error around 6% in relation to the reference solution.

Concerning the fixed length correction, FIG. 4.36b highlights a slight reduction in convergence compared to the original density upwinding due to the difficulty of finding an optimal fixed length for the entire wing. However, the lift coefficient curves are getting closer to the SU2 reference solution. For example, the finest mesh configuration results in a relative error equal to 5%. In addition, the mesh-dependency is partially removed since the curves are almost superimposed compared to the original DARTFLO implementation for which the lift coefficient evolution curves are distinct.

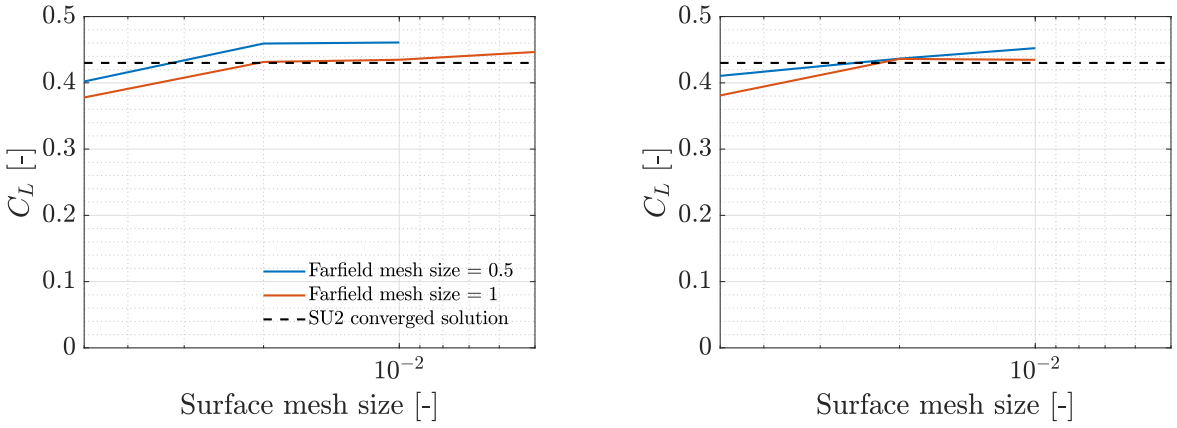

(a) Original DARTFLO implementation 2.4.2. (b) Fixed length correction 3.1 with $L = 0.1$.

FIGURE 4.36: Evolution of the lift coefficient C_L with respect to the mesh density for the original DARTFLO stabilisation solution and fixed length correction in the the three-dimensional test case.

Secondly, the drag coefficient C_D is studied. Its evolution with respect to the mesh density for the two stabilisation solutions retained after both two-dimensional test cases is plotted in FIG. 4.37. The observations concerning the mesh convergence are verified based on the drag evolution curves. The start of the convergence is detected from surface sizes around 1/50 of the chord lengths. The influence of the farfield mesh size on drag coefficient evolution is noticeable illustrating mesh-dependency phenomena. However, the fixed length correction provides a slight improvement since the curves for the different farfield mesh sizes get closer compared to the original DARTFLO implementation. In addition, the drag coefficient for both implementations is under-estimated which is expected due the difference of levels of fidelity.

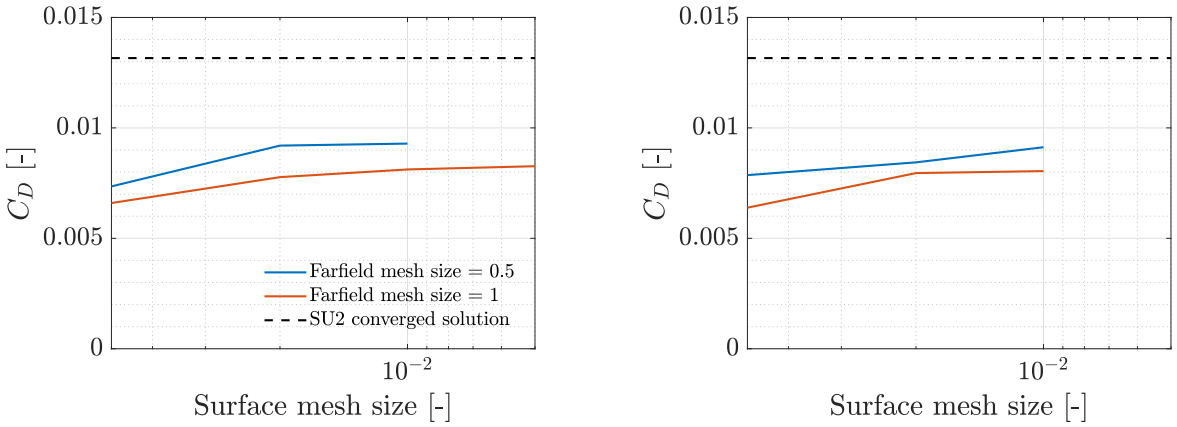

(a) Original DARTFLO implementation 2.4.2. (b) Fixed length correction 3.1 with $L = 0.1$.

FIGURE 4.37: Evolution of the drag coefficient C_D with respect to the mesh density for the original DARTFLO stabilisation solution and fixed length correction in the the three-dimensional test case.

Pressure coefficient distributions

This section aims to gain insight into the local behaviour of the flow at different positions along the span with the pressure coefficient distributions are studied.

Firstly, the local flow at the wing root is analysed in Fig. 4.38 describing the strongest shock experienced on the wing. The original DARTFlo implementation with a farfield mesh size equal to 0.5 presents a shock position which has more of less converged with the surface mesh refinement. This position sticks with the reference solution which proves that similar results can be obtained with different aerodynamic levels of fidelity. However, the pressure distribution does not converge with respect to the surface mesh for a farfield of 0.5 as observed in Fig. 4.38a. Indeed, the pressure curve for a surface mesh size equal to 1/50 of the chord lengths is almost fully superimposed with the SU2 solution while for a doubly refined surface mesh, the pressure distribution keeps varying since a stronger over- and under-shoot appears. It clearly illustrates the results mesh-dependency experienced by the full potential solver.

Coarsening the farfield mesh size depicted in Fig. 4.38c enables the pressure distribution to more or less converge. When the surface mesh size is refined finer than 1/100 of the chord lengths, the curves overlap and therefore almost merge. The pressure drop characterising the shock becomes steeper than SU2 which gets closer to the definition of a shock *i.e.* a discontinuity in the flow. In addition, the appearance of short-wavelength oscillations is noticed in the supersonic regions of the suction and pressure sides for a refined surface mesh to 1/200 of the chord lengths. These oscillations show that extremely refining the surface mesh makes the numerical scheme unstable. Consequently, it can be deduced that the stabilisation process loses some of its effectiveness when the mesh is refined, illustrating the mesh-dependency. As already explained earlier, since DARTFlo density upwinding depends on the mesh, the artificial viscosity effect is attenuated when the mesh in the supersonic zones is highly refined leading the solver to become less and less stable in these sensitive areas.

Fig. 4.38b and 4.38d demonstrate the evolution of the pressure distribution at the wing root based on the fixed length correction implementation with respect to the mesh density. Firstly, refining the surface mesh enables to almost converge the pressure distribution since the difference between the two finest mesh configuration moves the shock position by 1% which is negligible. Therefore, from a certain threshold, mesh refinement has only a minimal impact on the results. In addition, this approximate mesh convergence enables the results to get closer to the higher level of fidelity. However, compared the original DARTFlo implementation, the over- and under-shoots are larger involving an increase in the shock strength.

Then, the farfield mesh size is coarsened to 1 and the impact is studied. A priori, the results convergence is cancelled for the fixed length correction since the pressure distribution

does not tend to a single curve. The difficulty to determine an optimal fixed length for the correction is an important limiting factor when the mesh is extremely refined. In addition, another limiting factor of the three-dimensional analysis is the computational power since large numbers of elements are directly induced when the surface mesh is refined. Indeed, the mesh convergence analysis as well as the fixed length selection require repetitive simulations. For example, if the surface mesh size could have been refined further than 1/100 of the chord lengths based on the fixed length correction, the results mesh-independency could have been confirmed as the purple curve corresponding to the finest surface mesh size in FIG. 4.38d converges towards SU2 reference pressure distribution. However, the oscillations experienced by the original density upwinding implementation described previously are attenuated in the supersonic regions illustrating the slight improvement brought by the fixed length correction for the mesh-dependency.

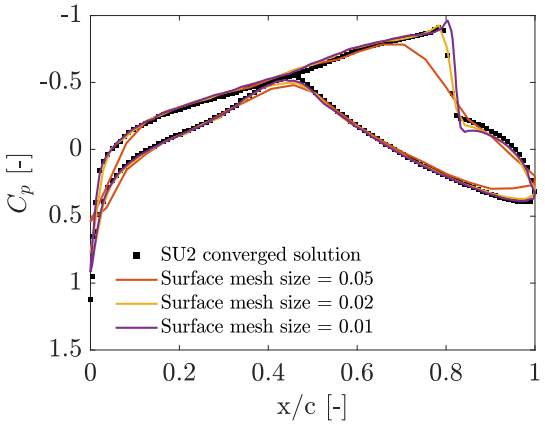

(a) Original DARTFLO implementation with a farfield mesh size = 0.5.

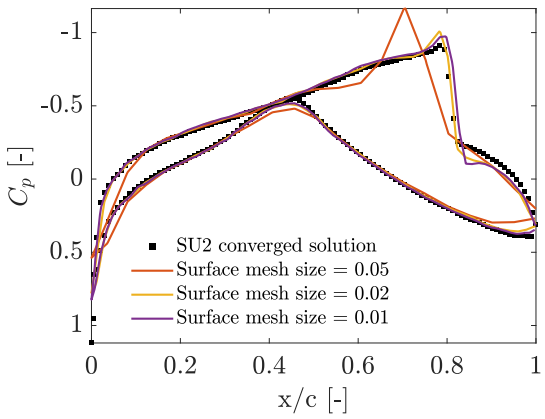

(b) Fixed length correction implementation with a farfield mesh size = 0.5 and $L = 0.1$.

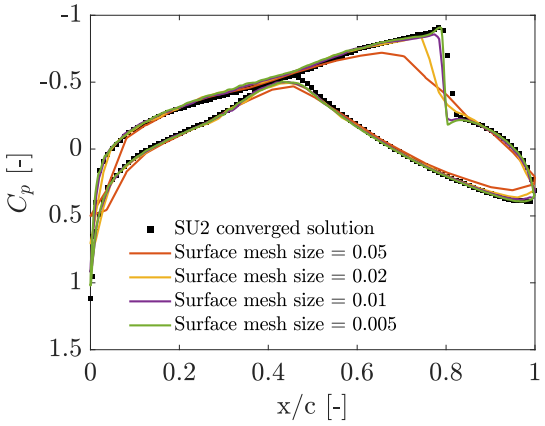

(c) Original DARTFLO implementation with a farfield mesh size = 1.

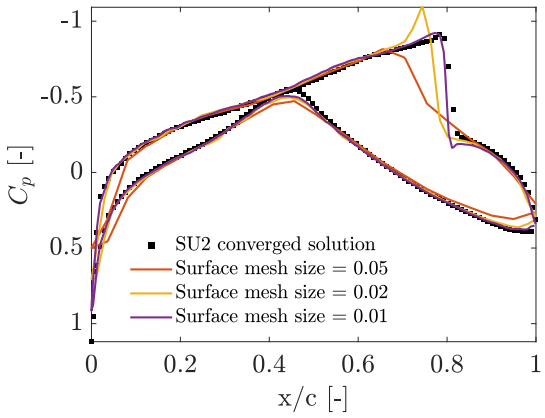

(d) Fixed length correction implementation with a farfield mesh size = 1 and $L = 0.1$.

FIGURE 4.38: Evolution of the pressure coefficient C_p distribution with respect to the mesh density for both original DARTFLO and fixed length correction implementations at the wing root ($y = 0\ m$) in the three dimensional test case context.

Afterwards, the same analysis is performed at the mean aerodynamic chord in FIG. 4.39.

At this spanwise station, the angle of attack becomes ≈ 0.66 degrees due to the twist angle inducing a weaker shock slightly moved upstream. Concerning the original DARTFlo implementation, the same conclusions as the root station can be drawn. The shock position converges with the mesh refinement while the pressure distribution keeps evolving illustrating the mesh-dependency of the stabilisation density upwinding. In addition, for highly refined surface meshes, the oscillations appearing on the suction and pressure sides demonstrate that the more the mesh is refined, the less the stabilisation effect of the density upwinding acts on the supersonic regions.

Increasing the farfield mesh size leads to a slight improvement in the results convergence since the difference observed between the two finest mesh configurations illustrated in Fig. 4.39c is minimal. However, the oscillations become heavier further destabilising the numerical scheme. This can be explained by the presence of a too large mesh growth factor leading to a fast mesh evolution between the body surfaces and the domain boundaries. Therefore, the mesh in the shock zone becomes quickly too coarse to correctly capture all the physics.

Concerning the fixed length correction, the mesh convergence is globally better than the original implementation since from a certain surface mesh size, the change in the pressure distribution and the shock position is of the order of 2%. However, stronger over- and under-shoots are experienced over-estimating the shock strength with respect to SU2. In addition, compared to the previous wingspan station, it can be observed in Fig. 4.39d that small oscillations are present on both suction and pressure sides with the fixed length correction. This is in contradiction with the results at the wing root for which these short oscillations were attenuated compared to the original density upwinding implementation.

If the farfield mesh size is coarsened to 1, the mesh convergence disappears since the pressure curves keep varying with respect to the mesh density. In addition, the oscillations observed for a finer mesh, get heavier in Fig. 4.39d. Therefore, at this farfield mesh size and wingspan station, the solution seems to be deteriorated with respect to the original density upwinding.

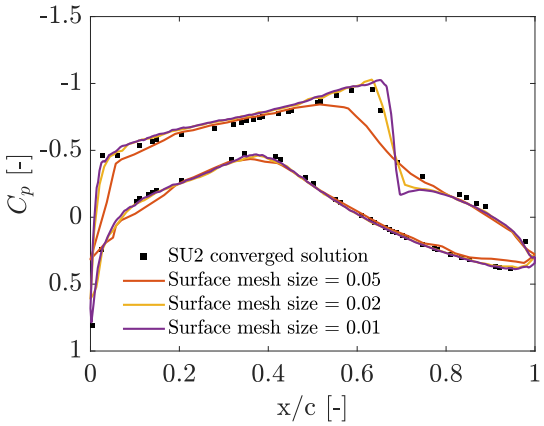

(a) Original DARTFLO implementation with a farfield mesh size = 0.5.

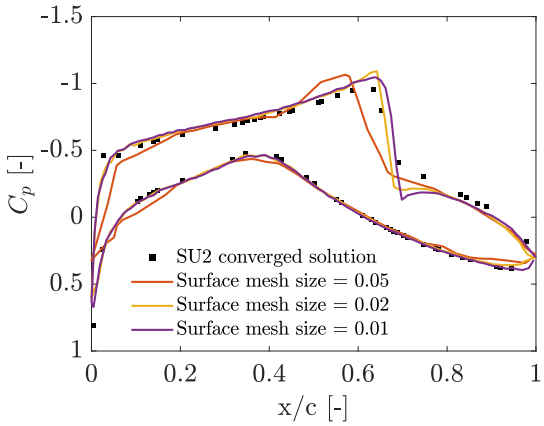

(b) Fixed length correction implementation with a farfield mesh size = 0.5 and $L = 0.1$.

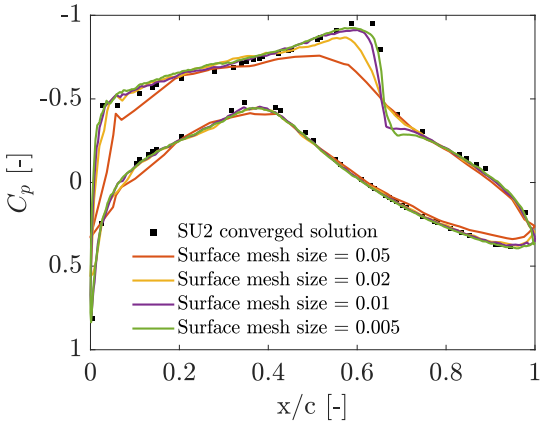

(c) Original DARTFLO implementation with a farfield mesh size = 1.

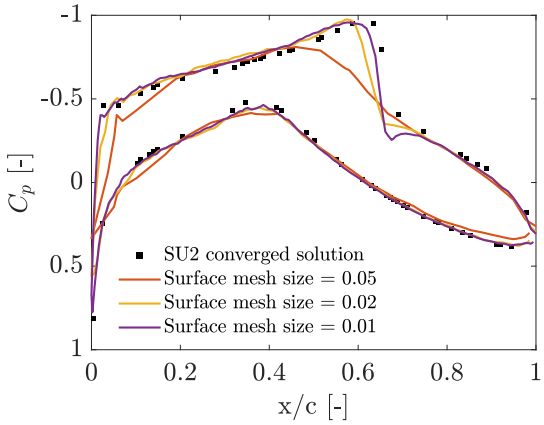

(d) Fixed length correction implementation with a farfield mesh size = 1 and $L = 0.1$.

FIGURE 4.39: Evolution of the pressure coefficient C_p distribution with respect to the mesh density for both original DARTFLO and fixed length correction implementations at the mean aerodynamic chord ($y \approx 6.3\ m$) in the three dimensional test case context.

As the study position moves away from the wing root, the angle of attack decreases and thus, the shock strength is reduced and the shock position keeps moving upstream. At 60% of the wingspan ($y = 9\ m$), the angle of attack becomes 0.3 degrees. FIG. 4.40 depicts the evolution of the pressure distribution at this wing station with respect to the mesh density. As observed for the original DARTFLO implementation, the shock capturing converges since from a surface mesh size equivalent to 1/50 of the chord lengths, the pressure distribution at the shock position does not vary anymore with the mesh. However, the mesh-dependency is still illustrated by the short-wavelength oscillations occurring in the supersonic zone. Henceforth, the farfield mesh size is increased to 1 reinforcing the oscillations on the suction side due to a larger mesh growth rate. However, the local flow at the shock still converges with respect to the surface mesh since both curves are superimposed.

Concerning the fixed length correction results illustrated in FIG. 4.40b and 4.40d, the conclusions are different depending the farfield mesh size. For a farfield mesh size equal

to 0.5, the correction does not greatly improve the local flow since as for the original implementation, oscillations occur on the supersonic suction side of the airfoil even if they are attenuated with the fixed length correction. In addition, the pressure curves at the shock position are still moderately modified with refined mesh sizes while with DARTFLO density upwinding, the pressure distribution converges. In other words, in this case, the results seem to be improved on some aspects and degenerated on others by the correction. However, when the farfield is coarsened, the fixed length correction limits the degradation of the results by containing the development of stronger oscillations and by keeping a certain convergence of the results with respect to the mesh.

More globally, comparing both implementations with respect to the reference solution, the results obtained based on the fixed length correction are closer to SU2 reference which represents a higher aerodynamic level of fidelity. This illustrates that based on the correction, the results are not degraded and even are slightly more accurate.

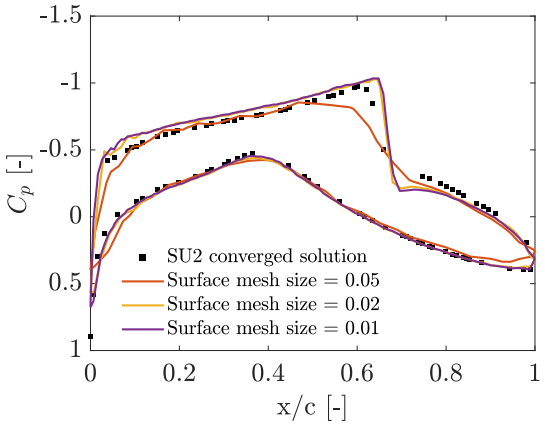

(a) Original DARTFLO implementation with a farfield mesh size = 0.5.

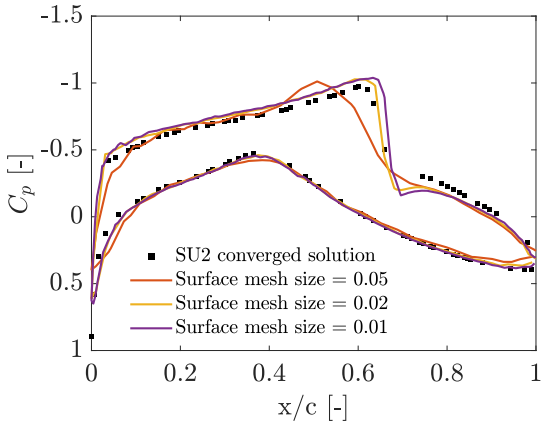

(b) Fixed length correction implementation with a farfield mesh size = 0.5 and $L = 0.1$.

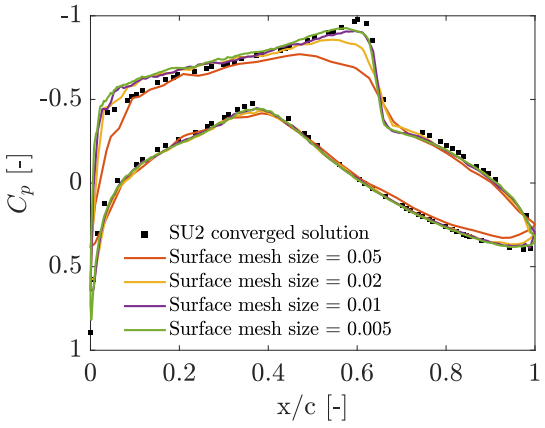

(c) Original DARTFLO implementation with a farfield mesh size = 1.

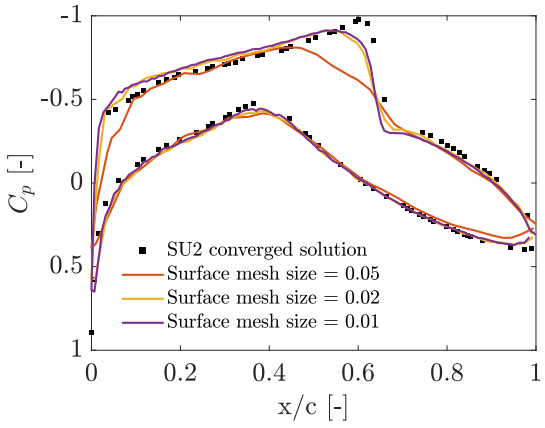

(d) Fixed length correction implementation with a farfield mesh size = 1 and $L = 0.1$.

FIGURE 4.40: Evolution of the pressure coefficient C_p distribution with respect to the mesh density for both original DARTFLO and fixed length correction implementations at 60% of the wingspan ($y = 9\ m$) in the three dimensional test case context.

The last station to be studied is the wingtip. Since a tip vortex singularity inducing an infinite local velocity is experienced by three-dimensional configurations in DARTFLO [27], studying the local flow at 95% of the wingspan is preferable. The flow variation between the wingtip and the 95%−wingspan station is considered to be minimal. At this wing location, the angle of attack is negative. No more shock is triggered in the flow. It can be observed that whatever the mesh configuration or the stabilisation implementation, the local flow undergoes strong oscillations. The main reason is the development of wingtip vortices which have an impact on the near-flow and require finer surface meshes than those used in this case to properly capture the local flow. Therefore, observing the improvements of the fixed length correction is difficult at this wingspan station.

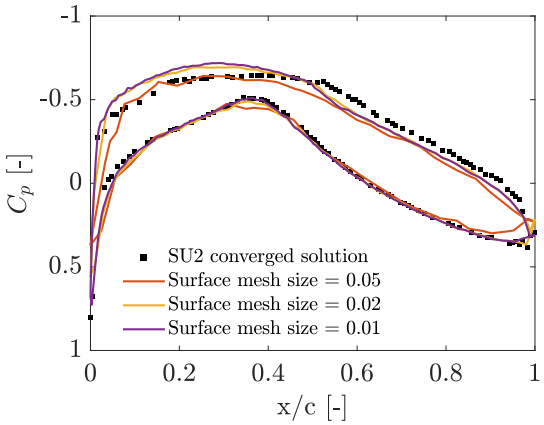

(a) Original DARTFLO implementation with a farfield mesh size = 0.5.

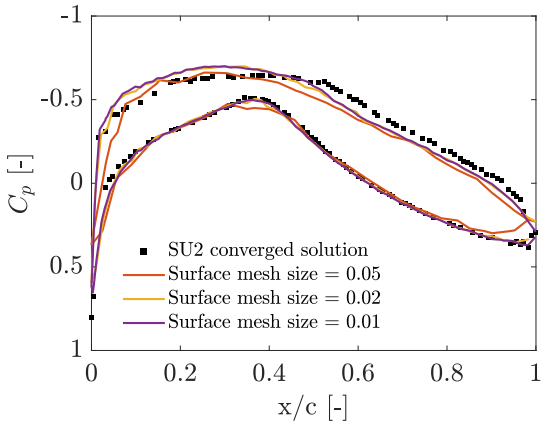

(b) Fixed length correction implementation with a farfield mesh size = 0.5 and $L = 0.1$.

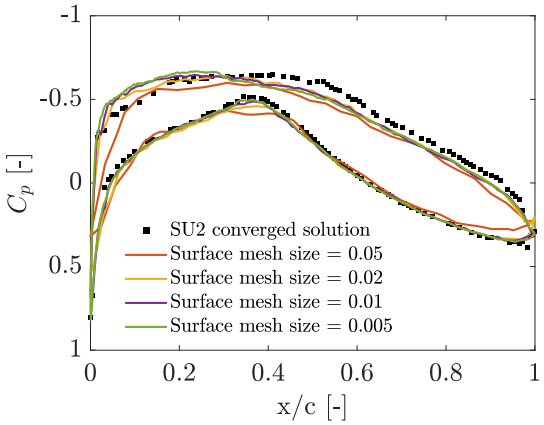

(c) Original DARTFLO implementation with a farfield mesh size = 1.

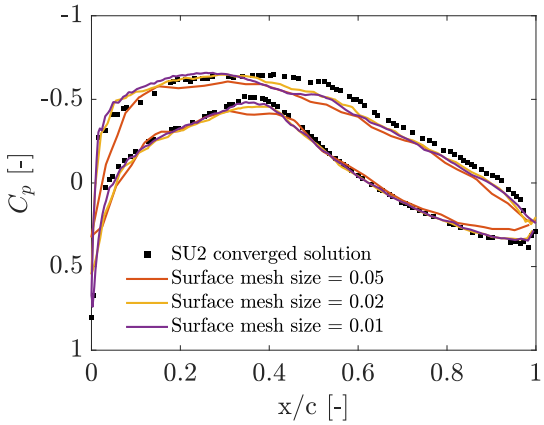

(d) Fixed length correction implementation with a farfield mesh size = 1 and $L = 0.1$.

FIGURE 4.41: Evolution of the pressure coefficient C_p distribution with respect to the mesh density for both original DARTFLO and fixed length correction implementations at the wingtip ($y = 14.25\ m$) in the three dimensional test case context.

4.4.5 Discussion

In this section, the results obtained for the different stabilisation processes in the three-dimensional test case are discussed.

The original DARTFLO implementation re-exhibits its mesh-dependency through different observations. Depending on the spanwise location, the local flow keeps varying with the mesh density. In addition, from a certain surface mesh size, short-wavelength oscillations are triggered by the stabilisation process mesh-dependency. However, DARTFLO illustrated quite accurate results with respect to the SU2 reference solution. As observed with the pressure distributions, the shock position computed with the original DARTFLO implementation closely meets the SU2 prediction with an averaged relative error of $\approx 1.5\%$. However, the aerodynamic coefficient analysis demonstrated that the farfield mesh size had still a small impact on the results. In other words, refining the farfield mesh size from 1 to 0.5 has an influence of 6% on the results.

The analysis of the fixed length correction has demonstrated that some improvements could be achieved regarding the mesh dependency limited by the choice of the fixed length in the three dimensional case. The surface element size largely varying along the span, it inevitably induces non-optimal fixed length everywhere over the three-dimensional wing. In addition, another limiting factor to the analysis has been the computational power available in the simulation computer for the three-dimensional test case. The mesh convergence and the fixed length selection processes require repetitive simulations. However, when the mesh is highly refined, large number of elements is treated resulting in simulations of several hours. With more CPU power, the improvements provided by the fixed length correction might have been more blatant. Therefore, further analyses should be conducted concerning the fixed length selection in three-dimensional case.

4.5 Discussion

Solutions based on the different stabilisation implementations were studied in the three different test cases. The weak shock test case has revealed that the sonic density bias solution and the switching function reformulation do not improve the mesh dependency of the results. However, great improvements have been obtained using the fixed length correction since mesh-dependency is almost withdrawn and mesh convergence is much enhanced. Therefore, the sonic density bias and the switching function reformulation solutions have been discarded from further analyses.

In the strong shock test case, the difficulty of finding an optimal fixed length was highlighted as being a limiting factor in the fixed length correction. The length range allowing the solver to converge is drastically narrowed. However, slight improvements can

be noticed in the supersonic regions where the oscillations due to the mesh-dependency are mostly removed.

To conclude, the three-dimensional test case supported the observation made in the previous test case concerning the fixed length selection. At each spanwise station, the fixed length correction shown the ability to slightly decrease mesh-dependency on one or several aspects. However, the original DARTFlo implementation illustrated to compute relevant results with respect to the reference solution even if mesh-dependency clues can be retrieved at each spanwise station.

5 Conclusion

5.1 Conclusions

Within the worldwide policies to reduce the aviation environmental impact and the ongoing quest to reduce aircraft fuel consumption, developing efficient modelling tools is one of the major keys. During the preliminary aircraft design, using fast and relatively accurate solvers enables to test different new aircraft configurations and thus, results in better design choices. At these early stages of the design, low-fidelity models are preferred demonstrating relevant results with low computational costs. Research has been performed to study the effects of levels of fidelity on steady aerodynamics and concluded that the *Full Potential* equation fulfilled the characteristics previously set out. Henceforth, the mathematical nature study of this partial differential equation brings into light that for transonic flows, the change in flow physics from subsonic to supersonic needs to be transcribed in the numerical implementation.

DARTFLO, a full-potential solver dedicated to the aerodynamic modelling of transonic flows in the preliminary aircraft design, is implemented using a density upwinding process introducing artificial viscosity when the local flow is supersonic. Thenceforth, this solution enables to derive a stable scheme for the subsonic flow portion and stabilise it when the flow becomes supersonic. The concept of the density upwinding consists in retarding the physical density with an upwind bias computed with a switching function and the upwind density.

The present thesis is the continuation of Crovato's work [27]. The density upwinding solution in DARTFLO experiences mesh-dependency. Therefore, the objective of this work was to characterise this mesh-dependency through different test cases and then, to develop new stabilisation alternatives.

The new stabilisation solutions were developed based on a literature review about full-potential methods and DARTFLO implementation. The first concept was to compute the upwind bias by evaluating the upwind streamwise density gradient multiplied by a

constant fixed length in the entire flow field to remove the mesh-dependency. Afterwards, the second correction was to replace the upwind bias by a constant at the flow scale. To reach the same effect as the density upwinding, the constant was determined to be the density at sonic conditions. The last solution has been a reformulation of the switching function based on observations provided by the literature.

The different stabilisation solutions were studied in different test cases. Two of them are two-dimensional cases with either a weak or a strong embedded shock. The third is a three-dimensional case based on a commercial regional aircraft wing. In each test cases, the original DARTFlo density upwinding was analysed and then, the corrections were compared to assess the improvements. The analysis of the original DARTFlo implementation confirmed its mesh-dependency addressed by Crovato [27]. In the whole three test cases, the first clue illustrating the results mesh-dependency is the oscillations appearing in the local flow parameters. When the mesh is highly refined, short-wavelength oscillations are created in supersonic zones. Indeed, since the upwind bias is dependent on the mesh size, the more the mesh is refined, the lower the stabilisation effect of the bias. Henceforth, the numerical scheme becomes more and more unstable giving rise to these oscillations. The second clue concerns the pressure distribution convergence. It has been observed that despite the mesh refinement, the pressure distribution across the shock keeps evolving showing still a large influence of the mesh on results. The last mesh-dependency observation is the convergence difficulty of the global parameters. From a certain mesh refinement, the solver stops converging resulting to not fully converged solutions. However, for precise mesh configurations, relevant results can still be calculated based on the original density upwinding compared to the higher level of fidelity, SU2.

First, the fixed length correction has shown improvements in different aspects of the mesh-dependency. The mesh convergence is facilitated since the mesh could be refined further. This can be achieved by almost fully attenuating the short-wavelength oscillations occurring in the supersonic zones when the mesh is extremely refined. In addition, the local flow could be converged with respect to the mesh refinement to reach mesh-independent solutions except in several cases for which the fixed length was not completely optimal and the results were not completely improved. The choice of the fixed length proved to be a limiting factor in the comparisons in the different test cases. It has been demonstrated that the optimal fixed length was decreasing with respect to surface mesh size until a certain threshold for which it converged. However, for the three-dimensional test case for example, the optimal fixed length for the wing root is not the same as for the wingtip since the reference chord lengths are different. Therefore, the selection choice should be investigated to develop a process to determine the optimal length anywhere in the case study whatever the dimensions.

The second alternative that has been proposed depicted that the artificial viscosity introduced through the constant sonic bias was too diffusive such that no shock could be captured by the solver. It has been illustrated by the local analysis showing nonexistent parameter drop that would correspond to a shock capturing.

The last new stabilisation solution was the switching function reformulation. It appeared that the new formulation experienced the same mesh-dependency as the original DARTFLO density upwinding. Similar clues could be observed in the weak shock test case analysis. This is explained by the re-expression of the switching function which is a reformulation of the original based on other flow parameters, simply transposing the problem under another formulation.

5.2 Suggestions for future work

Since the objectives have been partially fulfilled, the present thesis opens new questions about the density upwinding mesh-dependency. This section outlines suggestions for future work.

5.2.1 Fixed length selection process

As detailed in CHAP. 4, the fixed length selection process described in the present work has been a limiting factor for the full expression of the fixed length correction improvements. Further analysis should be performed to determine if a better selection process could be achieved enabling to choose the optimal fixed length depending on the case study or if the selection process is a restrictive factor not allowing long-term use of this solution.

5.2.2 Upwind density computation

In DARTFLO, the evaluation of the upwind density is performed on one unique element determined by minimising the scalar product between the local velocity vector and the vector joining both centroïds as explained in SEC. 2.4.2.

Another approach to withdraw the mesh-dependency could be to build up the upwind density based on a weighted average between all the adjacent upwind elements as depicted in FIG. 5.1. Adjacent elements qualified as upwind are determined based on negative scalar products between the local velocity vector and the vector joining both centroïds. The weights could be distributed based on the adjacent upwind element position with respect to the local velocity vector direction. Thenceforth, an upwind adjacent element located closest to the opposite local flow direction would have a heavier weight than the one positioned the furthest so that the upwind density ρ_U can be reconstructed.

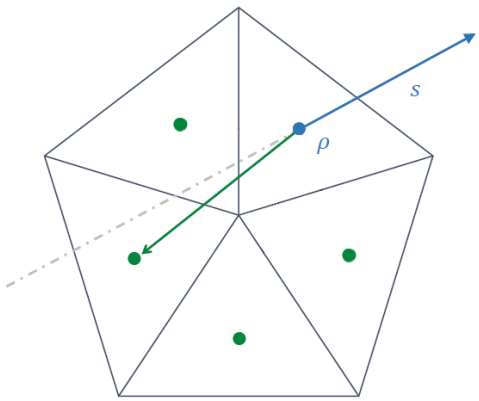

FIGURE 5.1: Multiple upwind elements approach.

TRANAIR is a full-potential, solution-adaptive, rectangular grid code for predicting subsonic, transonic, and supersonic flows about arbitrary configurations developed by Boeing company [62]. This code proposes a process to weight the influence of the upwind elements to compute the biased density depending on the mesh evolution between the adjacent cells and the current one. In TRANAIR context of a rectangular mesh grid, three scenarios can be stated. The first one is encountered when no mesh refinement is experienced such that each element face has an adjacent element. However, if the adjacent cells are refined or coarsened, all the contributions are averaged to upwind the density based on weights depending on the element location and size.

The upwinded density is determined based on the following relation,

$$\tilde{\rho} = \rho + \mu \sum_{i=1}^{6} \max\left(-\hat{V} \cdot \vec{n}_i, 0\right) S_i(\vec{V}) \sum_j C_{i,j} \left(\rho_{i,j} - \rho\right), \tag{5.2.1}$$

where, ρ is the physical density, μ the switching function, i runs over the 6 faces of the given rectangular box, j runs over the densities averaged to obtain the density upwinded to, $C_{i,j}$ is the weight coefficient depending on the box face and the upwind element contributing to the density upwinded to, $\hat{V}$ is the normalised velocity at the centroïd of the given element, $\vec{n}_i$ is the outward pointing normal to face i of the element, and $S_i(\vec{V})$ is a cubic blending function to make the upwinding differentiable.

This technique consisting in taking into account the location of the upwind element with respect to the opposite local flow direction to weight its associated density value could be adapted to DARTFLO and unstructured triangular mesh grids as depicted in FIG. 5.2. The influence of the element location to compute its corresponding weight could be taken into account by attributing more weight to upwind elements close to the opposite flow direction than the furthest. This weighted average is achieved by computing the cosine between the current local velocity vector and the centroïds vector such that elements whose

centroïd is almost aligned with the local flow direction would have cosine tending to 1 and inversely, tending to 0.

Thenceforward, the upwinded density formulation particularised for tetrahedral mesh element is expressed as,

$$\tilde{\rho} = \rho + \mu \sum_{i=1}^{4} \max\left(-\hat{V} \cdot \vec{n}_i, 0\right) S_i(\vec{V}) \frac{\sum_j \cos\theta_{i,j} \left(\rho_{i,j} - \rho\right)}{\sum_j \cos\theta_{i,j}}, \tag{5.2.2}$$

where, ρ is the physical density, μ the switching function described in Eq. 2.4.10, i runs over the 4 faces of the given tetrahedral element, j runs over the densities averaged to obtain the density upwinded to, $\cos\theta_{i,j}$ represents the cosine between the local flow vector and the vector linking both centroïds depending on the element face and the upwind element contributing to the density upwinded to, $\hat{V}$ is the normalised velocity at the centroïd of the given element, $\vec{n}_i$ is the outward pointing normal to face i of the element, and $S_i(\vec{V})$ is a cubic blending function to make the upwinding differentiable.

Note that the cosine for each upwind element is computed as follows,

$$\cos\theta_{i,j} = \frac{\mathbf{s} \cdot \mathbf{b}_{i,j}}{\|\mathbf{s}\| \|\mathbf{b}_{i,j}\|}, \tag{5.2.3}$$

where, $\mathbf{s}$ is the local velocity vector and $\mathbf{b_{i,j}}$ the vector joining the current element centroïd and the j upwind element one.

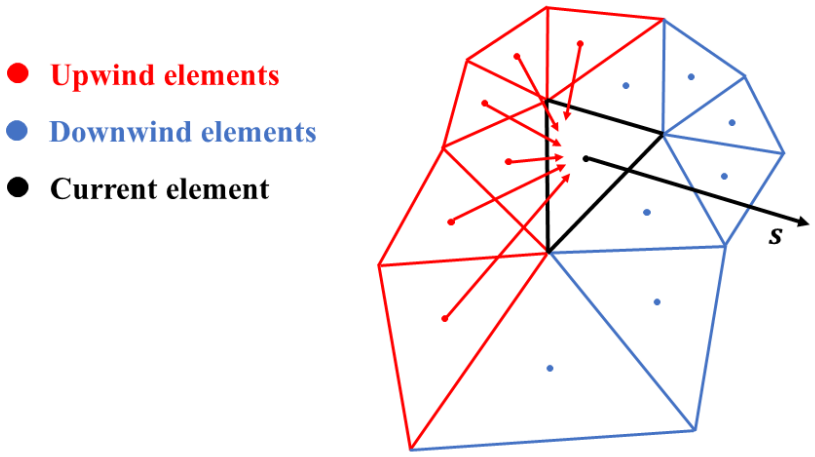

FIGURE 5.2: Two-dimensional multi upwind element influence inspired by TRANAIR upwind density computation routine.

5.2.3 Density gradient computation

In DARTFLO, the mesh-dependency mainly originates from the computation approximation of the streamwise upwind density gradient as initially derived by Hafez and Murman [46] in Eq. 2.3.13. Consequently, Tatum proposes a special algorithm for upwind differencing to avoid mesh-dependency by re-expressing the gradient differently [63]. The concept

is to determine the upwind element of a node based on the nodal velocity vector and to use the isentropic density defined at the corresponding element corners to build the artificial density upwinding effect as illustrated in FIG. 5.3.

Therefore, the upwind bias is computed as follows,

$$-\Delta s \overleftarrow{\delta}_s \rho = (\rho_i - \rho_j)\left[\frac{u}{q}\cos\beta_1 + \frac{v}{q}\sin\beta_1\right] + (\rho_i - \rho_k)\left[\frac{u}{q}\cos\beta_2 + \frac{v}{q}\sin\beta_2\right] \tag{5.2.4}$$

where, the points i, j and k and the angle β_1 and β_2 are defined in FIG. 5.3. In addition, (u, v) are the local velocity components whose magnitude is denoted by q.

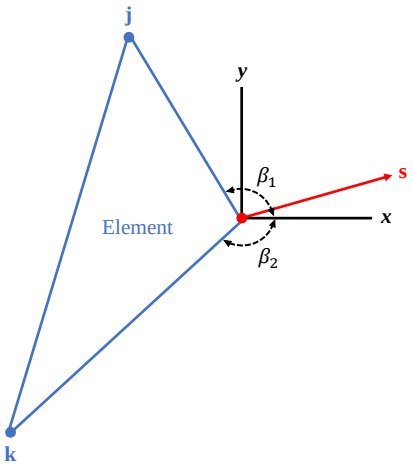

FIGURE 5.3: Relationship of angles β_1 and β_2 to upwind nodes on an arbitrary element depicted in [63].

5.2.4 Unsteady computations

Numerically, converging an unsteady system to steady states using time-marching procedure is better than solving directly a steady problem [64]. Even if the introduction of time-dependence usually has an influence on the mathematical nature of the corresponding partial differential equation, it has been demonstrated by Shankar *et al.* [65] that it does not enable to reach one single mathematical nature independent on the local flow regime in the case of the *Full Potential* equation.

Nevertheless, Kelley and Keyes explains that strategies such as line search combined with the quasi-Newton algorithm for steady partial differential equations stagnate to local minima. This behaviour is accentuated for solutions featuring complex flow characteristics such as shocks [66] altering the solver convergence. Using pseudo-time marching methods to compute time asymptotic steady-state solutions enables to ease the solver convergence and to increase solver robustness. The advantage of this procedure is the non-necessity to solve the non-linear equations until convergence, since all the intermediate steps in the transient phase are not of interest. According to Jiang and Forsyth [67], at each time step, only one nonlinear iteration is sufficient and occasionally, two or three if the flow varies

drastically during the corresponding time step. Therefore, using a pseudo-time marching procedure to derive a damped Newton method could be a good alternative to investigate in order to assess if it could improve DARTFLO convergence and robustness.

Bibliography

[1] U. Nations. *Department of Economic and Social Affairs*. 2019. https://www.un.org/development/desa/en/news/population/world-population-prospects-2019.html (visited on 04/26/2022) (cit. on p. 1).

[2] IHSMarkit. *IHS Economics*. 2022. https://ihsmarkit.com/index.html (visited on 04/26/2022) (cit. on p. 1).

[3] IATA. *20 Year Passenger Forecast*. 2022. https://www.iata.org/en/publications/store/20-year-passenger-forecast/ (visited on 04/26/2022) (cit. on p. 1).

[4] Boeing. *Commercial Market Outlook 20212040*. 2021. https://www.boeing.com/commercial/market/commercial-market-outlook/ (visited on 04/26/2022) (cit. on p. 1).

[5] D. S. Lee. "The contribution of global aviation to anthropogenic climate forcing for 2000 to 2018." In: *Atmospheric Environment* (2021) (cit. on p. 1).

[6] C. Aviation. "Strategic Research and Innovation Agenda." In: *Official report* (2021) (cit. on p. 1).

[7] E. Commission. "Flightpath 2050: Europe's vision for aviation." In: *Official report* (2012) (cit. on p. 1).

[8] Airbus. *ZEROe: Towards the worlds first zero-emission commercial aircraft*. 2022. https://www.airbus.com/en/innovation/zero-emission/hydrogen/zeroe (visited on 04/29/2022) (cit. on p. 2).

[9] Airbus. "Getting to grips with fuel economy." In: *Flight Operations Support Line Assistance report* (2004) (cit. on p. 2).

[10] A. J. Stolzer. "Fuel Consumption Modeling of a Transport Category Aircraft Using Flight Operations Quality Assurance Data: A Literature Review." In: *Journal of Air Transportation* (2002) (cit. on p. 2).

[11] Airbus. "Getting to grip with A320 family performance retention and fuel savings." In: *Flight Operations Support Line Assistance report* (2008) (cit. on p. 2).

[12] I. Bhateley and R. Cox. "Application of Computational Methods to Transonic Wing Design." In: *Progress in Astronautics and Aeronautics* (1981) (cit. on pp. 3, 6).

[13] A. Verhoff and P. ONeil. "Extension of FLO codes to transonic flow prediction for fighter configurations." In: *Progress in Astronautics and Aeronautics* (1981) (cit. on pp. 3, 6).

[14] P. Rubbert and G. Saaris. “Review and evaluation of a three-dimensional lifting potential flow analysis method for arbitrary configurations.” In: *10th AIAA Aerospace Science Meeting* (1972) (cit. on pp. 3, 6).

[15] J. Flores et al. “Comparison of the Full-Potential and Euler Formulations for Computing Transonic Airfoil Flows.” In: *Technical report, NASA* (1984) (cit. on pp. 3, 6).

[16] G. Klopfer and D. Nixon. “Nonisentropic potential formulation for transonic flows.” In: *AIAA Journal* (1984) (cit. on pp. 3, 6).

[17] J. Le Balleur. “Strong matching methods for computing transonic viscous flow including wakes and separations - lifting airfoils.” In: *La Recherche Aerospatiale* (1981) (cit. on pp. 3, 6).

[18] R. Melnik et al. “A Multigrid Method for the Computation of Viscid/Inviscid Interaction on Airfoils.” In: *Technical report, Grumman Aerospace Corporation* (1983) (cit. on pp. 3, 6).

[19] A. Van Muijden J.and Broekhuizen, A. van der Wees, and J. van der Vooren. “Flow analysis and drag prediction for transonic transport wing/body configurations using a viscousinviscid interaction type method.” In: *19th ICAS Congress* (1994) (cit. on pp. 3, 6).

[20] T. L. Holst. “Transonic flow computations using nonlinear potential methods”. In: *Progress in Aerospace Sciences* (2000), 36:1–61 (cit. on pp. 3, 6, 10).

[21] M. Drela, M. Giles, and W. Thompkins. “Newton Solution of Coupled Euler and Boundary Layer Equations.” In: *Numerical and Physical Aspects of Aerodynamic Flows* (1986) (cit. on pp. 3, 6).

[22] M. Potsdam. “An Unstructured Mesh Euler and Interactive Boundary Layer Method for Complex Configurations.” In: *12th Applied Aerodynamic Conference* (1994) (cit. on pp. 3, 6).

[23] M. Aftosmis, M. Berger, and J. Alonso. “Applications of a Cartesian Mesh Boundary-Layer Approach for Complex Configurations.” In: *44th AIAA Aerospace Science Meeting and Exhibit* (2006) (cit. on pp. 3, 6).

[24] A. Jameson. “The Evolution of Computational Methods in Aerodynamics.” In: *ournal of Applied Mechanics* (1983) (cit. on pp. 3, 6).

[25] F. Johnson, E. Tinoco, and N. Yu. “Thirty Years of development and applications of CFD at Boeing Commercial Airplanes.” In: *Computational Fluids* (2005) (cit. on pp. 3, 6).

[26] A. Crovato et al. “Effect of Levels of Fidelity on Steady Aerodynamic and Static Aeroelastic Computations.” In: *Aerospace* (2020) (cit. on pp. 3, 6).

[27] A. Crovato. “Steady Transonic Aerodynamic and Aeroelastic Modeling for Preliminary Aircraft Design”. PhD thesis. 2020 (cit. on pp. 4, 10, 13, 14, 16, 17, 21, 34, 70, 73, 74).

[28] P. Spalart and S. Allmaras. “A One-Equation Turbulence Model for Aerodynamic Flows.” In: *Recherche Aerospatiale* (1994), 1:5–21 (cit. on p. 5).

[29] J. Steger and B. Baldwin. “Shock waves and drag in the numerical calculation of isentropic transonic flows.” In: *Technical report, NASA* (1972) (cit. on p. 7).

[30] E. Murman and J. Cole. “Calculation of plane steady transonic flows.” In: *AIAA Journal* (1971) (cit. on pp. 10, 11, 13).

[31] J. Steger and H. Lomax. “Numerical calculation of transonic flow bout two-dimensional airfoils by relaxation procedures.” In: *AIAA Journal* (1972) (cit. on p. 11).

[32] P. Garabedian and D. Korn. “Analysis of transonic airfoils.” In: *Communications on Pure and Applied Mathematics* (1971) (cit. on p. 11).

[33] F. Bauer et al. “Supercritical Wing Section II.” In: *Lecture Notes in Economics and Mathematical Systems* (1975) (cit. on p. 11).

[34] J. J. South and A. Jameson. “Relaxation solutions for inviscid axisymmetric transonic flow over blunt or pointed bodies.” In: *First AIAA CFD Conference* (1973) (cit. on p. 11).

[35] J. Keller and J. J. South. “RAXBOD: A fortran program for inviscid transonic flow over axisymmetric bodies.” In: *NASA* (1976) (cit. on p. 11).

[36] J. Steger and H. Lomax. “Calculation of transonic flow around axisymmetric inlets.” In: *AIAA Journal* (1975) (cit. on p. 11).

[37] T. Baker. “A numerical method to compute inviscid transonic flow around axisymmetric ducted bodies.” In: *Symposium Transonicum II* (1975) (cit. on p. 11).

[38] D. Caughey and A. Jameson. “Accelerated iterative calculation of transonic nacelle flow fields.” In: *AIAA Journal* (1977) (cit. on p. 11).

[39] T. Reyhner. “Cartesian mesh solution for axisymmetric transonic potential flow around inlets.” In: *AIAA Journal* (1977) (cit. on p. 11).

[40] D. Ives and J. Liutermoza. “Analysis of transonic cascade flow using conformal mapping and relaxation techniques.” In: *AIAA Journal* (1977) (cit. on p. 11).

[41] D. Ives and J. Liutermoza. “Second-order-accurate calculation of transonic flow over turbomachinery cascades.” In: *AIAA Journal* (1979) (cit. on p. 11).

[42] A. Jameson. “Iterative solution of transonic flows over airfoils and wings, including flows at mach 1.” In: *Communications on Pure and Applied Mathematics* (1974) (cit. on pp. 11, 12).

[43] A. Jameson et al. “A brief description of the Jameson-Caughey NYU transonic swept-wing computer program FLO-22.” In: *NASA* (1976) (cit. on pp. 11, 12).

[44] A. Eberle. “A finite volume method for calculating transonic potential flow around wings from the pressure minimum integral.” In: *NASA* (1978) (cit. on pp. 12, 13).

[45] M. Hafez and W. J. Ballhaus. “Fast conservative schemes for the full potential equation applied to transonic flows.” In: *AIAA Journal* (1979) (cit. on pp. 12, 13, 24).

[46] M. Hafez, E. Murman, and J. J. South. “Artificial compressibility methods for numerical solution of transonic full potential equation.” In: *AIAA Journal* (1979) (cit. on pp. 12, 13, 16, 77).

[47] B. Engquist and S. Isher. “Stable and entropy satisfying approximations for transonic flow calculations.” In: *Mathematics of Computation* (1980) (cit. on p. 14).

[48] P. Goorjian and R. Van Buskirk. “Implicit calculations of transonic flows using monotone methods.” In: *AIAA paper* (1981) (cit. on p. 14).

[49] P. Goorjian, M. Meagher, and R. Van Buskirk. “Monotone implicit algorithms for the small-disturbance and full potential equations applied to transonic flows.” In: *AIAA paper* (1983) (cit. on p. 14).

[50] J. Boerstoel. "A multigrid algorithm for steady transonic potential flows around aerofoils using newton iteration." In: *Technical report, NASA* (1981) (cit. on p. 14).

[51] J. Slooff. "Some new developments in exact integral equation formulations for sub or transonic compressible potential flow." In: *Computational Mechanics Publications* (1982) (cit. on p. 14).

[52] S. Osher, M. Hafez, and W. J. Whitlow. "Entropy condition satisfying approximations for the full potential equations of transonic flow." In: *Mathematics of Computation* (1985) (cit. on p. 14).

[53] S. Osher, M. Hafez, and W. J. Whitlow. "Improved finite difference schemes for transonic potential fow calculations." In: *AIAA Journal* (1987) (cit. on p. 14).

[54] A. Kuethe and J. Schetzer. *Foundations of Aerodynamics*. John Wiley Sons, 1959 (cit. on p. 15).

[55] A. Em and J.-L. Guermond. "Theory and Practice of Finite Elements." In: Springer. 2004, pp. 88–93 (cit. on p. 17).

[56] C. Geuzaine and J.-F. Remacle. "Gmsh: a three-dimensional finite element mesh generator with built-in pre- and post-processing facilities." In: *International Journal for Numerical Methods in Engineering* (2009) (cit. on p. 26).

[57] T. D. Economoan et al. *SU2 v7.3.1 Blackbird*. https://su2code.github.io/. 2015 (cit. on pp. 28, 31, 58).

[58] A. Jameson. "Origins and Further Development of the Jameson-Schmidt-Turkel Scheme." In: *AIAA Journal* (2017) (cit. on p. 28).

[59] J. D. Anderson. *Fundamentals of aerodynamics (Sixth ed.)* McGraw Hill Education, 2017. ISBN: 978-1-259-12991-9. (Cit. on p. 29).

[60] P. Cook, M. McDonald, and M. Firmin. "Aerofoil Rae 2822: Pressure Distributions, and Boundary Layer and Wake Measurements." In: *Experimental Data Base for Computer Program Assessment, AGARD Report* (1979) (cit. on p. 29).

[61] V. Venkatakrishnan. "On the accuracy of limiters and convergence to steady state solutions." In: *31st Aerospace Sciences Meeting and Exhibit* (1993) (cit. on p. 32).

[62] F. T. Johnson et al. "TranAir: A Full-Potential, Solution-Adaptive, Rectangular Grid Code for Predicting Subsonic, Transonic, and Supersonic Flows About Arbitrary Configurations." In: *Theory document, NASA* (1992) (cit. on p. 76).

[63] K. E. Tatum. "Finite Element Methods for Transonic Flow Analysis." In: *AIAA Journal* (1983) (cit. on pp. 77, 78).

[64] C. Hirsch. *Numerical Computation of Internal and External Flows: The fundamentals of computational fluid dynamics*. Elsevier, 2007 (cit. on p. 78).

[65] V. Shankar, H. Ide, and J. Gorski. "A Fast, Time-Accurate, Unsteady Full Potential Scheme." In: *AIAA Journal* (1985) (cit. on p. 78).

[66] C. Kelley and D. E. KEYES. "Convergence Analysis Of Pseudo-Transient Continuation." In: *SIAM Journal on Numerical Analysis* (1998) (cit. on p. 78).

[67] H. Jiang and P. A. Forsyth. "Robust Linear And Nonlinear Strategies For Solution Of The Transonic Euler Equations." In: *Computers fluids* (1995) (cit. on p. 78).

Appendices

A One-dimensional shock code

The purpose of the one-dimensional full-potential finite element code was to illustrate the operation of the density upwinding process in a simple case. Afterwards, the observations would have been used to develop corrections to withdraw the mesh-dependency. However, the results obtained at the time do converge but the behaviour of the local flow at the shock is abnormal compared to what it expected.

A.1 Implementation

The implementation is mainly based on DARTFLO formulation. The *Full Potential* equation is particularised for one-dimensional problem such as,

$$\frac{\partial}{\partial x}\left(\rho\frac{\partial\phi}{\partial x}\right), \tag{1.1.1}$$

where, x denotes the direction of the problem and ϕ the total potential. The physical density ρ is computed based on the isentropic relations such that,

$$\rho = \rho_\infty\left[1+\frac{\gamma-1}{2}M_\infty^2\left(1-|\frac{\partial\phi}{\partial x}|^2\right)\right]^{\frac{1}{\gamma-1}}, \tag{1.1.2}$$

where, ρ_∞ is the freestream density, γ the heat capacity ratio and M_∞ freestream Mach number.

Adapting the finite element formulation based on EQ. 1.1.2 and 2.4.1, the one-dimensional full-potential finite element formulation can be cast as,

$$\int_\Omega \rho\frac{\partial\phi}{\partial x}\frac{\partial\psi}{\partial x}dV - \int_\Gamma \overline{\rho\frac{\partial\phi}{\partial x}}n_x\psi dS = 0, \quad \forall\psi\in H^1(\Omega), \tag{1.1.3}$$

where, Ω becomes the one-dimensional domain, Γ becomes nodes, *psi* defines the test functions and n_x is the normal of Γ.

In order to obtain a one-dimensional case with an embedded shock, Neumann boundary conditions are imposed at the inlet and the outlet. At the inlet domain, a supersonic Mach

number is imposed in order to build up a supersonic area before the shock is created such that,

$$\overline{\frac{\partial \phi}{\partial x}} n_x \Big|_{\text{Node inlet}} = U_{\text{inlet}} n_x. \tag{1.1.4}$$

Concerning the outlet, the same process is implemented by imposing a subsonic velocity,

$$\overline{\frac{\partial \phi}{\partial x}} n_x \Big|_{\text{Node outlet}} = U_{\text{outlet}} n_x. \tag{1.1.5}$$

B Test cases shock strength validation

B.1 Weak shock test case validation

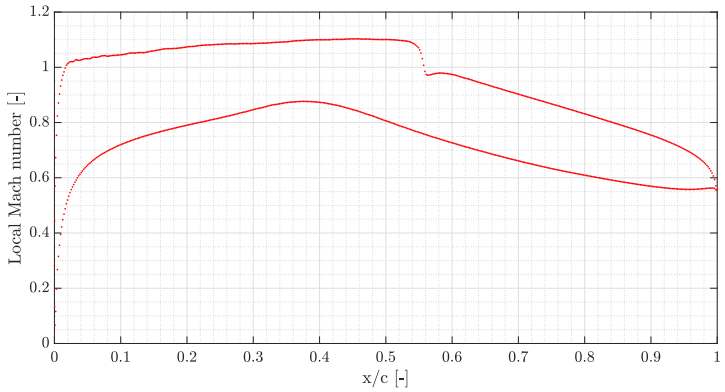

FIGURE B.1: Local Mach number along the airfoil for the weak shock configuration described in TAB. 4.1 for mesh sizes of 1/2 of the chord at the farfield and 1/500 at the airfoil.

B.2 Strong shock test case validation

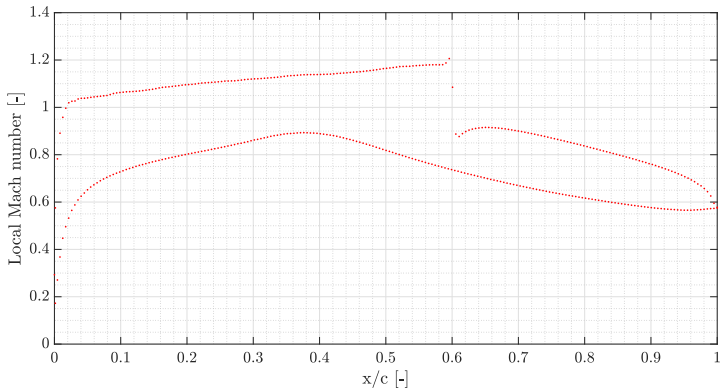

FIGURE B.2: Local Mach number along the airfoil for the strong shock configuration described in TAB. 4.3 for mesh sizes of 1/2 of the chord at the farfield and 1/200 at the airfoil.

B.3 Three-dimensional test case validation

Mesh size	**Value**
Farfield mesh size $[m]$	1
Wing root surface mesh size $[m]$	$\frac{c_R}{200}$
Wingtip surface mesh size $[m]$	$\frac{c_T}{200}$
Mesh density [elements]	2925091

TABLE B.1: Mesh sizes for three-dimensional case validation

where, c_R corresponds to the wing root chord length and c_T to the wingtip chord length. Based on this mesh and flow characteristics summarised in TAB. 4.6, the wing aerodynamic coefficients are computed,

Aerodynamic coefficient	**Value**
C_L $[-]$	.446
C_D $[-]$	.009

TABLE B.2: Aerodynamic performances of the three-dimensional wing design.

C Additional reference solution computations

C.1 Three-dimensional reference solution

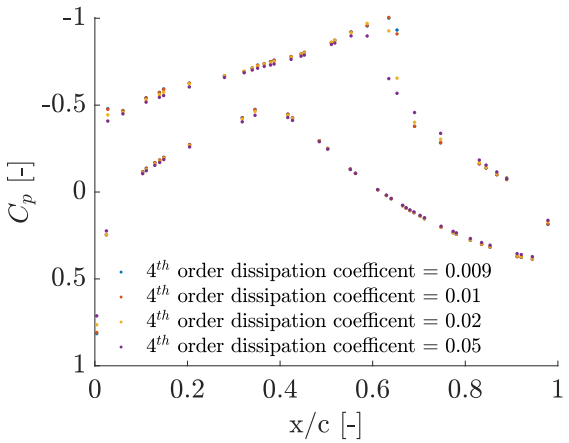

FIGURE C.1: Influence study of the 4^{th} order dissipation coefficient in Jameson-Schmidt-Turkel scheme using SU2 based on the converged mesh with the by-default 2^{nd} order dissipation coefficient for the three-dimensional test case on the pressure distribution at the mean aerodynamic chord ($y = 3.63\ m$).

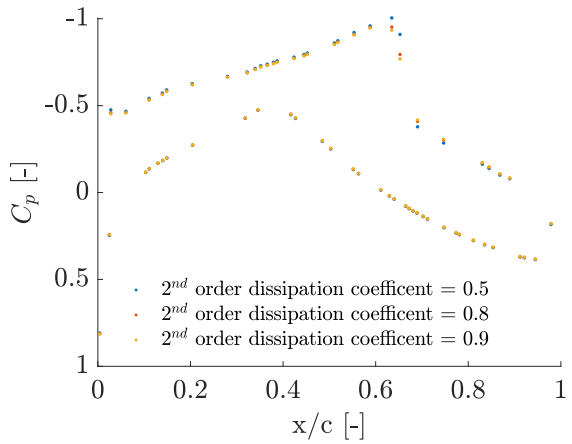

FIGURE C.2: Influence study of the 2^{nd} order dissipation coefficient in Jameson-Schmidt-Turkel scheme using SU2 based on the converged mesh with the optimal 4^{th} order dissipation coefficient for the three-dimensional test case on the pressure distribution at the mean aerodynamic chord ($y = 3.63\ m$).